

**EXPLORING THE THERMAL EXPANSION OF FLUORIDES AND
OXYFLUORIDES WITH ReO_3 -TYPE STRUCTURES: FROM
NEGATIVE TO POSITIVE THERMAL EXPANSION**

A Thesis
Presented to
The Academic Faculty

by

Benjamin K. Greve

In Partial Fulfillment
of the Requirements for the Degree
Doctor of Philosophy in the
School of Chemistry and Biochemistry

Georgia Institute of Technology
May 2012

EXPLORING THE THERMAL EXPANSION OF FLUORIDES AND
OXYFLUORIDES WITH ReO_3 -TYPE STRUCTURES: FROM
NEGATIVE TO POSITIVE THERMAL EXPANSION

Approved by:

Professor Angus P. Wilkinson, Advisor
School of Chemistry and Biochemistry
Georgia Institute of Technology

Professor Z. John Zhang
School of Chemistry and Biochemistry
Georgia Institute of Technology

Dr. Peter J. Chupas
X-Ray Science Division, APS
Argonne National Laboratory

Professor Christopher W. Jones
School of Chemical & Biomolecular
Engineering
Georgia Institute of Technology

Professor Jake Soper
School of Chemistry and Biochemistry
Georgia Institute of Technology

Date Approved: December 19, 2011

To those who are no longer with us, but should have seen this to the end...

My grandmother, Viola M. Ward

and

My best friend, Derek B. Benicewicz

ACKNOWLEDGEMENTS

Writing the acknowledgments for this thesis is perhaps more difficult than writing the thesis itself; there have been many people who have been instrumental in this work and in my life. My time at Georgia Tech has flown by, and has certainly been filled with its up and downs. I am very grateful for all of the friends I've made during my time here, and for all of the experiences I've had along the way.

First and foremost, I'd like to thank my adviser Professor Angus Wilkinson. Without his support throughout my time here, this thesis would not have been possible. In addition to advising me in the traditional research issues that all advisers face, he was always available when personal issues arose that impacted my work (unfortunately he had to deal with more than any adviser should). I appreciate all of his support and cooperation during my time here. I would also like to thank all of my committee members, especially for their flexibility and understanding with scheduling requirements.

My family also deserves special recognition for their support during my time at Georgia Tech. There were many times where I considered just getting a Master's degree in Chemistry and finding a job, but they were always around to allow me to vent and helped prevent me from making a rash decision. My brother, Alan Greve, found himself answering his phone many times in the middle of the night and during the early hours of the morning when I just needed someone to talk to. While not a brother by birth, I need to also thank Lloyd Morris for all the reality checks he gave me while I was in grad school; while hearing them was not always easy, they were necessary. Without all of their support, this would not have been possible.

During my time here at Georgia Tech I have made several good friends who have always been there for me. I'll never forget the time I spent studying for classes with Andrew Brown and Michael Bayless, or the time spent bouncing research ideas off of each other. Nor will I forget all of the help Matthew Hagy provided when I had endless questions concerning

writing pieces of code for data analysis. I was fortunate in that I was also able to spend a lot of time with these guys outside of Georgia Tech as well.

I also developed close friendships with Rebecca Key and Deborah Ortiz while at Georgia Tech. I thank both of these outstanding ladies for their friendship during my time here. Rebecca and I have spent countless hours talking about everything from science to the stress of graduate school; she was always available when I needed her, and I can honestly say that without her finishing this thesis would have been a lot more stressful. Near the end of my time here, Deborah provided me a room to stay in and was always available to listen to me unwind after a long day in the lab. Both of these ladies now know more about materials chemistry than they probably ever cared to!

A special thanks also needs to be given to Dr. Andrew Jupe and Cody Morelock of the Wilkinson Group. Andrew spent countless hours helping me with various scripts used in data analysis, and was always asking me challenging questions. I spent countless hours conducting experiments at National Labs with both Cody and Andrew, and Cody's proofreading of this thesis was invaluable. I appreciate all of your help, guys.

Most of the research presented in this thesis has depended heavily on experiments conducted at the Advanced Photon Source (APS) at Argonne National Lab and at the High Flux Isotope Reactor (HFIR) at Oak Ridge National Lab. During the course of these experiments, I was privileged to be able to work with a great group of scientists who have been instrumental in my growth as a scientist. I've spent a considerable amount of time working with Dr. Karena Chapman and Dr. Pete Chupas while conducting experiments at the APS. They have both provided an immense amount of guidance on all of my research projects, and have always been available when I had questions that others couldn't answer.

Dr. Chapman was instrumental in all of the high pressure studies using diamond anvil cells (DACs); most of the measurements were made using her DACs and she spent a considerable amount of time teaching me how to use them. She also spent a good amount of time teaching me how to extract pair distribution functions from total scattering data, while making sure that I fully understood what was going on in the process. I appreciate all of the time that was devoted by the APS crew to teaching me how to conduct the diffraction

experiments on my own.

During my time conducting experiments at HFIR I was able to have many conversations with Dr. Clarina Dela Cruz. We discussed everything from the project at hand to future career choices. I really enjoyed these conversations, and feel that they have helped me develop a clear picture of where I want to be professionally.

Finally, I'd like to thank my best friend Derek Benicewicz. Unfortunately, Derek is no longer with us, but I am thankful for every moment I got to spend with Derek during my time at Tech. When I had a personal crisis, Derek was the first person who was there for me to make sure that everything was okay. Without him, I certainly would not be where I am now. I miss you, Derek.

This work was partially supported by the National Science Foundation under grants DMR-0605671 and DMR-0905842. Use of the Advanced Photon Source at Argonne National Laboratory was supported by the U. S. Department of Energy, Office of Science, Office of Basic Energy Sciences, under Contract No. DE-AC02-06CH11357. Part of this work was performed at Oak Ridge National Laboratory's High Flux Isotope Reactor, sponsored by the Scientific User Facilities Division, Office of Basic Energy Sciences, U. S. Department of Energy.

TABLE OF CONTENTS

DEDICATION	iii
ACKNOWLEDGEMENTS	iv
LIST OF TABLES	x
LIST OF FIGURES	xii
SUMMARY	xv
I INTRODUCTION	1
1.1 Thermal Expansion	1
1.2 Low Thermal Expansion Materials	3
1.3 Negative Thermal Expansion	4
1.3.1 Mechanisms for Negative Thermal Expansion	4
1.3.2 ReO ₃ Family	6
1.3.3 NTE Materials Under Pressure	8
II PRONOUNCED NEGATIVE THERMAL EXPANSION IN ScF₃ . .	12
2.1 Introduction	12
2.2 Experimental	12
2.2.1 Variable Temperature Diffraction Studies	14
2.2.2 High Pressure Diffraction Studies	14
2.3 Results	15
2.3.1 Temperature Dependence of Unit Cell Dimensions	17
2.3.2 High Pressure Behavior	17
2.4 Discussion	20
2.5 Conclusions	22
2.6 Supplemental Information	22
III SYNTHESIS AND CHARACTERIZATION OF TITANIUM OXYFLUORIDE AND TITANIUM OXYHYDROXYFLUORIDES	24
3.1 Introduction	24
3.2 Experimental	26
3.2.1 Syntheses	26

3.2.2	Sample Characterization	26
3.2.3	Non-Ambient Diffraction Studies	27
3.3	Results	28
3.3.1	Phase Purity and Room Temperature Crystal Structure	28
3.3.2	Thermogravimetric and IR Spectral Analysis	29
3.3.3	Variable Temperature PXRD	29
3.3.4	Variable Pressure PXRD	35
3.4	Discussion	42
3.5	Conclusions	46
3.6	Supplementary Information	46
IV	EFFECT OF PRESSURE ON THE PROPERTIES OF TaO₂F AND ScF₃	50
4.1	Introduction	50
4.2	Experimental	51
4.2.1	Sample Preparation	51
4.2.2	High Pressure–Low Temperature Neutron Diffraction	52
4.2.3	High Pressure–High Temperature X-ray Diffraction	53
4.3	Results	53
4.3.1	TaO ₂ F	53
4.3.2	ScF ₃	60
4.4	Discussion	60
4.5	Conclusions	66
4.6	Supplemental Information	66
V	LOCAL STRUCTURE OF TaO₂F AND TiOF₂	72
5.1	Introduction	72
5.2	Experimental	74
5.2.1	Sample Preparation	74
5.2.2	Total Scattering Data Collection	75
5.2.3	Diffraction Data Processing	75
5.3	Results	75
5.3.1	Titanium Oxyfluoride	75

5.3.2	TaO ₂ F	77
5.4	Discussion	86
5.5	Conclusions	88
5.6	Supplemental Information	88
VI	CONCLUDING REMARKS	94
	REFERENCES	96

LIST OF TABLES

1	Coefficients of thermal expansion for some common materials	3
2	List of negative thermal expansion framework materials and their amorphization pressures	11
3	Equation of State parameters for ScF_3 under pressure	20
4	ScF_3 unit cell parameters as a function of pressure	23
5	Crystallographic data for TiOF_2 prepared from the direct reaction of TiO_2 with TiF_4	30
6	Crystallographic data for $\text{Ti}_{1-x}(\text{O}/\text{OH}/\text{F})_3$	31
7	Selected coefficients of thermal expansion for TiOF_2 and $\text{Ti}_{1-x}(\text{O}/\text{OH}/\text{F})_3$	33
8	Equation of State parameters for TiOF_2 & $\text{Ti}_{1-x}(\text{O}/\text{OH}/\text{F})_3$	40
9	Rietveld refinement results from TiOF_2 at 298 K from the variable temperature cryostream experiments	47
10	Rietveld refinement results for $\text{Ti}_{1-x}(\text{O}/\text{OH}/\text{F})_3$ at 298 K from the variable temperature cryostream experiments	48
11	TiOF_2 unit cell parameters as a function of pressure	49
12	$\text{Ti}_{1-x}(\text{O}/\text{OH}/\text{F})_3$ unit cell parameters as a function of pressure	49
13	Average coefficients of thermal expansion and bulk moduli for $\text{TaO}_2\text{F-A}$ and $\text{TaO}_2\text{F-B}$ from the low temperature–high pressure diffraction experiments at HFIR	59
14	Average coefficients of thermal expansion and bulk moduli for $\text{TaO}_2\text{F-B}$ from the high temperature–high pressure diffraction experiments at beamline 11-ID-B, APS	59
15	Average coefficients of thermal expansion and bulk moduli for ScF_3 from the low temperature–high pressure diffraction experiments at HFIR	63
16	$\text{TaO}_2\text{F-A}$ lattice constants from the low temperature–high pressure neutron diffraction experiments at HFIR	67
17	$\text{TaO}_2\text{F-B}$ lattice constants from the low temperature–high pressure diffraction experiments at HFIR	68
18	$\text{TaO}_2\text{F-B}$ lattice constants from the high temperature–high pressure diffraction experiments at APS	69
19	ScF_3 lattice constants from the variable pressure–temperature experiments	70
20	Tetragonal model with oxygen atoms in the $a - b$ plane used to describe the local structure of cubic TiOF_2	76

21	Tetragonal model with oxygen atoms out of the $a - b$ plane used to describe the local structure of cubic TiOF_2	78
22	Ti- X -Ti ($X = \text{O}, \text{F}$) bond lengths and angles from tetragonal models fit to the pair distribution function at short range for cubic TiOF_2	78
23	Ta- X -Ta ($X = \text{O}, \text{F}$) bond lengths and angles from fit of supercell model to local structure of TaO_2F	81
24	Average linear coefficients of thermal expansion for the Ta- X -Ta links in TaO_2F	86
25	Extracted TaO_2F lattice constants from fits to the variable temperature PDFs	91
26	Supercell model used to describe the local structure of TaO_2F	92
27	Final atomic positions in the tetragonal model used to describe the local structure of cubic TiOF_2 . Initial refinement placed the oxygen atoms out of the $a - b$ plane, and once a minimum in R_W was reached, they oxygen atoms were placed back into the $a - b$ plane for further refinement.	93

LIST OF FIGURES

1	Interatomic potential well	2
2	Cell edges and unit cell volume for PbTiO_3	5
3	Illustration of how negative thermal expansion can arise from rigid unit modes	6
4	Cubic ReO_3 structure type	7
5	Schematic of a diamond anvil cell	9
6	Illustration of how negative thermal expansion can arise in the ReO_3 structure type	13
7	An illustration depicting the rhombohedral to cubic phase transition in ReO_3 type structures	13
8	Representative Rietveld fit to ScF_3 variable temperature cryostream data .	16
9	Representative Rietveld fit to ScF_3 variable temperature wire wound furnace data	16
10	Representative Rietveld fit to ScF_3 high temperature Linkam furnace data .	18
11	Representative Rietveld fit to ScF_3 variable temperature neutron powder diffraction data	18
12	ScF_3 lattice constant versus temperature and derived coefficient of thermal expansion	19
13	ScF_3 pressure-temperature phase diagram	19
14	Equation of State fit to the experimental unit cell volumes of ScF_3 under pressure	21
15	Atomic displacement parameters for ScF_3 as a function of temperature . . .	21
16	Rietveld fit for TiOF_2 synthesized from the direct reaction of TiO_2 with TiF_4	30
17	Rietveld fit for $\text{Ti}_{1-x}(\text{O}/\text{OH}/\text{F})_3$	31
18	Thermogravimetric analysis of TiOF_2 and $\text{Ti}_{1-x}(\text{O}/\text{OH}/\text{F})_3$	32
19	IR spectra for $\text{Ti}_{1-x}(\text{O}/\text{OH}/\text{F})_3$ and TiOF_2	32
20	Unit cell volume versus temperature for $\text{Ti}_{1-x}(\text{O}/\text{OH}/\text{F})_3$	34
21	Unit cell volume versus temperature for TiOF_2	34
22	Stack plot of high temperature $\text{Ti}_{1-x}(\text{O}/\text{OH}/\text{F})_3$ powder X-ray diffraction data	36
23	Stack plot of high temperature TiOF_2 powder X-ray diffraction data	36
24	Determination of TiOF_2 phase transition temperature from Bragg peak widths	37

25	Determination of TiOF_2 phase transition temperature from Bragg peak areas	37
26	Atomic displacement parameters for TiOF_2 as a function of temperature . .	38
27	Stack plot of variable pressure diffraction data for $\text{Ti}_{1-x}(\text{O}/\text{OH}/\text{F})_3$	39
28	Stack plot of variable pressure diffraction data for TiOF_2	39
29	TiOF_2 rhombohedral cell angle versus pressure	40
30	Ti-X-Ti bond angle versus pressure	40
31	Equation of State fit to unit cell volume data for TiOF_2	41
32	Rietveld fit for TiOF_2 at 298 K from the variable temperature cryostream experiments	47
33	Rietveld fit for $\text{Ti}_{1-x}(\text{O}/\text{OH}/\text{F})_3$ at 298 K from the variable temperature cryostream experiments	48
34	Rietveld fit to 280 K–0.01 GPa TaO_2F Diffraction Pattern from HFIR . . .	55
35	Representative Rietveld fit to TaO_2F High Pressure–High Temperature PXRD Data	55
36	TaO_2F -A unit cell volume versus temperature at pressure from low temperature–high pressure measurements at HFIR	56
37	TaO_2F -A unit cell volume versus pressure at temperature from low temperature–high pressure diffraction experiments at HFIR	56
38	TaO_2F -B unit cell volume versus temperature at pressure from low temperature–high pressure diffraction experiments at HFIR	57
39	TaO_2F -B unit cell volume versus pressure at temperature from low temperature–high pressure diffraction experiments at HFIR	57
40	High pressure–high temperature TaO_2F unit cell volume versus temperature at pressure	58
41	High pressure–high temperature TaO_2F unit cell volume versus pressure at temperature	58
42	$R\bar{3}c$ structural model fit to a 60 K – 0.3 GPa diffraction pattern for TaO_2F collected at IPNS	61
43	$Pm\bar{3}m$ structural model fit to the ambient diffraction data for TaO_2F collected at IPNS	61
44	$Pm\bar{3}m$ structural model fit to a 60 K–0.3 GPa diffraction pattern for TaO_2F collected at IPNS	62
45	ScF_3 unit cell volume versus temperature at pressure from data collected at HFIR	62
46	ScF_3 unit cell volume versus pressure at temperature from data collected at HFIR	70

47	TaO ₂ F and ScF ₃ bulk moduli plotted with respect to temperature	71
48	Rietveld fit to a 280 K–ambient pressure ScF ₃ Diffraction pattern from HFIR	71
49	Fit of the cubic $Pm\bar{3}m$ model to the 500 K X-ray PDF for TiOF ₂	79
50	Fit of a tetragonal model with oxygen atoms in the equatorial $a - b$ plane to a pair distribution function for cubic TiOF ₂	79
51	Fit of a tetragonal model with oxygen atoms out of the $a - b$ plane to a pair distribution function for cubic TiOF ₂	80
52	Fit of a tetragonal model with oxygen atoms placed back into $a - b$ plane after a minimum in R_W was observed following refinement of a tetragonal model with oxygen out of $a - b$ plane to a pair distribution function for cubic TiOF ₂	80
53	Fit of a cubic $Pm\bar{3}m$ model to the 80 K X-ray pair distribution function for TaO ₂ F	82
54	Fit of a 3x3x3 supercell to a pair distribution function for TaO ₂ F	82
55	Atom positions from the TaO ₂ F supercell on the (0 0 1) plane	83
56	Ta–O–Ta separation as a function of temperature, $Q_{max}=25.9$	83
57	Ta–O–Ta separation as a function of temperature, $Q_{max}=25$	84
58	Ta–O–Ta separation as a function of temperature, $Q_{max}=25.9$ and the PDF was smoothed	84
59	Ta–F–Ta separation as a function of temperature, $Q_{max}=25.9$ and the PDF was smoothed	85
60	Ta–F–Ta separation as a function of temperature, $Q_{max}=25.9$	85
61	Ta–F–Ta separation as a function of temperature, $Q_{max}=25$	89
62	Crystal structure of the tetragonal model with the oxygen atoms in the $a - b$ plane, used to fit the pair distribution function for cubic TiOF ₂	89
63	Crystal structure of the tetragonal model with oxygen atoms out of the $a - b$ plane, used to fit the pair distribution function for cubic TiOF ₂	90
64	Representative fit of the cubic $Pm\bar{3}m$ model to the variable temperature PDFs for TaO ₂ F	90
65	TaO ₂ F lattice constant versus temperature extracted from fits to the variable temperature PDFs	93

SUMMARY

This thesis explores the thermal expansion and high pressure behavior of some materials with the ReO_3 structure type. This structure is simple and has, in principle, all of the features necessary for negative thermal expansion (NTE) arising from the transverse thermal motion of the bridging anions and the coupled rotation of rigid units; however, ReO_3 itself only exhibits mild NTE across a narrow temperature range at low temperatures. ReO_3 is metallic because of a delocalized d -electron, and this may contribute to the lack of NTE in this material. The materials examined in this thesis are all based on d^0 metal ions so that the observed thermal expansion behavior should arise from vibrational, rather than electronic, effects.

In Chapter 2, the thermal expansion of scandium fluoride, ScF_3 , is examined using a combination of *in situ* synchrotron X-ray and neutron variable temperature diffraction. ScF_3 retains the cubic ReO_3 structure across the entire temperature range examined (10 – 1600 K) and exhibits pronounced negative thermal expansion at low temperatures. The magnitude of NTE in this material is comparable to that of cubic ZrW_2O_8 , which is perhaps the most widely studied NTE material, at room temperature and below. This is the first report of NTE in an ReO_3 type structure across a wide temperature range.

Chapter 3 presents a comparison between titanium oxyfluoride, TiOF_2 , and a vacancy-containing titanium hydroxyoxyfluoride, $\text{Ti}_x(\text{O}/\text{OH}/\text{F})_3$. TiOF_2 was originally reported to adopt the cubic ReO_3 structure type under ambient conditions, therefore the initial goal for this study was to examine the thermal expansion of this material and determine if it displayed interesting behavior such as NTE. During the course of the study, it was discovered that the original synthetic method resulted in $\text{Ti}_x(\text{O}/\text{OH}/\text{F})_3$, which does adopt the cubic ReO_3 structure type. The chemical composition of the hydroxyoxyfluoride is highly dependent upon synthesis conditions and subsequent heat treatments. This material readily pyrohydrolyzes at low temperatures (≈ 350 K). It was also observed that TiOF_2

does not adopt the cubic ReO_3 structure; at room temperature it adopts a rhombohedrally distorted variant of the ReO_3 structure. Positive thermal expansion was observed for TiOF_2 from 120 K through decomposition into TiO_2 . At ≈ 400 K, TiOF_2 undergoes a structural phase transition from rhombohedral to cubic symmetry. High pressure diffraction studies revealed a cubic to rhombohedral phase transition for $\text{Ti}_x(\text{O}/\text{OH}/\text{F})_3$ between 0.5–1 GPa. No phase transitions were observed for TiOF_2 on compression.

In Chapter 4, an *in situ* variable pressure–temperature diffraction experiment examining the effects of pressure on the coefficients of thermal expansion (CTE) for ScF_3 and TaO_2F is presented. In the manufacture and use of composites, which is a possible application for low and NTE materials, stresses may be experienced. Pressure was observed to have a negligible effect on cubic ScF_3 ’s CTE; however, for TaO_2F the application of modest pressures, such as those that might be experienced in the manufacture or use of composites, has a major effect on its CTE. This effect is associated with a pressure-induced phase transition from cubic to rhombohedral symmetry upon compression. TaO_2F was prepared from the direct reaction of Ta_2O_5 with TaF_5 and from the digestion of Ta_2O_5 in hot hydrofluoric acid. The effects of pressure on the two samples of TaO_2F were qualitatively similar. The slightly different properties for the samples are likely due to differences in their thermal history leading to differing arrangements of oxide and fluoride in these disordered materials.

In Chapter 5, the local structures of TiOF_2 and TaO_2F are examined using pair distribution functions (PDFs) obtained from X-ray total scattering experiments. In these materials, the anions (O/F) are disordered over the available anion positions. While traditional X-ray diffraction provides detailed information about the average structures of these materials, it is not sufficient to fully understand their thermal expansion. Fits of simple structural models to the low r portions of PDFs for these materials indicate the presence of geometrically distinct $M\text{--}X\text{--}M$ ($M = \text{Ti}, \text{Ta}$; $X = \text{O}, \text{F}$) linkages, and a simple analysis of the TaO_2F variable temperature PDFs indicates that these distinct links respond differently to temperature.

CHAPTER I

INTRODUCTION

1.1 Thermal Expansion

Thermal expansion is an inherent property of all materials, and a thorough understanding of how a material responds to temperature is crucial when considering its potential application.[1] Combining materials with differing rates of thermal expansion may be detrimental to some applications; cracks may form or separation may occur at interfaces between the materials.[2] Likewise, materials which exhibit large thermal expansion often exhibit poor thermal shock resistance and may crack or fail during periods of rapid heating and cooling.[3, 4]

Most materials exhibit positive thermal expansion, that is, they expand upon heating.[1, 4] This process is generally well understood, and for the simplest case, that of a diatomic molecule, thermal expansion can be explained through examination of the interatomic potential.[1, 5] The interatomic potential explains how a chemical bond length changes with temperature; as energy (or temperature) increases, vibrations increase and the chemical bond lengthens.[1, 5] If the potential were purely harmonic, then the average interatomic distance would be the same for all temperatures and thermal expansion would not be observed.[1, 5] However, the interatomic potential is typically anharmonic, and, as seen in Figure 1, the average chemical bond length increases with increasing temperature.[1, 5]

Thermal expansion in solids is a more complicated situation than that of a simple diatomic molecule as the thermal expansion of all chemical bonds and the changes in bond angles with temperature must be taken into consideration.[6] The magnitude of thermal expansion in a material is quantified by its coefficient of thermal expansion (CTE); the volumetric CTE, α_v , is defined as:[6]

$$\alpha_v = \frac{d(\ln V)}{dT} = \frac{1}{V} \frac{dV}{dT} \quad (1)$$

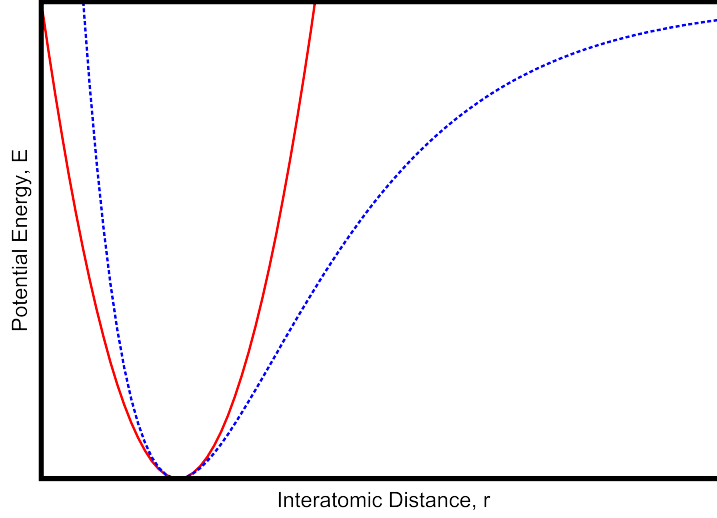


Figure 1: Potential energy (E) curves for harmonic (solid) and anharmonic (dashed) oscillators plotted as a function of interatomic separation, r .

where V is the unit cell volume and T is the temperature. The linear CTEs, α_l , are defined as:

$$\alpha_l = \frac{d(\ln L)}{dT} = \frac{1}{L} \frac{dL}{dT} \quad (2)$$

where L is the value of each unique lattice constant and T is the temperature. The volumetric CTE describes the overall expansion in a material; in the case of cubic materials in which all lattice constants are equivalent, $\alpha_v = 3\alpha_l$. In the case of anisotropic materials, different values of α_l are typically observed for different lattice constants.[6]

The CTE of a material is not a constant value; there is a temperature dependence to the CTE as there is with the specific heat. This temperature dependence is illustrated in the Grueneisen relationship:

$$\alpha_v = \frac{\gamma K_0 C_v}{v} \quad (3)$$

where α_v is the volumetric CTE, γ is the Grueneisen constant, K_0 is the compressibility, C_v is the specific heat at constant volume, and v is the molar volume.[6, 3, 4] At absolute zero, the CTE will be zero but increases rapidly to the region of the Debye temperature at which point it will asymptotically approach a constant value at high temperature.[7]

Ceramic materials may be divided into three different categories depending upon the magnitude of the volumetric CTE:[7]

High Expansion Materials:	$\alpha_l > 8 \times 10^{-6} K^{-1}$
Intermediate Expansion Materials:	$2 < \alpha_l < 8 \times 10^{-6} K^{-1}$
Low Expansion Group:	$0 \leq \alpha_l < 2 \times 10^{-6} K^{-1}$

1.2 Low Thermal Expansion Materials

Materials that fall into the low expansion group are interesting from an applications perspective as low expansion materials are more likely to exhibit high thermal shock resistance and enhanced dimensional stability.[1, 7, 3] Table 1 lists some common low expansion materials and their coefficients of thermal expansion.[7]

Table 1: Some common materials and their coefficients of thermal expansion.[7]

Material	Average CTE, α_l (ppm·K ⁻¹)	Range (K)
SiO ₂ glass	0.5	298–1273
SiO ₂ -TiO ₂ glasses	0.05 to -0.03	298–1073
Invar	0.01	278–303
NZP, NaZr ₂ P ₃ O ₁₂	-0.4	298–1273
Cordierite, Mg ₂ Al ₄ Si ₅ O ₁₈	1.4	298–1073
Zerodur	0.12	293–873
β -Eucryptite, Li ₂ O·Al ₂ O ₃ ·2SiO ₂	-6.2	293–1273

There are many applications where low thermal expansion materials may find use; the enhanced thermal shock resistance afforded by low expansion materials is potentially useful in automotive applications such as spark plugs (automotive spark plugs have a ceramic component that could potentially crack from thermal shock) and in cookware designed to be used in the oven and freezer.[7, 3] Likewise, the dimensional stability arising from using low thermal expansion materials may be useful in applications such as precision optics where it is necessary to preserve the original dimensions to retain the desired optical properties.[7] In all applications where low expansion materials may find use, they must not develop cracks during operation. Therefore, an ideal low expansion material would have cubic symmetry so that the thermal expansion would be equal in all directions; low expansion materials which are made from non-cubic materials may develop microcracks from internal stresses

associated with anisotropic thermal expansion.[8, 7]

Research of low expansion materials prior to World War II was centered around families of materials based upon cordierite ($2\text{MgO}\cdot 2\text{Al}_2\text{O}_3\cdot 5\text{SiO}_2$), zircon (ZrSiO_4), and Invar ($\text{Fe}_{65}\text{Ni}_{35}$).[7] Shortly following World War II, a new family of low and even negative thermal expansion materials were discovered in the lithium aluminum silicates (β -eucryptite and β -spodumene).[7, 9, 10] These materials dominated the field of low expansion materials for the next 40 years, until the discovery of the NZP ($\text{NaZr}_2\text{P}_3\text{O}_{12}$) family of materials in the early 1980s.[11]

1.3 Negative Thermal Expansion

Some materials may contradict the expected response to temperature and contract on heating.[12] Materials that exhibit contraction on heating, a phenomenon known as negative thermal expansion (NTE), have been known to exist for quite some time. The earliest observation of NTE was related to the 'density anomaly of water'; the highest density for water occurs at 277 K, therefore it displays NTE between 273–277 K.[13] The first observation of NTE in a solid was in 1907; Scheel observed negative coefficients of thermal expansion in both crystalline and glassy quartz.[13]

Following the discovery of pronounced NTE over an extended temperature range (0.3 to 1050 K) in cubic ZrW_2O_8 [14], there have been considerable research efforts surrounding NTE materials. In addition to fundamental interest in structure–property relationships, NTE materials may be useful in different engineering applications. For example, combining NTE materials with positive thermal expansion materials in composites may allow for precise control of thermal expansion, thereby making it possible to tailor the CTE for the application.[15] The ability to match CTEs is beneficial when forming an interface between materials in order to avoid cracking or separation at the interface, for instance, between a heatsink and a computer chip.[15, 3]

1.3.1 Mechanisms for Negative Thermal Expansion

There are an increasing variety of materials that possess structural features whose temperature dependence may overwhelm the lengthening of bonds and give rise to NTE. Several

different mechanisms have been proposed to explain this phenomena.[12, 6, 4]

Temperature induced structural phase transitions may give rise to NTE in some materials.[12, 4] For example, the ferroelectric material PbTiO_3 exhibits negative thermal expansion as it approaches the ferroelectric \rightarrow paraelectric phase transition at 490°C . [12] At room temperature, PbTiO_3 adopts a tetragonal structure comprised of distorted TiO_6 octahedra. Within these octahedra, the Ti atom is displaced away from the center of the coordination sphere along a four-fold axis, giving rise to three distinct Ti–O bond lengths (1.766, 2.390, and 4×1.979 Å, respectively), resulting in an average Ti–O bond length of 2.012 Å.[12] Upon heating, the distorted octahedra start to become regular octahedra. As the Ti atom moves to the center of the octahedra, the four equivalent Ti–O bonds slightly elongate while the longest Ti–O bond decreases and the shortest Ti–O bond increases. This results in a decrease of the average Ti–O bond length, giving rise to a volumetric contraction upon heating as seen in Figure 2.

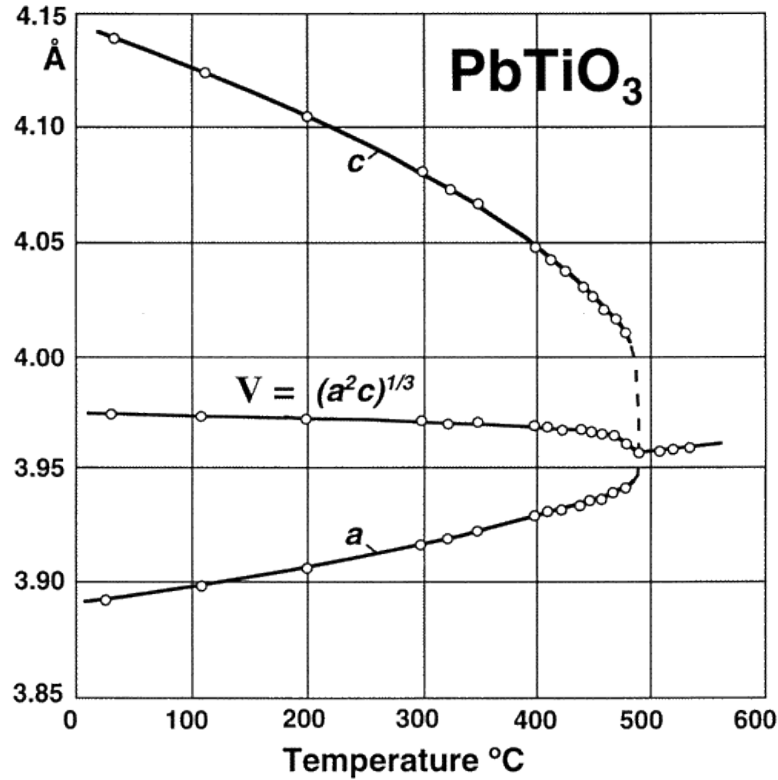


Figure 2: Unit cell edges and volume vs. temperature for PbTiO_3 . [12]

For some framework oxide materials, NTE may arise through the transverse thermal

motion of bridging oxygen atoms and can be explained using a rigid unit mode (RUM) model.[4, 16, 17] In this model, the framework material is comprised of corner sharing polyhedra which are treated as rigid units: mechanical structures having mass, moments of inertia, and translational and vibrational degrees of freedom. The only interaction between these units is at their corners (Figure 3).[18, 16]

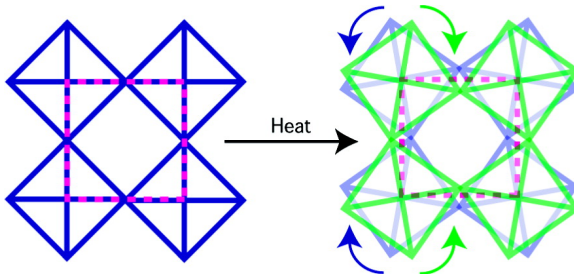


Figure 3: Negative thermal expansion can arise in framework materials through the transverse thermal motion of bridging atoms or moieties (located at the corners of the octahedra) and the associated rocking of the rigid units.

In these framework materials, the rigid units are connected together through bridging moieties (most often through a Metal–O–Metal linkage). With increasing temperature, low energy vibrational modes are populated giving rise to significant transverse thermal motion of the linking atom. This thermal motion is associated with a coupled rotation of the rigid units and may give rise to negative thermal expansion.[18, 4, 12]

1.3.2 ReO_3 Family

In elementary discussions of NTE in framework materials, the cubic ReO_3 structure is often used to explain how NTE can arise from the transverse thermal motion of bridging moieties and associated rigid unit modes.[18, 16, 4] This structure, comprised of corner sharing ReO_6 octahedra, is analogous to the ABO_3 perovskite with the *A*-site vacant (Figure 4).

Until recently, there has been disagreement in literature concerning the thermal expansion behavior of ReO_3 . Matsuno reported one of the earliest studies on the thermal expansion behavior of ReO_3 : below 340 K there was a small but negative thermal expansion in the material.[19] However, in a later review on negative thermal expansion materials, Taylor argued those findings were misleading because the reported CTEs were mean values relative to a reference temperature (300 K), whereas the instantaneous CTE was positive

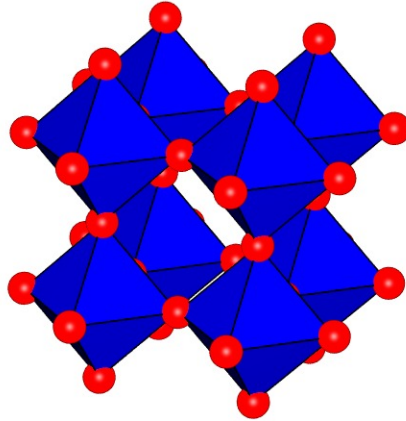


Figure 4: The cubic ReO_3 structure comprised of ReO_6 octahedra. The Re atom resides at the center of the octahedra and the oxygen atoms are located at the corners (red spheres).

for the temperature range studied.[20] These findings indicated that ReO_3 is a positive thermal expansion material; as a result, little further research was conducted with regard to its thermal expansion behavior until recently.

In 2008, Dapiaggi and Fitch reported both a negative and very small positive thermal expansion in ReO_3 from 5 to 300 K using high resolution synchrotron powder x-ray diffraction experiments.[21] Chatterji *et al.* also reported NTE in ReO_3 from 2 to 200 K as determined from powder neutron diffraction experiments.[22] Lattice dynamic calculations indicated that ReO_3 should exhibit NTE up to 350 K.[23]

These reports of NTE in ReO_3 renewed interest in the thermal expansion behavior of this material. The discrepancies between experimentally measured CTEs were later found to be a result of static disorder of the oxygen atoms, the magnitude of which depends on sample preparation.[24] It was found that the CTE for ReO_3 prepared as a single crystal was close to that originally determined by Matsuno.[24, 19]

A variety of other materials, including several metal trifluorides (MF_3 where $M = \text{Al}, \text{Ga}, \text{In}, \text{Sc}, \text{Ti}, \text{V}, \text{Cr}, \text{Mn}, \text{Fe}, \text{Co}, \text{Ir}, \text{Rh}, \text{Ru}$) and some oxyfluorides (TaO_2F , NbO_2F , and TiOF_2) have ReO_3 type structures.[25, 26, 27] With the exception of ScF_3 and MnF_3 ,

all of the metal trifluorides adopt a rhombohedral structure at room temperature that 'unfolds' upon heating; this leads to a strong positive thermal expansion, and in some cases, a phase transition to the cubic structure at high temperatures.[26, 28, 29, 30, 31, 32] Scandium trifluoride (ScF_3), which adopts the cubic ReO_3 structure type at room temperature, was recently reported to exhibit pronounced negative thermal expansion across a broad temperature range and is discussed in detail in Chapter 2 of this thesis.[33]

There are several oxyfluorides (NbO_2F , TaO_2F , and TiOF_2) which have been reported to adopt the cubic ReO_3 structure.[34, 27] The thermal expansion properties of TaO_2F were examined by Tao and Sleight; the coefficients of thermal expansion reported were so small that the material could be classified as a zero-expansion material.[35] In this oxyfluoride, there is no long range order in the arrangement of the O and F across the available anionic sites; analysis of the thermal parameters and local structural data for these disordered materials suggests that there is static disorder of those anions, just as was observed in ReO_3 . [35, 24] The lack of pronounced NTE in ReO_3 and TaO_2F has been attributed to the presence of this static disorder, such that when the $M\text{-}X\text{-}M$ ($M = \text{Re}, \text{Ta}; X = \text{O}, \text{F}$) bond angle deviates from 180° , the transverse thermal motion is enough to offset positive thermal expansion associated with bond length elongation but not sufficient to give rise to NTE.[24]

1.3.3 NTE Materials Under Pressure

The same structural features that can give rise to NTE, flexible open frameworks, can also give rise to interesting behavior under pressure.[4, 12, 36, 37] One potential application for NTE materials is their use in controlled thermal expansion composites.[15] However, the manufacture and use of such composites may subject the materials to stresses that can induce phase transitions or alter the thermal expansion behavior of the material.[38] An understanding of the behaviors of NTE materials under pressure is important when considering their use.

The effect of pressure on materials can be studied using diffraction techniques. There are a variety of high pressure sample environments that allow the application of hydrostatic

pressure on the sample for both *in situ* and *ex situ* studies. Diamond anvil cells (DACs), which apply pressure by squeezing the sample between two diamond faces (Figure 5), allow for *in situ* X-ray diffraction studies to very high pressures (>100 GPa).[39] High pressure gas (typically helium) cells exist which can apply precisely measured hydrostatic pressures and can be easily cooled for variable temperature–pressure neutron diffraction studies.[40]

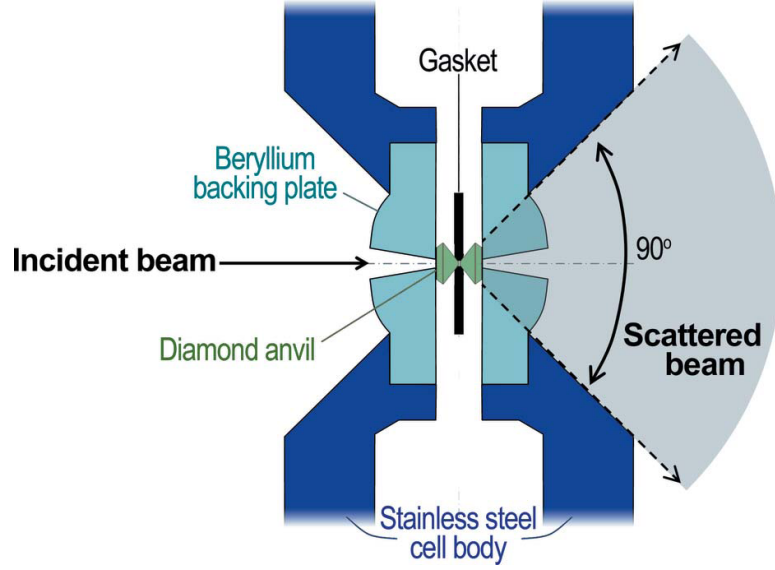


Figure 5: Schematic of a Diacell-Bragg type diamond anvil cell. The sample is held in a small hole in the gasket, and pressure is applied by squeezing the two diamonds.[39]

When studying the effects of pressure on materials using diffraction, the unit cell volume is typically extracted from the diffraction data and plotted with respect to pressure. The bulk modulus, K , can be calculated from the pressure dependence of the unit cell volume and provides a quantitative measure of how elastically soft a material is. The isothermal bulk modulus is defined as:[1]

$$K_T = -V \left(\frac{\partial P}{\partial V} \right)_T \quad (4)$$

The bulk modulus is the reciprocal of the isothermal compressibility. A pressure dependence of the volumetric coefficient of thermal expansion (α_V) exists, and it is related to the temperature dependence of the isothermal bulk modulus by:[41]

$$\left(\frac{\partial \alpha_v}{\partial p} \right)_T = \frac{1}{K_T^2} \left(\frac{\partial K_T}{\partial T} \right)_p \quad (5)$$

Experimental and theoretical studies of the temperature dependence of the isothermal bulk

modulus, $(\frac{\partial K_T}{\partial T})_p$, show that it is typically negative, which implies that the CTE usually decreases upon compression.[42]

In the case of NTE materials, high pressure effects such as phase transitions and pressure induced amorphization have been observed. One of the most widely studied NTE materials, cubic ZrW_2O_8 , undergoes a pressure-induced structural phase transition from cubic→orthorhombic symmetry at ≈ 0.2 GPa.[43, 44] The thermal expansion properties of these two phases differ considerably ($\alpha_l = -9$ ppm·K⁻¹ for the cubic phase, $\alpha_l = -1$ ppm·K⁻¹ for the orthorhombic phase).[43, 44] Holzer *et al.* explored the feasibility of making a metal matrix composite using copper metal and cubic ZrW_2O_8 ; such a composite should have low thermal expansion and high thermal conductivity, which would be ideal for applications such as heat sinks for electronic components.[38] However, the cubic→orthorhombic phase transition in ZrW_2O_8 was observed, arising from stresses encountered during the processing or from the mismatches between the CTEs of the filler and matrix.[38]

The effects of pressure on TaO_2F , a zero expansion material with the cubic ReO_3 structure, were examined by Cetnikol *et al.* Two phase transitions were observed, one occurring at ≈ 0.7 GPa, and a second at 4.0 GPa; the first is broadly consistent with a rhombohedral VF_3 structure type, while the second is fully consistent with the rhombohedral VF_3 structure.[45] In ReO_3 type materials, such symmetry lowering transitions can readily occur from rotation of the rigid octahedra into the void space.

Pressure induced amorphization has also been observed in a number of framework materials that exhibit NTE (Table 2).[46] During this process, long range order of the crystalline phase is lost, resulting in an amorphous material. Unlike most crystalline to crystalline structural phase transitions, which may be reversible upon release of pressure, the starting crystalline structure is typically not recovered on pressure release.[46]

Table 2: List of negative thermal expansion framework materials and their amorphization pressures. [46]

Compound	Transition Pressure (GPa)
ZrW ₂ O ₈	1.5
HfW ₂ O ₈	2
ZrV ₂ O ₇	4
ZrMo ₂ O ₈	8
Sc ₂ (WO ₄) ₃	4
Lu ₂ (WO ₄) ₃	7
Al ₂ (WO ₄) ₃	10
Gd ₂ (MoO ₄) ₃	6
Sm ₂ (MoO ₄) ₃	6
Eu ₂ (MoO ₄) ₃	7

CHAPTER II

PRONOUNCED NEGATIVE THERMAL EXPANSION IN ScF_3

2.1 *Introduction*

The simple cubic ReO_3 structure type is often used to illustrate how NTE can arise through the transverse thermal motion of bridging atoms or moieties and the associated rigid unit vibrational modes (Figure 6).[18, 16] However, ReO_3 itself does not display NTE at room temperature and only shows modest NTE ($\alpha_l = \frac{1}{l} \frac{dl}{dT} \approx -1 \text{ ppm}\cdot\text{K}^{-1}$) at low temperatures (15–294 K).[23, 21, 24] The absence of NTE in ReO_3 at room temperature may be related to the delocalization of rhenium’s single d -electron in the conduction band.[23] ReO_3 contains highly covalent Re–O bonds formed from Re $5d$ and O $2p$ orbitals; the covalent nature of these Re–O bonds may contribute to the lack of NTE in this material.[23] The absence of pronounced NTE in ReO_3 has sparked recent searches for other ReO_3 -type materials that do display NTE.

There are several metal trifluorides (MF_3 , $M = \text{Al, Ga, In, Sc, Ti, V, Cr, Mn, Fe, Co, Ir, Rh, Ru}$) that have ReO_3 -type structures.[25, 26, 27] With the exception of ScF_3 (and Jahn-Teller distorted MnF_3), all of these metal trifluorides adopt a rhombohedrally-distorted structure at room temperature. This structure ‘unfolds’ upon heating, as seen in Figure 7, which leads to strong positive thermal expansion.[28, 29] In some cases, a phase transition occurs from the rhombohedral to the cubic ReO_3 structure at elevated temperatures (greater than room temperature).[26, 28, 29, 30, 31, 32]

Scandium trifluoride has been previously reported as being either rhombohedral or cubic.[47, 48] Melnikov *et al.* indicated that ScF_3 exhibits NTE, but thermal expansion data has not been reported until now.[49]

2.2 *Experimental*

Scandium trifluoride was used as supplied by American Elements (99.99% metals basis).

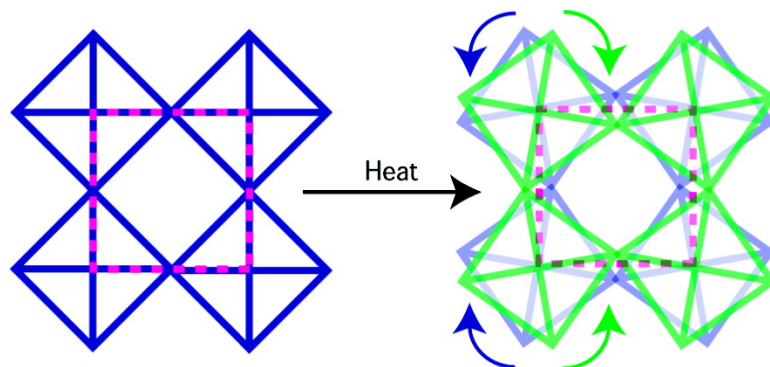


Figure 6: Negative thermal expansion can arise in the cubic ReO_3 structure type through the transverse thermal motion of bridging atoms (located at the corners of the octahedra) and the associated rocking of rigid units.

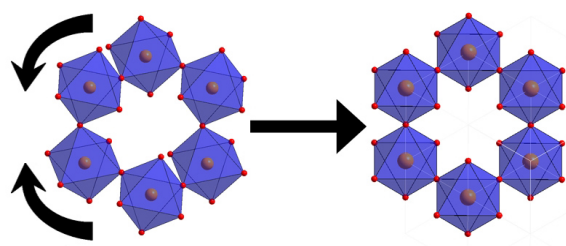


Figure 7: Two layers of octahedra in the rhombohedral (left) and cubic (right) ReO_3 structure types (viewed down $[1\ 1\ 1]$), illustrating the phase transition mechanism. In the case of heating, the rhombohedral structure 'unfolds' into the cubic structure type, and under pressure the octahedra can tilt, transforming a cubic structure into a rhombohedral one.

2.2.1 Variable Temperature Diffraction Studies

The temperature-dependent unit cell volume of ScF_3 was initially examined by powder X-ray diffraction at beamline 1-BM-C of the Advanced Photon Source, Argonne National Laboratory. A wavelength of 0.6183 Å (as calibrated using a NIST Si powder standard) was selected using a Si(111) double-crystal monochromator, and the diffraction images were recorded on a Mar345 imaging plate detector. The sample to detector distance (≈ 200 mm), beam center, tilt plane rotation angle, and tilt angle were calibrated from a LaB_6 (NIST SRM 660a) diffraction pattern using the program Fit2D.[50]

Low temperature X-ray diffraction data were collected with the samples held in Kapton capillary tubes. The temperature was cycled between 120 and 500 K multiple times at a rate of 180 K/hr using an Oxford Cryosystems liquid nitrogen cryostream. Subsequent higher temperature diffraction data (333 – 1073 K) were collected using a wire-wound furnace for temperature control.[51]

The temperature range was extended (>1600 K) by using high energy X-rays (≈ 90 keV) at beamline 11-ID-B of the Advanced Photon Source to study the sample sealed in a platinum capillary within a Linkam TS1500 furnace. Diffraction data were recorded on a Perkin-Elmer amorphous silicon detector. The temperature calibration of the furnace was checked by monitoring the thermal expansion of an α -alumina sample.

Low temperature (10 – 280 K) neutron powder diffraction data were collected on beamline HB2A at the High Flux Isotope Reactor, Oak Ridge National Laboratory. The sample was held in an aluminum-bodied helium gas pressure cell, and temperature was controlled using a closed-cycle helium refrigerator. A wavelength of 1.117544 Å was selected using a Ge(117) crystal monochromator and was calibrated using a NIST Si powder diffraction standard.

2.2.2 High Pressure Diffraction Studies

High pressure diffraction data were collected *in situ* at ambient temperature and from ambient pressure to ≈ 6 GPa at beamline 1-BM-C of the Advanced Photon Source. A Diacell Bragg diamond anvil cell (DAC), equipped with diamonds having 500 μm culets,

was used; the samples were loaded into $300\mu\text{m}$ holes which had been EDM drilled into preindented stainless steel gaskets ($250\mu\text{m}$ thickness). A 4:1 methanol:ethanol mixture was used as the pressure transmitting medium to ensure hydrostatic compression and the ruby fluorescence technique was used for pressure calibration.[52]

High pressure-high temperature diffraction data were collected *in situ* at beamline 1-BM-C of the Advanced Photon Source using a hydrothermal diamond anvil cell (HDAC) equipped with diamonds having $600\mu\text{m}$ culets. The samples were loaded into $300\mu\text{m}$ holes which had been predrilled in rhenium gaskets. The HDAC was sealed under liquid argon which was used as a pressure transmitting medium to ensure hydrostatic compression. Data were collected from ambient to ≈ 2 GPa across a series of temperatures from ambient to ≈ 690 K. Pressure was calibrated by using NaCl as an internal standard.

Low temperature-high pressure diffraction data were collected using a helium gas pressure cell inside of a helium refrigerator at beamline HB2A of the High Flux Isotope Reactor, ORNL. Diffraction data were collected at ambient pressure from 10 to 280 K, and at 0.1, 0.2, and 0.3 GPa from 50 to 280 K.

2.3 Results

Diffraction data from the cryostream and wire-wound furnace variable temperature experiments were analyzed using the Rietveld method as implemented in GSAS with the EXPGUI interface.[53, 54] The batch mode of GSAS, SEQGSAS, was utilized to analyze the diffraction data. During analysis, the unit cell parameters, thermal parameters, background, and a pseudo-Voigt peak shape model (GW, GU, GV, LX, and LY) were refined. Representative Rietveld fits are shown in Figures 8 and 9.

The high temperature data from the Linkam furnace was analyzed using the Rietveld method in GSAS. There was a considerable amount of scattering from the platinum capillary, making it necessary to exclude portions of the diffraction data overwhelmed with Pt Bragg reflections. During analysis, the unit cell parameters, background, and a single Gaussian peak shape parameter were refined from a fit to seven ScF_3 Bragg reflections (Figure 10).

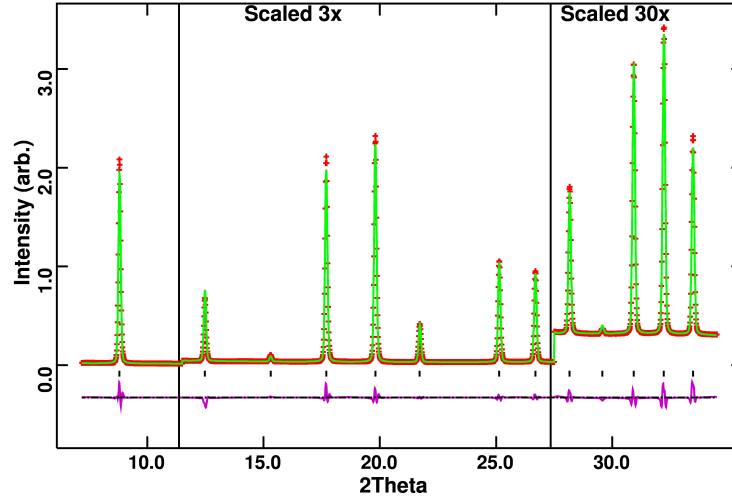


Figure 8: Rietveld fit (green line) to the first (room temperature) diffraction pattern (red +) collected during the variable temperature cryostream experiment. This fit was used to initialize the batch mode processing of the remaining cryostream data. The regions between 11.5 – 27.5 2θ were multiplied by 3 and 27.5–34.5 2θ by 30 to better show fit quality at high angles.

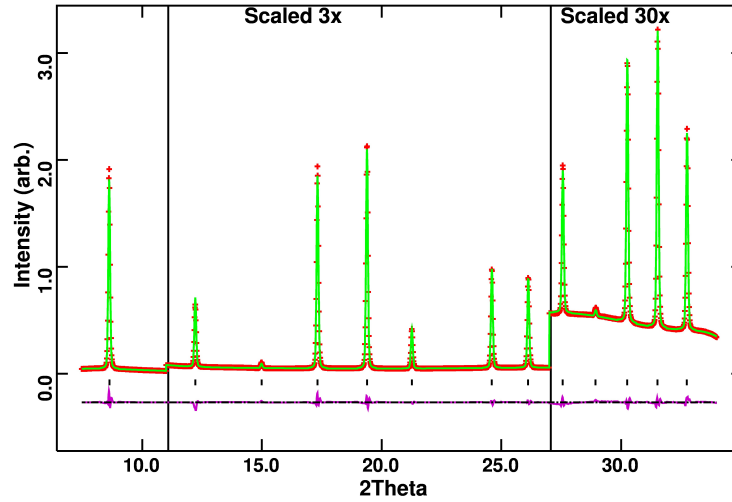


Figure 9: Rietveld fit (green line) to the first (room temperature) diffraction pattern (red +) collected during the variable temperature wire-wound furnace experiment. This fit was used to initialize the batch mode processing of the remaining wire-wound furnace data. The regions between 11–27 2θ were multiplied by 3 and 27–34 2θ by 30 to better show fit quality at high angles.

The neutron diffraction data was analyzed using a combination of Le Bail and Rietveld analysis as implemented in Fullprof.[55] As seen in Figure 11, the diffraction patterns were dominated by scattering from the aluminum pressure cell. A Le Bail fit was utilized to fit the aluminum diffraction peaks, while a Rietveld fit was simultaneously utilized on the ScF_3 diffraction peaks. The lattice parameters for ScF_3 and a four term Thompson-Cox-Hastings pseudo Voigt were refined. The intense scattering from the aluminum prevented refinement of other parameters.

2.3.1 Temperature Dependence of Unit Cell Dimensions

The lattice constants, extracted from Rietveld analyses of the diffraction data, were plotted with respect to temperature (Figure 12). The lattice constants from the different experiments were scaled linearly to account for experimental calibration discrepancies arising from sample to detector distances, etc. The coefficient of thermal expansion (CTE) was derived using a smoothing spline fit to the lattice constants against temperature data.

2.3.2 High Pressure Behavior

The high pressure diffraction data were analyzed using the Rietveld method. A pressure-temperature phase diagram was constructed based upon the analyses of the variable temperature neutron diffraction data and the hydrothermal diamond anvil cell X-ray diffraction data (Figure 13). The two phases present are the cubic ReO_3 type structure (space group $Pm\bar{3}m$, no. 221) and a rhombohedral distortion of the cubic phase (space group $R\bar{3}c$, no. 167).

From the high pressure diffraction data collected using a Diacell-Bragg DAC, the bulk modulus was estimated to be 55(2) GPa for the cubic phase using a straight line fit through the available data; for the rhombohedral phase the bulk modulus was estimated from a 4th-order Birch-Murnghan equation of state fit to the available data. During the equation of state fit, V_0 and K_0 , K_p , and K_{pp} were all refined. The resulting equation of state fit is illustrated in Figure 14, and the fit results are summarized in Table 3.

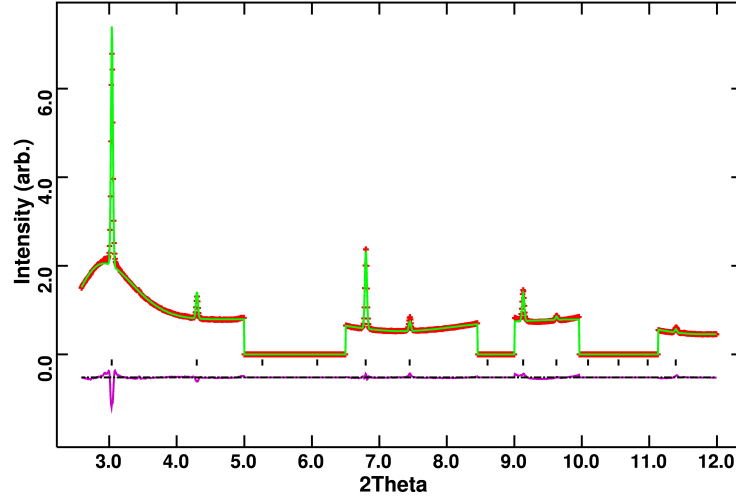


Figure 10: Rietveld fit (green line) to the first (room temperature) diffraction pattern (red +) collected during the high temperature Linkam furnace experiment. Regions with large amounts of scattering from the platinum capillary were excluded.

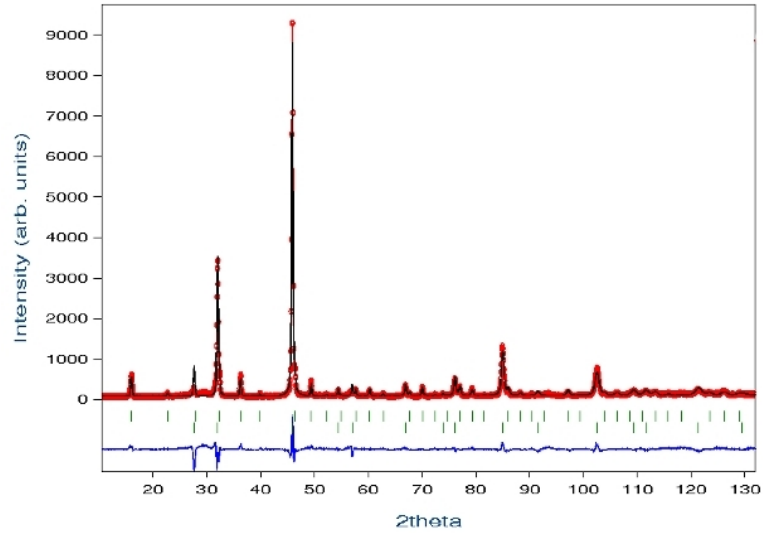


Figure 11: Rietveld (ScF_3) and Le Bail (Al) fits (black line) to the first diffraction pattern (red \circ) collected during the variable pressure-temperature neutron powder diffraction experiment on ScF_3 contained in an Al-pressure cell. The bottom reflection markers (green |) correspond to the Bragg reflections from the aluminum sample cell, whereas the top reflection markers are the ScF_3 Bragg reflections.

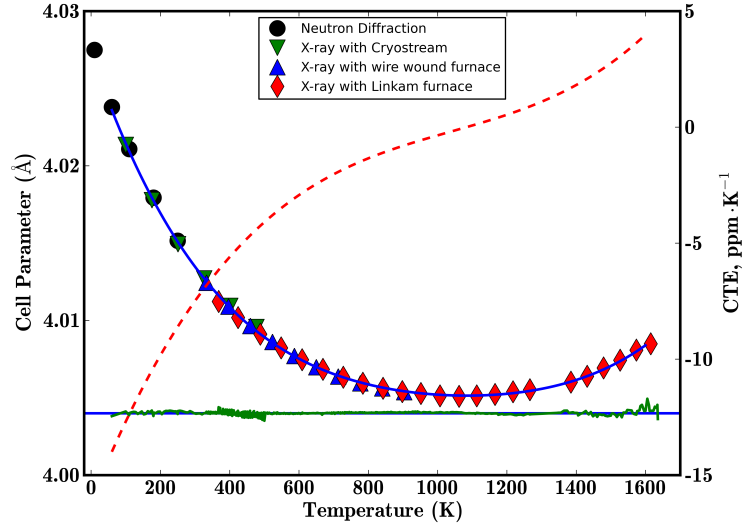


Figure 12: Selected experimentally-determined lattice constants for cubic ScF_3 (solid symbols), along with a smoothing spline fit (blue line) to nearly all the available values for ≥ 60 K (some at ≈ 1350 K were excluded as outliers). The ESDs for the lattice constants are comparable to the symbol sizes. The difference between the experimentally determined lattice constants and the spline fit is shown as a green line. The lattice constants from different measurements are scaled linearly to account for calibration discrepancies. The linear CTE, derived from the spline fit, is shown as a dashed red line.

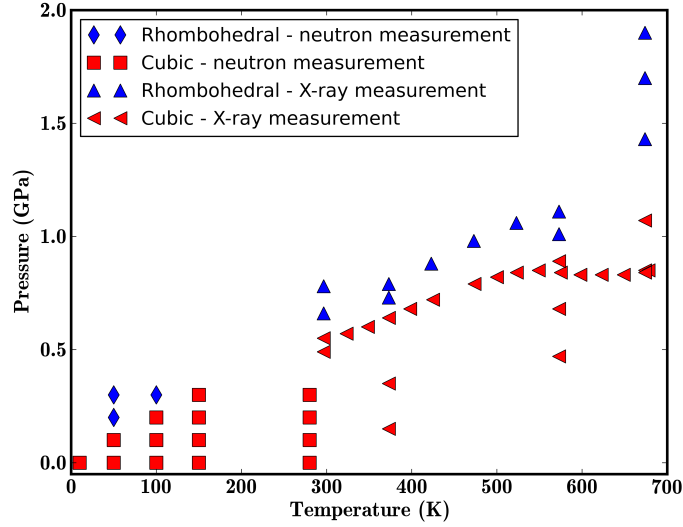


Figure 13: Pressure-temperature phase diagram for ScF_3 . Under pressure, the octahedral tilts fold the structure so that it is more compact and reduces the symmetry from cubic to rhombohedral.

Table 3: Equation of state fit results to ScF₃ Rhombohedral Phase.

EqS Fit Statistics	$R_w=1.4454\%$, $\chi^2=0.0038$
V_0	135(4)
K_0	9(3)
K_p	-2.9(9)
K_{pp}	1(1)

2.4 Discussion

The lattice constants derived from the variable temperature diffraction data for ScF₃ show that the CTE is strongly and smoothly dependent on temperature. At room temperature, the CTE ($\alpha_l \approx -8\text{ppm}\cdot\text{K}^{-1}$) is similar to that of cubic ZrW₂O₈ ($\alpha_l \approx -9\text{ppm}\cdot\text{K}^{-1}$), and ScF₃ shows an even more pronounced NTE at lower temperatures. The CTE approaches zero at ≈ 1100 K and becomes positive at higher temperatures. Upon cooling to 10 K, ScF₃ remained cubic and displayed a CTE ($\alpha_l \approx -14\text{ppm}\cdot\text{K}^{-1}$, 60 - 110 K) that is more negative than that of nearly all materials whose NTE arises from vibrational motion (with the exception of those with many more vibrational degrees of freedom, e.g. Zn/Cd(CN)₂). [56, 57] The temperature range over which ScF₃ exhibits NTE is much larger than that found for materials whose NTE arises from magnetostrictive effects [58, 59] or valence state changes [60].

The pronounced negative thermal expansion found in ScF₃ is consistent with a rigid unit mode (RUM) model. This may involve the same R₅ mode that has been implicated in the cubic to rhombohedral phase transition seen in many metal trifluorides. [26] This mechanism is supported by the large, strongly temperature dependent transverse component of the anisotropic displacement parameters for the bridging fluorine atoms (Figure 15). However, the factors underlying the pronounced, continuous variation in the CTE are less obvious. It is unlikely that expansion of the individual Sc – F bond lengths alone would be sufficient to produce the observed change in CTE. However, a change in the rocking motion of the ScF₆ rigid octahedra upon heating could contribute to the variations in the CTE. This may also incorporate a contribution to the CTE from static disorder as has been previously suggested for AlF₃ above its rhombohedral-to-cubic phase transition (the Al-F-Al links in AlF₃ are locally bent in the cubic phase). [28, 32]

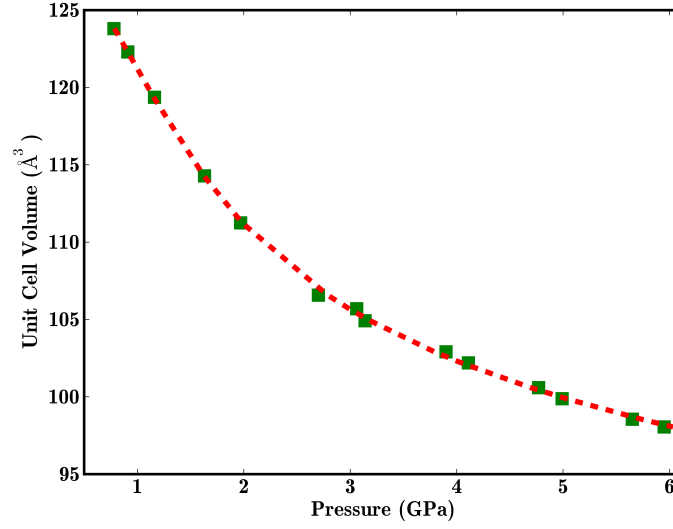


Figure 14: Fourth order Birch Murnghan Equation of State (red dashed line) fit to the available unit cell volume–pressure data (green squares) for the high pressure rhombohedral phase of ScF_3 .

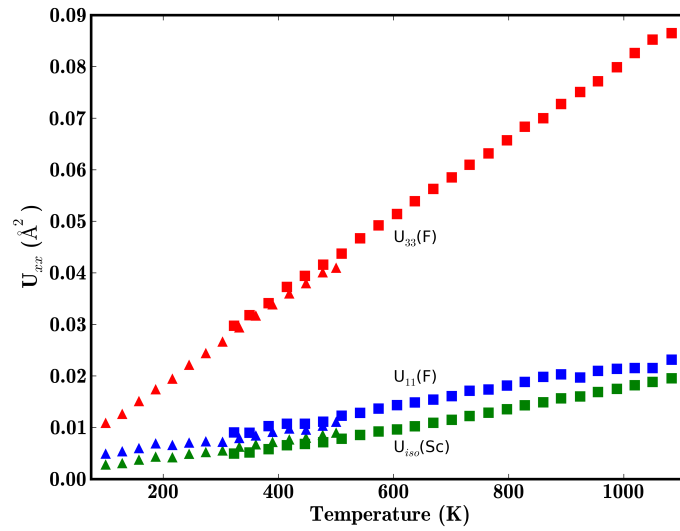


Figure 15: Atomic displacement parameters for ScF_3 extracted from Rietveld analysis of the Cryostream (triangles) and wire-wound furnace (squares) variable temperature data.

Most metal trifluorides with ReO_3 type connectivity are unstable with respect to a static-correlated rotation ($a^-a^-a^-$ type rotation in Glazer notation) of the corner-sharing MF_6 octahedra that comprise the framework structure.[61] This rotation leads to rhombohedral symmetry ($R\bar{3}c$, no. 167) and a smaller volume per formula unit. At ambient temperature, ScF_3 transforms from cubic to rhombohedral symmetry between ~ 0.5 and ~ 0.8 GPa (Figure 13). This observed phase transition is consistent with previous high-pressure micro Raman studies, which reported the phase transition as occurring at ~ 0.7 GPa.[48] The high pressure X-ray measurements suggest a bulk modulus for cubic ScF_3 of 55(2) GPa, which is close to the 70 GPa estimated in previous Raman work.[48]

2.5 Conclusions

The first full characterization of ScF_3 's thermal expansion behavior revealed several striking features. First, there is prominent NTE at temperatures below 300 K that is more pronounced than that of most known NTE materials. Second, there is a slow, smooth evolution toward positive thermal expansion above 1100 K. Finally, a very simple crystal structure is maintained. These behaviors arise, in part, because ScF_3 does not undergo a symmetry-lowering phase transition upon cooling unlike most ReO_3 type materials; this may arise because the bonding in ScF_3 is less covalent than that in many related MF_3 phases, and the cubic structure is electrostatically favored over the rhombohedral structure since the separation between ions of the same charge is maximized for a given $M\text{--F}$ bond length.

2.6 Supplemental Information

Table 4: ScF₃ unit cell parameters as a function of pressure. α is the primitive rhombohedral unit cell angle, and is listed as N/A for the cubic phase of ScF₃.

<i>Pressure</i> (GPa)	<i>a</i> Å	α	<i>Vol.</i> Å ³
0	4.01260(7)	N/A	64.607(3)
0.11	4.00924(6)	N/A	64.445(3)
0.25	4.00643(7)	N/A	64.309(3)
0.51	3.99992(7)	N/A	63.996(3)
0.78	5.6281(4)	59.216(4)	123.81(1)
0.91	5.6212(4)	58.844(4)	122.29(1)
1.16	5.6091(3)	58.102(5)	119.36(1)
1.63	5.5938(4)	56.682(5)	114.29(1)
1.97	5.5867(2)	55.784(3)	111.24(1)
2.70	5.5784(2)	54.349(3)	106.57(1)
3.06	5.5780(6)	54.056(8)	105.69(1)
3.14	5.5755(4)	53.840(5)	104.91(1)
3.90	5.5678(5)	53.302(6)	102.91(1)
4.11	5.5643(6)	53.121(6)	102.19(1)
4.77	5.5536(7)	52.771(7)	100.59(1)
4.99	5.5465(8)	52.657(7)	99.87(1)
5.65	5.5367(6)	52.383(6)	98.55(1)
5.95	5.5328(5)	52.280(5)	98.04(1)

CHAPTER III

SYNTHESIS AND CHARACTERIZATION OF TITANIUM OXYFLUORIDE AND TITANIUM OXYHYDROXYFLUORIDES

3.1 Introduction

Titanium oxyfluoride (TiOF_2) was first synthesized and reported to adopt the cubic ReO_3 type structure, shown in Chapter 1 Figure 4, over 50 years ago.[62, 27] In this material, fluoride and oxide are disordered over the available anion sites. Over the years, there have been studies examining its refractive index and potential for use as a UV absorber [63], potential as an anode material in Li-ion batteries [64], and use as a visible light photocatalyst for water oxidation.[65]

There has, however, been some uncertainty in the literature surrounding the actual stoichiometry of TiOF_2 . In the earliest reports on this material, TiOF_2 was prepared by either hydrolysis of TiF_4 or digestion of TiO_2 in aqueous hydrofluoric acid (HF) followed by evaporation to dryness.[62] Initial characterization of the resulting material was performed using only powder X-ray diffraction (PXRD), which suggested that the material was TiOF_2 with the cubic ReO_3 structure. However, a later report by Dehnicke suggested that the material possessed a significant number of hydroxyl groups based on infrared (IR) spectral analysis.[66] Using both IR and powder X-ray diffraction, Dehnicke proposed that the material was actually $\text{TiO}(\text{OH})\text{F}$; since X-rays are scattered by electrons, OH^- and F^- would be almost indistinguishable using XRD because they have the same number of electrons.[66]

Following these reports, several researchers have subsequently attempted to synthesize TiOF_2 free of any hydroxyl impurities using different approaches. It was reported by Moss and Wright that preparation of TiOF_2 by digestion of TiO_2 in aqueous HF followed by heating to 450°C would remove all OH bands from IR spectra, but would leave a material with TiO_2 impurities.[67] Moss and Wright also reported the synthesis of TiOF_2 by heating TiO_2 with TiF_4 , but they noted that the reaction was difficult to take to completion and

may result in the formation of Ti_2OF_6 . [67] Mel'nichenko *et al.* explored the impact of 'heat treatments' on ' TiOF_2 ' prepared from the digestion of TiO_2 in HF using a combination of powder X-ray diffraction, IR spectral analysis, and fluoride content determination. They reported a stoichiometry of $\text{TiO}(\text{OH})_{0.2}\text{F}_{1.8}$ when samples were dried under vacuum at temperatures less than 400°C , and $\text{TiO}_{1.1}\text{F}_{1.8}$ when dried at 400°C . [68] In their analyses, hydroxyl groups were used to maintain charge balance to compensate for the lower than expected fluoride content.

In a recent study, Shian *et al.* prepared TiOF_2 from the reaction of silica microspheres with TiF_4 gas generated inside sealed titanium ampoules. [69] The authors reported a rhombohedrally-distorted ReO_3 structure at room temperature that undergoes a phase transition to the cubic ReO_3 structure at around 340 K. [69] In a quest for an improved UV absorber, Demourgues *et al.* synthesized and characterized a titanium hydroxyfluoride, $\text{Ti}_{0.75}(\text{OH})_{1.5}\text{F}_{1.5}$, prepared via microwave synthesis, which also adopts the cubic ReO_3 structure. [70] This was the first report of a titanium hydroxyfluoride that contains Ti vacancies and adopts the cubic ReO_3 type structure.

Even though ReO_3 itself does not show appreciable NTE, ScF_3 which adopts the cubic ReO_3 structure type has been recently reported to exhibit NTE behavior. [33] It has also been reported that TaO_2F , which adopts the cubic ReO_3 structure type, exhibits 'zero' thermal expansion across a broad temperature range. [35] Titanium oxyfluoride (TiOF_2) has also been reported by some workers to adopt the ReO_3 structure type. [62, 27] The somewhat confusing literature combined with interest in the thermal expansion of ReO_3 type materials motivated us to further examine both synthetic avenues and properties of the materials at non-ambient temperatures and pressures. The traditionally proposed synthetic method of digesting TiO_2 in aqueous HF has been reexamined and the materials' true chemical identity readdressed; a synthetic approach involving the direct reaction of TiO_2 with TiF_4 is also characterized.

3.2 *Experimental*

3.2.1 Syntheses

Titanium hydroxyoxyfluorides ($\text{Ti}_{1-x}(\text{O}/\text{OH}/\text{F})_3$) were prepared using the synthetic procedure for TiOF_2 reported by Vorres and Dutton.[62] Finely ground TiO_2 (anatase, STREM Chemicals, 99% metals basis) was combined with aqueous HF (at least 48% HF by weight, but not greater than 60%, Mallinckrodt) in a PTFE beaker. The reaction mixture was stirred over low heat (≈ 353 K) until all of the HF had evaporated. The resulting white powder was collected and vigorously washed with distilled water followed by rinsing with acetone.

TiOF_2 was prepared using a low temperature solid state reaction between TiO_2 and TiF_4 (Alfa Aesar, 98% metals basis). The starting reagents (including 15% excess TiF_4 over that required by stoichiometry) were combined in an argon-filled glove box using a mortar and pestle. The reaction mixture was sealed inside of a copper tube fitted with brass Swagelok compression fittings to create an air-tight vessel. The mixture was heated at 493 K for 18 hours followed by quenching in water to room temperature.

3.2.2 Sample Characterization

Room temperature powder X-ray diffraction (PXRD) data were collected from 5–120 degrees 2θ at a rate of $0.1^\circ/\text{min}$ on a Scintag X1 diffractometer using Cu K_α radiation and a Peltier cooled solid state detector. The diffraction patterns were compared with the ICDD database using Jade, and structural refinement was performed by using the Rietveld method as implemented in GSAS with the EXPGUI interface.[53, 54]

The densities of powdered samples were measured using a Micromeritics AccuPyc II 1340 gas pycnometer and ultra high purity helium. The sample cell was purged 200 times to help ensure a sample free of adsorbed moisture, and the average volume was obtained from 20 sequential measurements. The fluoride contents of both materials were determined using pyrohydrolysis by Galbraith Laboratories (Knoxville, TN).

Thermogravimetric analysis (TGA) was performed using a Perkin Elmer TGA-7 equipped with a high temperature furnace attachment. Argon was used as the purge gas during all

measurements; however, no special precautions were taken to maintain an anhydrous environment. A small amount of sample (≈ 20 mg) was placed into a platinum weighing pan and data were collected from ambient temperature to 1273 K at a rate of 5 K/min.

IR spectra were obtained by attenuated total reflectance (ATR) through a diamond plate using a Bruker Optics Alpha-P Fourier transform infrared (FTIR) spectrometer. The samples were stored in a desiccator with Drierite overnight prior to analysis and were examined without further preparation.

3.2.3 Non-Ambient Diffraction Studies

In situ powder diffraction data were collected using beamline 1-BM-C at the Advanced Photon Source (APS), Argonne National Laboratory. X-rays (≈ 20 keV) were selected using a Si(111) double-crystal monochromator, and the wavelengths were calibrated using a NIST Si powder sample. Diffraction patterns were recorded on a Mar345 imaging plate detector. The sample to detector distance (≈ 200 mm), beam center, tilt plane rotation angle, and tilt angle were calibrated from a LaB_6 (NIST SRM 660a) diffraction pattern.

Low temperature data were recorded with the samples held in Kapton capillary tubes. The temperature was cycled from 120–500 K multiple times at a rate of 180 K/hr using an Oxford Cryosystems liquid nitrogen cryostream. High temperature data were collected with the samples held in a quartz capillary mounted in a flow cell equipped with wire wound resistance heaters.[51] The temperature was increased from 303–1173 K at a rate of 180 K/hr.

High pressure diffraction data were collected at ambient temperature using a Diacell Bragg (easyLab Technologies Ltd.) diamond anvil cell equipped with diamonds having $500\mu\text{m}$ culets. The samples were loaded into $300\mu\text{m}$ holes which had been EDM drilled into preindented stainless steel gaskets ($250\mu\text{m}$ thickness). A 4:1 methanol:ethanol mixture was used as the pressure transmitting medium to ensure hydrostatic compression, and the ruby fluorescence technique was used for pressure determination.[52] Data were collected from ambient pressure to ≈ 9 GPa.

The two-dimensional diffraction images from the Mar345 detector were integrated using the program Fit2D.[50] Structural information and lattice constants were obtained by Rietveld analysis of the integrated diffraction patterns using the program GSAS with the EXPGUI interface.[53, 54] The sequential processing mode within GSAS (SEQGSAS) was used to allow batch processing of the variable temperature diffraction patterns.

3.3 Results

3.3.1 Phase Purity and Room Temperature Crystal Structure

The powder diffraction patterns collected for the materials prepared using both synthetic routes were initially analyzed using the Rietveld method assuming a cubic ReO_3 -structure type (space group no. 221, $Pm\bar{3}m$).[62] Diffraction patterns collected for TiOF_2 under ambient conditions showed a single Bragg reflection ($d = 2.29\text{\AA}$) that is not symmetry-allowed for the $Pm\bar{3}m$ structure. Symmetry lowering may occur in perovskites arising from octahedral tilts; therefore diffraction patterns possessing the extra Bragg reflection were subsequently analyzed using the lower symmetry rhombohedral space group $R\bar{3}c$ (Figure 16).

As shown in Figure 17, the $\text{Ti}_{1-x}(\text{O}/\text{OH}/\text{F})_3$ samples were all single phase with cubic ReO_3 ($Pm\bar{3}m$) type symmetry. However, TiOF_2 samples contained a trace amount (less than 1% by weight, as determined by quantitative Rietveld analysis) of TiO_2 (anatase) impurity. During analyses of the diffraction data, the unit cell parameters, sample height displacement, pseudo-Voigt profile parameters, background, and thermal parameters for Ti and randomly distributed O/F (constrained to be identical to one another) were refined. During the analysis of the diffraction data for TiOF_2 using the rhombohedral space group, the O/F positions in the unit cell were refined. The site occupancy for Ti was also refined during analysis of the diffraction data for $\text{Ti}_{1-x}(\text{O}/\text{OH}/\text{F})_3$; while the refinement of site occupancy is highly correlated to the atomic displacement parameters, it resulted in a calculated density that was in good agreement with that measured experimentally. The results from the Rietveld refinements are presented in Tables 5 and 6.

The measured densities for TiOF_2 and $\text{Ti}_{1-x}(\text{O}/\text{OH}/\text{F})_3$ were 3.102(6) and 2.924(2)

$\text{g}\cdot\text{cm}^{-3}$, respectively. The measured fluoride content from three replicate measurements of TiOF_2 and $\text{Ti}_{1-x}(\text{O}/\text{OH}/\text{F})_3$ were 43.3, 42.5, 42.7 and 41.1, 40.9, 40.9% by weight, respectively. The expected fluoride content in TiOF_2 is 37.3% by weight. The measured density of TiOF_2 is consistent with that expected for TiOF_2 with rhombohedral symmetry ($3.118 \text{ g}\cdot\text{cm}^{-3}$), and the measured density for $\text{Ti}_{1-x}(\text{O}/\text{OH}/\text{F})_3$ is consistent with the presence of $\approx 15\%$ Ti vacancies.

3.3.2 Thermogravimetric and IR Spectral Analysis

The thermogravimetric weight loss curves for both materials are presented in Figure 18. TiOF_2 displays a single weight loss of $\approx 19.5\%$ beginning at $\approx 500 \text{ K}$ and ending at $\approx 600 \text{ K}$. The thermal decomposition of $\text{Ti}_{1-x}(\text{O}/\text{OH}/\text{F})_3$ occurs in two stages, beginning at $\approx 440 \text{ K}$ and ending at $\approx 740 \text{ K}$, resulting in an overall weight loss of $\approx 30\%$. The end products of both decompositions were confirmed to be TiO_2 (anatase) by powder X-ray diffraction.

The IR spectra collected for both materials are presented in Figure 19. There are three distinct features characteristic of O–H vibrations present in the spectrum for titanium hydroxyoxyfluoride that indicate the presence of hydroxyl groups. First, there is a broad peak centered around 3300 cm^{-1} . Second is a sharp peak at 1625 cm^{-1} ; the third distinct feature is a broad peak around 1100 cm^{-1} . The assignment of water and/or OH peaks in the IR spectra is consistent with findings by Demourgues *et al.* in a recent study of $\text{Ti}_{0.75}(\text{OH})_{1.5}\text{F}_{1.5}$. [70] These features are absent in the TiOF_2 spectrum, indicating that this material is free of hydroxyl groups.

3.3.3 Variable Temperature PXRD

Unit cell volumes per formula unit (V/Z) were extracted from sequential Rietveld fits to the powder diffraction data and plotted with respect to temperature, as seen in Figures 20 and 21. During the sequential analysis of the diffraction data, a rhombohedral ($R\bar{3}c$) model was used for all TiOF_2 diffraction patterns and the cubic ($Pm\bar{3}m$) structural model was used for all $\text{Ti}_{1-x}(\text{O}/\text{OH}/\text{F})_3$ diffraction patterns during the first heating cycle. The rhombohedral ($R\bar{3}c$) model was employed during analysis of the $\text{Ti}_{1-x}(\text{O}/\text{OH}/\text{F})_3$ diffraction patterns for all subsequent heat cycles. The volumetric coefficient of thermal expansion (CTE), α_v , was

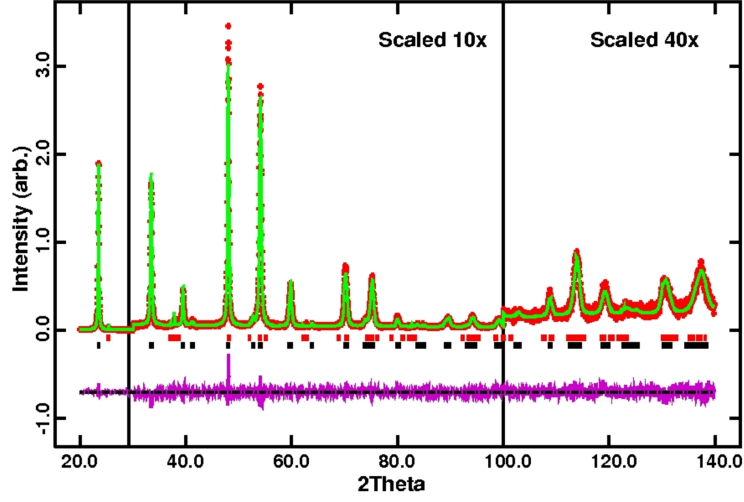


Figure 16: Rietveld fit of the rhombohedral $R\bar{3}c$ model to lab X-ray data for TiOF_2 . The red crosses are the data points, the green line is the fit to the data, and the purple line is the difference curve. The range 30 to 100° 2 Θ was multiplied by 10, and the range 100 to 140° 2 Θ was multiplied by 40 to better show fit quality at higher angles. The top set of reflection markers corresponds to anatase TiO_2 , and the lower set of reflection markers corresponds to rhombohedral TiOF_2 .

Table 5: Crystallographic data from the Rietveld analysis of powder diffraction data for TiOF_2 collected on a Scintag X1 diffractometer at room temperature.

Space group	$R\bar{3}c$, No. 167, Primitive
Unit cell	$a = 5.3734(2) \text{ \AA}$ $\alpha = 59.732(2)^\circ$
Atomic displacement parameters	Ti $U_{iso} = 0.0204(3) \text{ \AA}^2$ O,F $U_{11}=U_{22} = 0.023(1) \text{ \AA}^2$ O,F $U_{33} = 0.022(2) \text{ \AA}^2$ O,F $U_{12} = -0.022(1) \text{ \AA}^2$ O,F $U_{13}=U_{23} = -0.053(8) \text{ \AA}^2$
Atom coordinates	Ti (0, 0, 0), occ. = 1 O $[-0.2117(3), 0.7117(3), 0.25]$, occ. = $\frac{1}{3}$ F $[-0.2117(3), 0.7117(3), 0.25]$, occ. = $\frac{2}{3}$
Rietveld statistics	$\chi^2 = 2.102$, $R_F^2 = 0.0570$

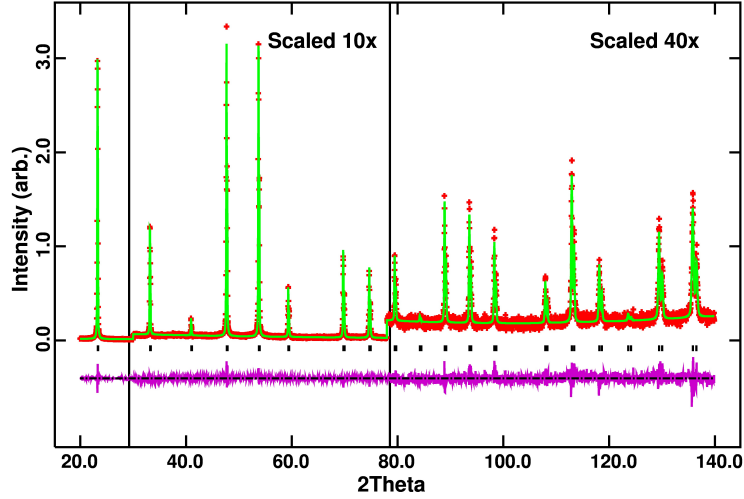


Figure 17: Rietveld fit of the cubic $Pm\bar{3}m$ model to laboratory X-ray data for $\text{Ti}_{1-x}(\text{O}/\text{OH}/\text{F})_3$. The red crosses are the data points, the green line is the fit to the data, and the purple line is a difference curve. The range $30\text{--}78^\circ$ 2Θ was multiplied by 10, and the range $78\text{--}140^\circ$ 2Θ was multiplied by 40 to better show fit quality at higher angles.

Table 6: Crystallographic data from the Rietveld analysis of powder diffraction data collected for $\text{Ti}_{1-x}(\text{O}/\text{OH}/\text{F})_3$ collected on a Scintag X1 diffractometer at room temperature.

Space group	$Pm\bar{3}m$, No. 221
Unit cell	$a = 3.80929(2)\text{\AA}$
Atomic displacement parameters	Ti $U_{iso} = 0.0218(3)\text{\AA}^2$
	O,F $U_{11} = 0.015(1)\text{\AA}^2$
	O,F $U_{22} = U_{33} = 0.0592(9)\text{\AA}^2$
Ti site occupancy	0.788(4)
Rietveld statistics	$\chi^2 = 2.315$
	$R_F^2 = 0.0685$

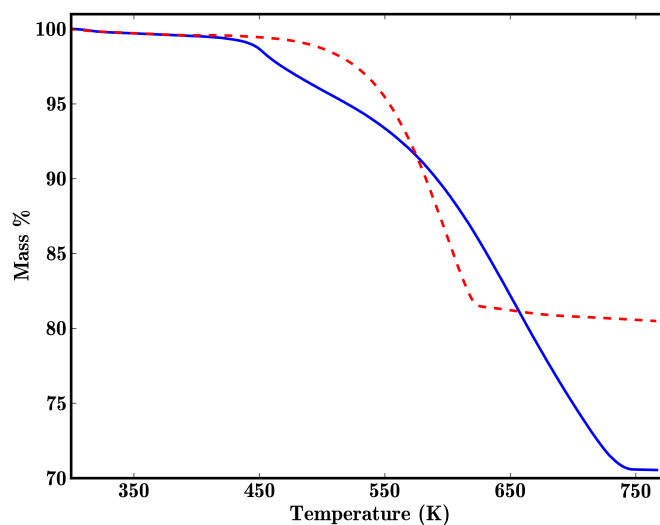


Figure 18: Weight loss on heating. The solid curve is for $\text{Ti}_{1-x}(\text{O}/\text{OH}/\text{F})_3$ and indicates a 29.5% weight loss up to 750 K. The dashed line is for TiOF_2 and indicates a 19.5% weight loss up to 750 K.

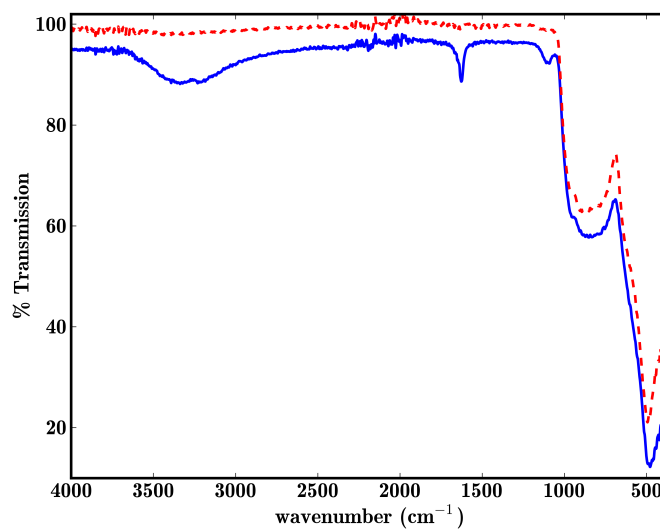


Figure 19: IR spectra collected for $\text{Ti}_{1-x}(\text{O}/\text{OH}/\text{F})_3$ (solid blue line) and TiOF_2 (dashed red line).

derived from a smoothing spline fit through the available data. Both samples exhibit positive thermal expansion over the temperature range examined. Titanium hydroxyoxyfluoride initially undergoes a change at high temperature that alters the thermal expansion behavior on repeated temperature cycles (Figure 20). After this 'change', the material behaves consistently upon repeated temperature cycles; volumetric coefficients of thermal expansion at several temperatures are presented in Table 7. Following the change at high temperature, $\text{Ti}_{1-x}(\text{O}/\text{OH}/\text{F})_3$ adopts a rhombohedral structure at low temperatures and undergoes an apparent second order phase transition to the cubic ReO_3 -structure type at elevated temperatures. As illustrated by a stack plot of the high temperature diffraction data from the wire-wound furnace experiments in Figure 22, no further temperature induced phase transitions are observed before decomposition into TiO_2 .

Table 7: Selected volumetric coefficients of thermal expansion for TiOF_2 and $\text{Ti}_x(\text{O}/\text{OH}/\text{F})_3$ during the first and second heat cycles

Temperature	TiOF_2	$\text{Ti}_{1-x}(\text{O}/\text{OH}/\text{F})_3$ (1 st heating)	$\text{Ti}_{1-x}(\text{O}/\text{OH}/\text{F})_3$ (2 nd heating)
130 K	47 ppm·K ⁻¹	27 ppm·K ⁻¹	61 ppm·K ⁻¹
300 K	165 ppm·K ⁻¹	31 ppm·K ⁻¹	72 ppm·K ⁻¹
490 K	15 ppm·K ⁻¹	10 ppm·K ⁻¹	23 ppm·K ⁻¹

TiOF_2 is rhombohedral ($R\bar{3}c$) at room temperature and undergoes a temperature induced phase transition to cubic ($Pm\bar{3}m$) symmetry at higher temperatures. A stack plot of the high temperature diffraction data from the wire-wound furnace experiments, Figure 23, shows that TiOF_2 does not undergo any further temperature-induced phase transitions before decomposition into TiO_2 at ≈ 650 K. The decomposition of $\text{Ti}_{1-x}(\text{O}/\text{OH}/\text{F})_3$ into anatase TiO_2 occurs at ≈ 600 K, approximately 50 degrees lower than that observed for TiOF_2 .

To estimate the phase transition temperature in TiOF_2 , a pseudo-Voigt function was fit to the cubic (2 2 2) Bragg reflection; this Bragg reflection splits during the cubic \rightarrow rhombohedral phase transition ((2 2 2) \rightarrow (4 4 4), (4 0 0)). As seen in Figure 24, the FWHM of this reflection was plotted with respect to temperature, and peak broadening begins to occur at ≈ 400 K. To provide a second estimate of the phase transition temperature, the integrated intensity of the background and rhombohedral (2 1 0) Bragg reflection (not

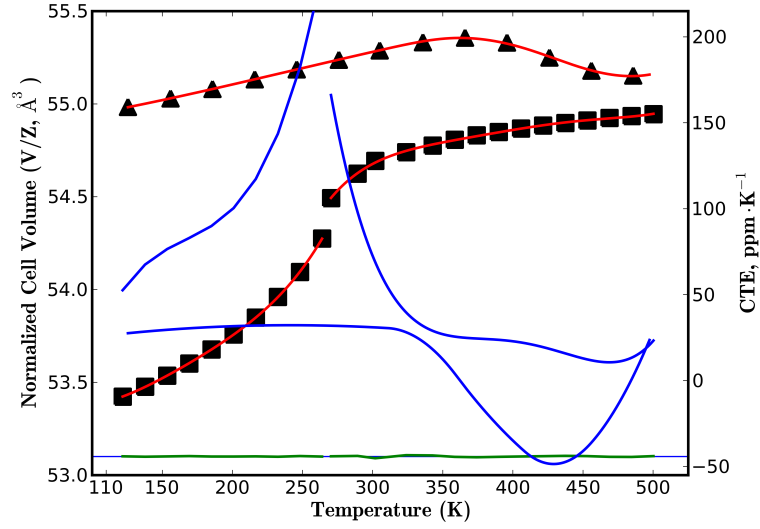


Figure 20: Unit cell volume per formula unit (V/Z , Z = number of formula units in unit cell) plotted with respect to temperature (black '■') for $\text{Ti}_{1-x}(\text{O}/\text{OH}/\text{F})_3$ (Every 5th data point plotted for clarity). The solid red lines are smoothing spline fits through the data (separate splines for low and high temperature range), the blue line is the volumetric coefficient of thermal expansion derived from the spline fit, and the green line at the bottom is a difference curve between the spline fit and the data. The '▼' are data points from the first temperature cycle, which resulted in an irreversible change in the material (Every 5th data point plotted for clarity).

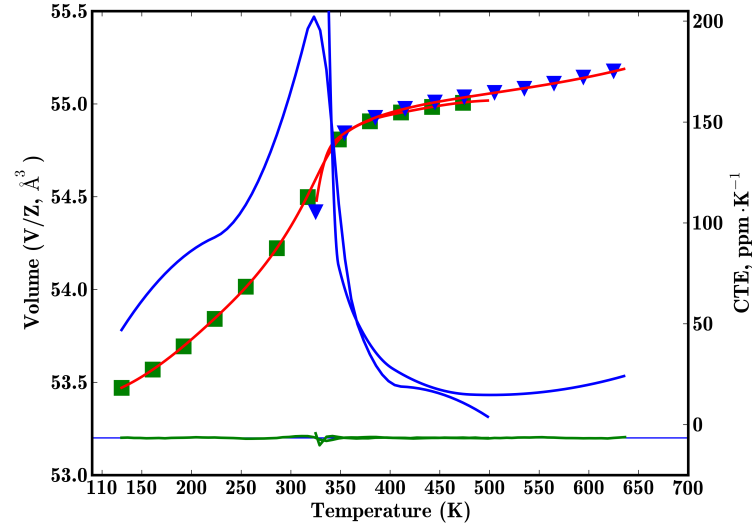


Figure 21: Unit cell volume per formula unit (V/Z) plotted with respect to temperature for TiOF_2 . The green squares are data from the cryostream experiments, and the blue triangles are from the high temperature wire wound furnace. The solid red lines are smoothing spline fits through the data. The blue lines are volumetric CTEs calculated from the spline fit, and the green line is a difference curve between the spline fits and the data.

present in the cubic diffraction patterns) was compared to the integrated intensity of the background ± 1 degree 2θ either side of the peak. As seen in Figure 25, the integrated intensity of the (2 1 0) reflection approaches that of the integrated background intensity at ≈ 425 K.

The atomic displacement factors were refined during the Rietveld analysis of the variable temperature data. These factors were plotted with respect to temperature (Figure 26). In the cubic phase, the site symmetry for Ti constrains the displacement factor to be isotropic; in the rhombohedral phase the Ti atomic displacement factor consists of two components: U_{11} and $U_{22}=U_{33}$. For the cubic phase, the atomic displacement factor for the anions (O/F) is comprised of two components, $U_{11} = U_{22}$ which are transverse to the M-X-M linkage, and U_{33} .

3.3.4 Variable Pressure PXRD

Diffraction patterns were analyzed using the Rietveld method as implemented in GSAS with the EXPGUI interface. Titanium hydroxyoxyfluoride undergoes a phase transition from cubic ($Pm\bar{3}m$) to rhombohedral ($R\bar{3}c$) symmetry between ≈ 0.5 -1 GPa, as evidenced by the appearance of a new Bragg reflection ($d \approx 2.29\text{\AA}$) and peak broadening at high angles (Figure 27). As shown in Figure 28, titanium oxyfluoride remains rhombohedral ($R\bar{3}c$) throughout the pressure range examined. During the analyses, the background was modeled using an interpolation function. The unit cell constants, anion positions within the unit cell (for the rhombohedral phase), atomic displacement parameters, and three profile terms were refined. As the refined parameter values were very sensitive to the choice of background used during Rietveld analysis, the same type of background was interpolated for each diffraction pattern.

The primitive rhombohedral unit cell angle, α , was extracted from the Rietveld analysis results and plotted with respect to pressure (Figure 29). For both samples, the rhombohedral cell angle steadily decreases under pressure. However, titanium hydroxyoxyfluoride appears to have greater sensitivity to applied pressure. As shown in Figure 30, the apparent Ti-X-Ti bond angle in the rhombohedral cells for both materials behaves similarly

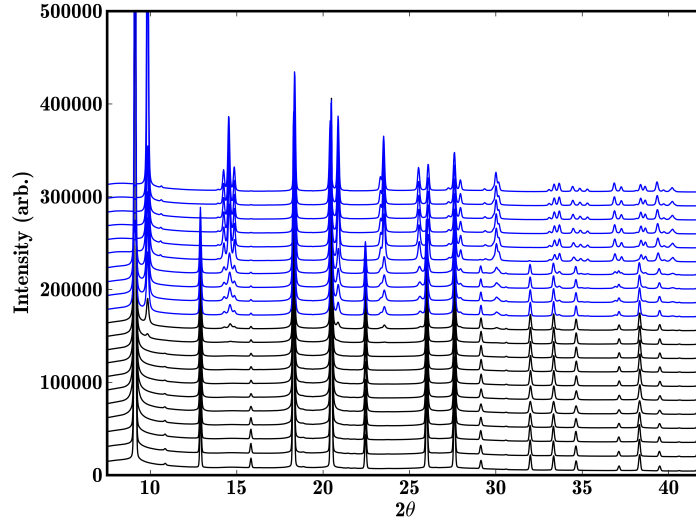


Figure 22: The high temperature powder diffraction data for $\text{Ti}_x(\text{O/OH/F})_3$. Decomposition of $\text{Ti}_{1-x}(\text{O/OH/F})_3$ (black) to TiO_2 (anatase, blue) is observed at temperatures above ≈ 600 K. The first diffraction pattern was recorded at 306 K; the temperature increases ≈ 30 K between each plotted diffraction pattern to a max temperature of 897 K.

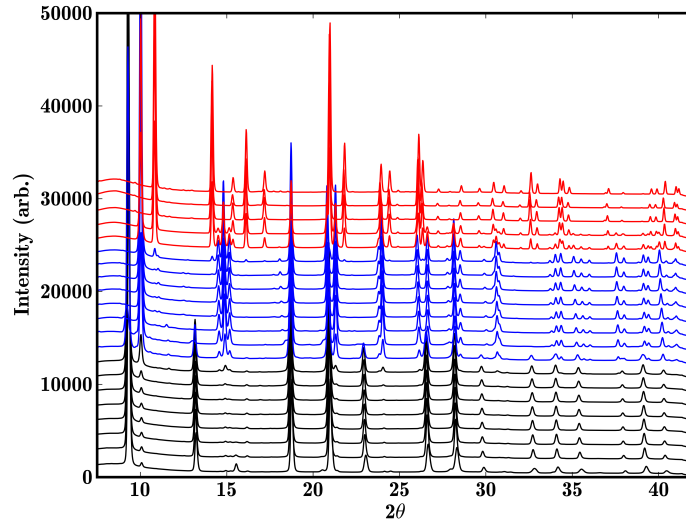


Figure 23: The high temperature powder diffraction data for TiOF_2 . The decomposition of TiOF_2 (black) to anatase TiO_2 (blue) is observed at temperatures above ≈ 650 K. At temperatures above ≈ 1050 K anatase begins to transform into rutile TiO_2 (red diffraction patterns). The first diffraction pattern was recorded at 326 K; the temperature increase ≈ 42 K between each plotted diffraction pattern to a max temperature of 1219 K.

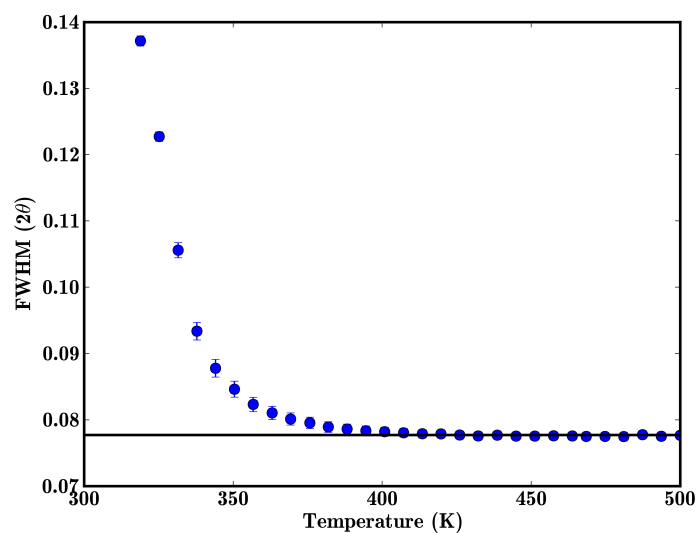


Figure 24: Full width at half maximum of the cubic (2 2 2) reflection plotted with respect to temperature for TiOF_2 .

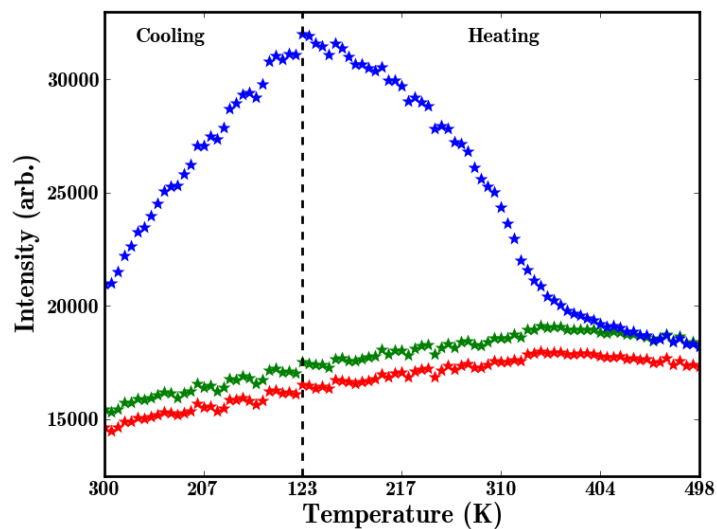


Figure 25: Integrated intensity of the rhombohedral (2 1 0) reflection plus background (blue *) and the integrated intensity of the background to the left (green *) and right (red *) of this reflection for TiOF_2 .

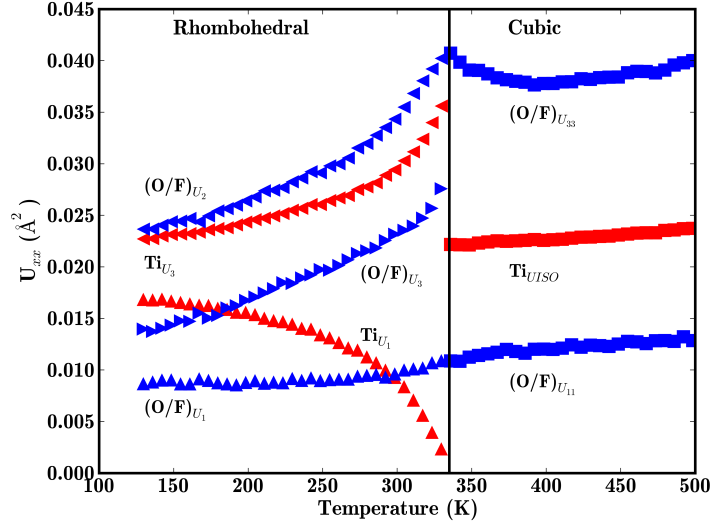


Figure 26: Atomic displacement parameters plotted with respect to temperature for TiOF_2 . For the rhombohedral phase, the principle components of the atomic displacement tensors are plotted.

under applied pressure. The extracted structural information is provided in Supplementary Information.

3^{rd} and 4^{th} order Birch-Murnaghan equations of state (EOS) were fit to the rhombohedral TiOF_2 cell volume–pressure data. Both equations of state fit the data well, with the 4^{th} -order resulting in a slightly better fit (Figures 31a and 31b). The results from both fits are summarized in Table 8. In order to compare the impacts of pressure on the two materials, bulk moduli were also calculated from the lower (1.09–1.34 GPa) and upper (5.66–6.12 GPa) limits of the pressure regions examined and found to be 23.55 and 61.52 GPa, respectively.

An attempt was made to fit a Birch-Murnaghan equation of state to the rhombohedral cell volume–pressure values for the titanium hydroxyoxyfluoride material. However, a ‘decent’ fit was only possible by utilizing a 3^{rd} -order equation of state and keeping K_p fixed at an unreasonably high value of 75 (compared to $K_p=4$ that is observed for most materials, Figure 31c). The calculated bulk moduli for the lower (1.05–1.36 GPa) and upper bounds (5.78–6.49 GPa) of the pressure region were 16.84 and 59.5 GPa, respectively.

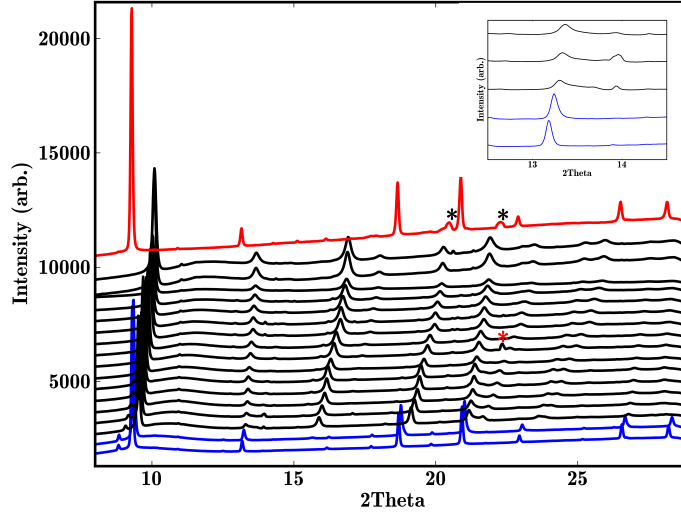


Figure 27: Integrated powder diffraction patterns for titanium hydroxyoxyfluoride. The pressure increases from 0 to ≈ 7 GPa starting at the bottom, the pressures are listed in Table 12 in Supplemental Information. The bottom two diffraction patterns, colored blue, correspond to the cubic ReO_3 structure type. The top diffraction pattern (red) was collected after the diamond anvil cell had been fully decompressed. The inset shows the emergence of a new Bragg reflection arising from the cubic to rhombohedral phase transition.

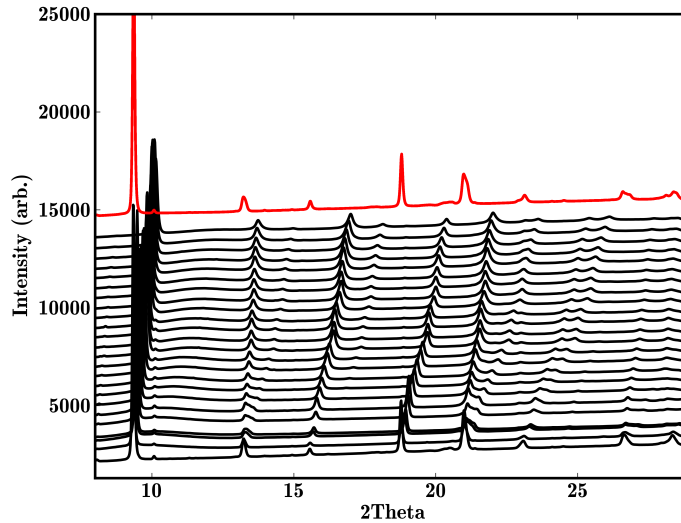


Figure 28: Integrated powder diffraction patterns for TiOF_2 . The pressure increases from 0 to ≈ 8.9 GPa starting at the bottom. The pressures shown are listed in Table 11 in Supplemental Information. The top diffraction pattern, represented as a red line, was collected after the diamond anvil cell had been fully decompressed.

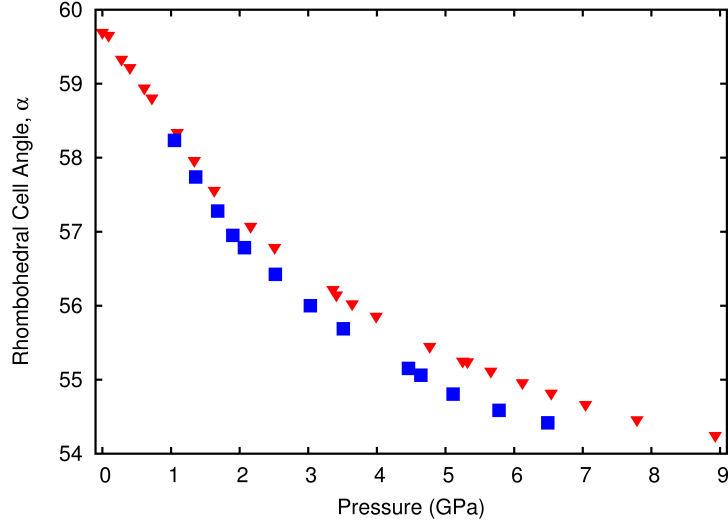


Figure 29: The primitive rhombohedral unit cell angle, α , plotted with respect to pressure at 298 K. TiOF_2 is represented by the triangles, ' \blacktriangledown ', and $\text{Ti}_{1-x}(\text{O/OH/F})_3$ by the squares, ' \blacksquare '. The error in α is smaller than the symbol size.

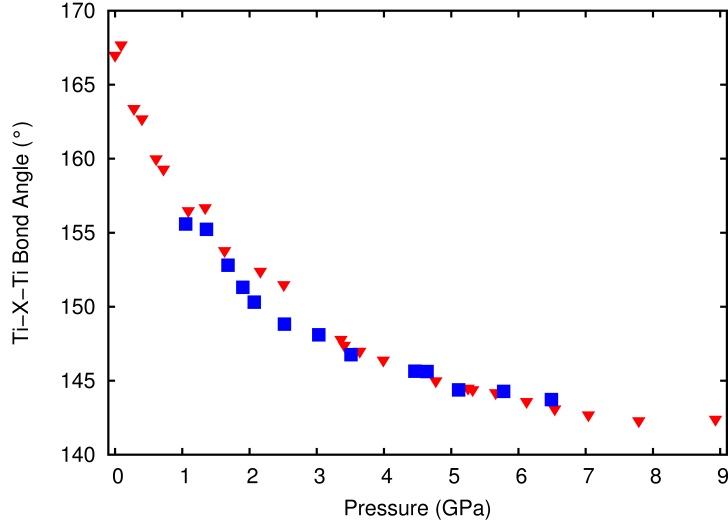


Figure 30: The Ti-X-Ti ($X=\text{O}, \text{F}, \text{OH}$) bond angle plotted with respect to pressure at 298 K. $\text{Ti}_{1-x}(\text{O/OH/F})_3$ is represented by the squares, ' \blacksquare ', and TiOF_2 by the triangles, ' \blacktriangledown '. The error in the bond angle is smaller than the symbol size.

Table 8: Birch-Murnaghan equation of state fit parameters for TiOF_2 and $\text{Ti}_{1-x}(\text{O/OH/F})_3$. *Variables that were kept constant during the equation of state fit.

Material	V_0/Z (\AA^3)	K_0 (GPa)	K_p	K_{pp}	Order of EoS	R_w
TiOF_2	54.4(4)	14.6(4)	4.5(7)	3.2(3)	4 th	0.9908%
TiOF_2	53.6(3)	23.1(9)	4*	-0.16862*	3 rd	8.5814%
$\text{Ti}_{1-x}(\text{O/OH/F})_3$	57.7(4)	1.21(8)	75*	N/A	3 rd	2.7951%

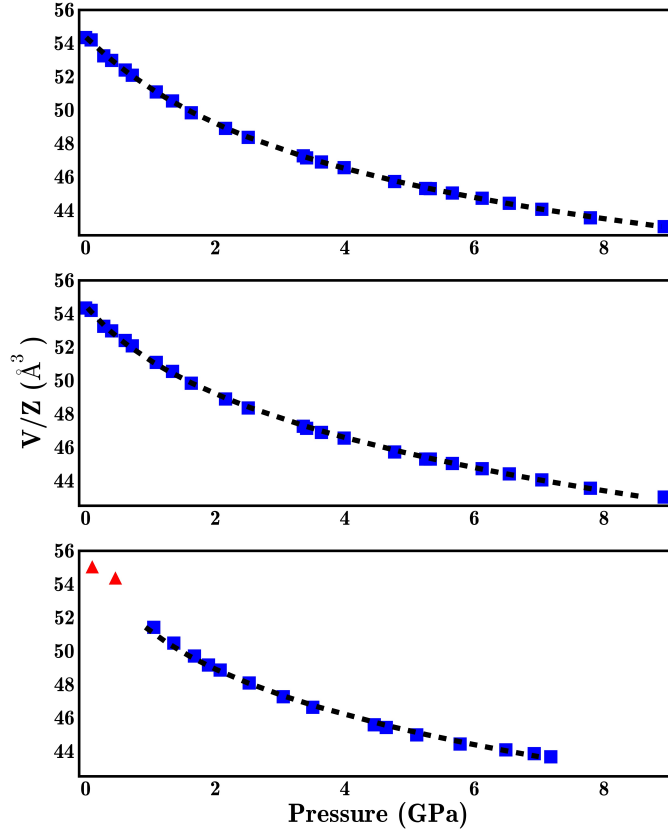


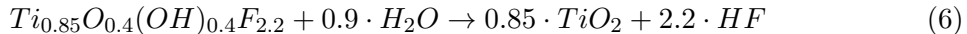
Figure 31: (a) 4th-order Birch-Murnghan equation of state fit to TiOF_2 unit cell volume versus pressure; (b) 3rd-order Birch-Murnghan equation of state fit to TiOF_2 unit cell versus pressure; (c) 3rd-order Birch-Murnghan equation of state (K_p fixed at 75) fit to $\text{Ti}_{1-x}(\text{O}/\text{OH}/\text{F})_3$ unit cell versus pressure.

3.4 Discussion

Titanium oxyfluoride that had been prepared from the direct reaction of TiO_2 with TiF_4 is free of hydroxyl defects and Ti vacancies, but the material does not adopt the cubic ReO_3 structure. Under ambient conditions, this material adopts a rhombohedral structure with ReO_3 -type connectivity. Shian *et al.* reported similar findings in their synthesis of TiOF_2 from TiF_4 vapor and SiO_2 . [69]

The material prepared using the previously reported synthesis (digestion of TiO_2 in aqueous HF) does adopt the cubic ReO_3 structure type but does not have the 1:1:2 stoichiometry implied by the formula TiOF_2 . While there has been speculation in the literature concerning the presence of hydroxyl groups in this material, they have not been properly quantified until now. The measured density of this material was much lower than that of the material produced from the direct reaction synthesis due to the presence of Ti vacancies, an observation that is also supported from the Rietveld analysis of the power diffraction data; refinement of the Ti site occupancy resulted in a substantially improved fit. Coupling the fluoride content with the density measurements, the approximate stoichiometry of the material is $\text{Ti}_{0.85}\text{O}_{0.4}(\text{OH})_{0.4}\text{F}_{2.2}$. The presence of hydroxyl groups in this material is confirmed by IR spectra.

The suggested approximate stoichiometry of $\text{Ti}_{0.85}\text{O}_{0.4}(\text{OH})_{0.4}\text{F}_{2.2}$ is further supported by the TGA measurements. The end product of the decomposition was confirmed to be TiO_2 , with a measured weight loss of $\approx 30\%$. One possible decomposition route to TiO_2 is through pyrohydrolysis:



Such a decomposition would result in a weight loss of 29.1%, which is consistent with the weight loss measured experimentally. As no special precautions were taken to maintain an anhydrous environment during analysis, coupled with evidence of HF liberation through significant fluoride etching of the fused quartz furnace surrounding, it is likely that water was present during the TGA measurements.

The averaged measured fluoride content in TiOF_2 is 42.8%, which is higher than that

expected (37.3%). It is likely that the measured fluoride content in these materials is in error, as the density measurements and thermogravimetric analysis for TiOF_2 are consistent with the material being TiOF_2 . While an excess of TiF_4 was used during the synthesis of TiOF_2 ; residual TiF_4 would hydrolyze in air and should be evident in the IR spectra, however, no such indication was observed. This suggests that the actual fluoride content in $\text{Ti}_{1-x}(\text{O}/\text{OH}/\text{F})_3$ may be lower than estimated from the analysis, which would be offset by an increase in the hydroxyl content.

During the course of this study, multiple titanium hydroxyoxyfluoride samples were synthesized from the digestion of TiO_2 in HF. Diffraction patterns collected for these samples all indicate that they adopted the cubic ReO_3 structure type; however, density measurements of the samples varied from $\approx 2.7\text{--}2.95\text{ g}\cdot\text{cm}^{-3}$. All IR spectra collected of samples prepared using this method indicated that OH groups were present, suggesting that the amount of Ti vacancies and the O/OH/F ratio in this material is extremely sensitive to the reaction conditions; it was not possible to consistently synthesize materials with the same amount of Ti vacancies. In a recent study on zinc hydroxyfluorides, Serier *et al.* reported that during the synthesis of $\text{Zn}(\text{OH})_{2-x}\text{F}_x$, the amount of fluorine in the final product was to some extent dependent upon experimental conditions.[71]

While several other materials with the same structural connectivity display interesting (NTE and 'zero') thermal expansion behavior, both TiOF_2 and $\text{Ti}_{0.85}\text{O}_{0.4}(\text{OH})_{0.4}\text{F}_{2.2}$ exhibit positive thermal expansion in the temperature range examined, between 120 K through decomposition into TiO_2 . The initial decrease in unit cell volume observed during the first heating cycle of the variable temperature diffraction experiments of $\text{Ti}_{1-x}(\text{O}/\text{OH}/\text{F})_3$ arises from a composition change due to pyrohydrolysis. The thermal expansion properties of the resulting material are similar to those of TiOF_2 , and the resulting material adopts a rhombohedrally distorted ReO_3 structure at room temperature. However, TiOF_2 is not formed by this pyrohydrolysis; while similar, the thermal expansion characteristics of the resulting material and TiOF_2 differ, and as evidenced in Figures 20 and 21, the maximum thermal expansion for TiOF_2 occurs at $\approx 330\text{ K}$ whereas the maximum for the new material occurs at $\approx 260\text{ K}$. The temperature-induced phase transition from rhombohedral \rightarrow cubic symmetry

for TiOF_2 also occurs at a higher temperature than that observed for $\text{Ti}_{0.85}\text{O}_{0.4}(\text{OH})_{0.4}\text{F}_{2.2}$ after heating to 500 K.

Shian *et al.* examined the phase transition from rhombohedral to cubic symmetry in TiOF_2 prepared by the reaction of TiF_4 gas with silica microspheres.[69] In the course of their variable temperature powder diffraction studies, there was no evidence of a rhombohedral phase at temperatures greater than 368 K; through the course of DSC analyses the phase transition was estimated to occur between 333-338 K.[69] Variable temperature diffraction data collected for TiOF_2 prepared from the direct reaction of TiO_2 and TiF_4 indicate that, for the material prepared using this route, the rhombohedral to cubic phase transition is not complete until ≈ 400 K (Figures 24 and 25).

Titanium trifluoride, TiF_3 , also adopts a rhombohedrally distorted ReO_3 -type structure under ambient conditions; at temperatures above ≈ 380 K a phase transition to the cubic ReO_3 -type structure is observed.[72] This transition occurs at a slightly lower temperature than that estimated for TiOF_2 . Both TiOF_2 and TiF_3 exhibit drastic changes in thermal expansion behavior during the phase transition; this is in stark contrast to behavior observed for the perovskites SrZrO_3 and LaAlO_3 , where the rate of thermal expansion remains almost constant throughout the transition.[72, 73, 74] Much like TiF_3 , the only temperature induced phase transition observed for TiOF_2 is that from rhombohedral to cubic symmetry.

Much like TiOF_2 , tantalum oxyfluoride, TaO_2F , is also an anion disordered oxyfluoride. Under ambient conditions, TaO_2F adopts the cubic ReO_3 structure type, which is thermally stable until decomposition into Ta_2O_5 at temperatures above 773 K.[34] Tao and Sleight examined the thermal expansion properties of this material, and they reported that the thermal expansion was so low that they could not be certain whether it was positive or negative.[35] Large atomic displacement parameters (ADPs) were observed for Ta and the anion (O/F) transverse component; the large values for the ADPs persisted to low temperatures indicating the presence of static disorder in this structure. This observation led the authors to propose that there may be non-linear Ta-(O/F)-Ta links in this material; if NTE is expected to arise through rocking of rigid unit modes, it would be optimized if the Ta-(O/F)-Ta linkages were at a 180° angle.[35] As evidenced by the low temperature

ADPs for TiOF_2 (Figure 26), there is also a large amount of static disorder in TiOF_2 .

There is not a temperature-induced phase transition in TaO_2F ; the lack of a phase transition, coupled with the potential for different amounts of static disorder in these two materials, may account for their differences in thermal expansion behavior. The CTE for the rhombohedral phase of TiOF_2 is higher than that of the cubic phase; during heating the rhombohedral phase expands as it unfolds into the cubic phase. TiOF_2 also has a greater F:O ratio than TaO_2F ; however, X-ray diffraction alone is not sufficient to quantify how this difference impacts thermal expansion properties. An analysis of the local structures of TiOF_2 and TaO_2F , presented in Chapter 5, is necessary to formulate an understanding of how local structural disorder impacts thermal expansion properties of these materials.

The role of static disorder on the thermal expansion properties of ReO_3 has recently been studied in detail. Analysis of the atomic displacement parameters (ADPs) indicated that there was static disorder of the oxygen atoms in ReO_3 , transverse to the Re–O–Re bonds, that is dependent upon sample preparation and quality.[24] In a study examining the lattice dynamics of ReO_3 , the $M3$ phonon mode, which involves rotation of the ReO_6 octahedra arising from the transverse thermal motion of the bridging oxygen atoms, was implicated as contributing to NTE in this material.[22] As this mode is the primary contributor to NTE at low temperatures, static displacements of the oxygen atoms transverse to the Re–O–Re bond would diminish NTE behavior.[24]

During the high pressure studies, the structure of TiOF_2 remained rhombohedral over the entire pressure range examined. The calculated zero pressure bulk modulus (K_0) for TiOF_2 , as determined from the 4th order Birch-Murnaghan equation of state, is quite low, 14.6(4) GPa. In a high pressure powder diffraction study of TaO_2F , Cetinkol *et al.* reported an average bulk modulus of 60(2) GPa for the high pressure rhombohedral phase between 4–8 GPa (as it was not possible to fit an equation of state to the available data), which is similar to the bulk moduli estimated for the high pressure region for both TiOF_2 ($K=61.5$ GPa between 5.66–6.12 GPa) and $\text{Ti}_{1-x}(\text{O}/\text{OH}/\text{F})_3$ ($K=59.5$ GPa between 5.78–6.49 GPa). Niobium oxyfluoride, NbO_2F , has been reported to have a zero pressure bulk modulus of ≈ 9.6 GPa for the rhombohedral phase, which is a similar value as that observed for

TiOF₂.^[75] The CTE (α_v) of cubic NbO₂F, calculated from 10–300 K, was reported to be 31.2 ppm·K^{−1}; this is higher than the CTE observed for cubic TiOF₂.^[35]

3.5 Conclusions

The two different synthesis methods reported for TiOF₂ resulted in two different materials. The material produced by heating TiO₂ with TiF₄ is in fact TiOF₂, however this material does not adopt the cubic ReO₃ structure under ambient conditions as some reports previously suggested. Using the more commonly used synthesis method, digestion of TiO₂ in HF, did not produce TiOF₂; this synthesis route resulted in a titanium hydroxyoxyfluoride (Ti_{1−x}(O/OH/F)₃) containing Ti vacancies. While both NTE and zero thermal expansion have been observed in some materials with the ReO₃ structure, both TiOF₂ and Ti_{1−x}(O/OH/F)₃ exhibit positive thermal expansion at all temperatures examined.

During the variable temperature diffraction studies, the Ti_{1−x}(O/OH/F)₃ material exhibited a reduction in unit cell volume during the first heating cycle. This reduction occurred during decomposition through pyrohydrolysis, and the resulting material adopted a rhombohedral structure at room temperature and thermal expansion behavior broadly similar to TiOF₂. However, pyrohydrolysis to TiOF₂ was not observed; the thermal expansion rates for the two materials differed and the phase transition from rhombohedral→cubic symmetry occurred at different temperatures.

Large values for the transverse component of the atomic displacement parameters for the anions in TiOF₂ were observed to low temperatures suggesting static disorder of the anions. Such static disorder has been implicated as impeding NTE in ReO₃ and as a possible reason why TaO₂F displays zero thermal expansion as opposed to NTE. The presence of such static disorder, coupled with TiOF₂ adopting a rhombohedral structure at low temperatures, likely contributes to this material displaying positive thermal expansion.

3.6 Supplementary Information

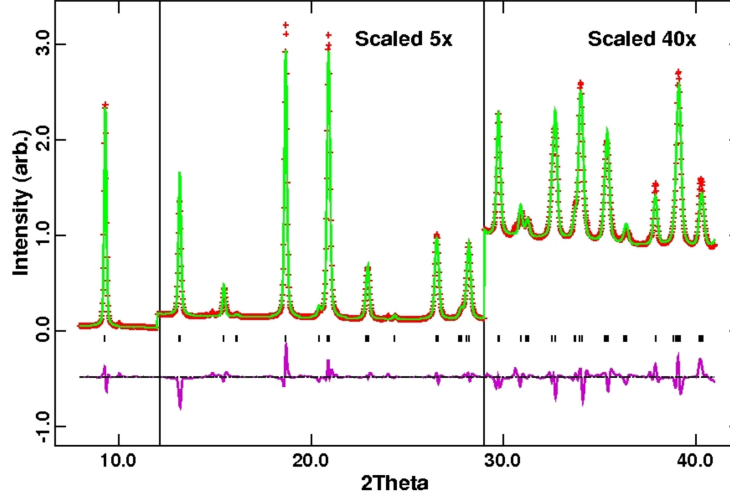


Figure 32: Rietveld fit of TiOF_2 at 298 K. This is a representative fit to the cryostream diffraction data collected using beamline 1-BM-C at the Advanced Photon Source. The fit was used as the starting point for sequential Rietveld analysis of the remaining diffraction data. The red (+) are the data points, the green (-) is the fit, and the purple (-) is the difference curve.

Table 9: Rietveld analysis results for TiOF_2 variable temperature experiment at beamline 1-BM-C of the APS using a cryostream for temperature control. The results are from the analysis of the first pattern in the series, collected at 298 K.

Space group	$R\bar{3}c$, No. 167, Primitive
Wavelength	0.615183 Å
Unit cell	$a = 5.3625(3)$ Å $\alpha = 59.724(2)^\circ$
Atomic displacement parameters	Ti $U_{11=22=33} = 0.0272(5)$ Å ² Ti $U_{12=13=23} = -0.0121(3)$ Å ² Ti $U_1 = 0.0093(2)$ Å ² Ti $U_{2=3} = 0.029(7)$ Å ² O,F $U_{11=22} = 0.026(1)$ Å ² O,F $U_{33} = 0.020(2)$ Å ² O,F $U_{12} = -0.020(1)$ Å ² O,F $U_{13=23} = -0.0040(8)$ Å ² O,F $U_1 = 0.009(1)$ Å ² O,F $U_2 = 0.034(2)$ Å ² O,F $U_3 = 0.023(1)$ Å ²
Atom coordinates	Ti (0, 0, 0), occupancy = 1 O $[-0.2119(4), 0.7119(4), 0.25]$, occupancy = $\frac{1}{3}$ F $[-0.2119(4), 0.7119(4), 0.25]$, occupancy = $\frac{2}{3}$
Rietveld statistics	$\chi^2 = 28.94$, $R_F^2 = 0.0576$

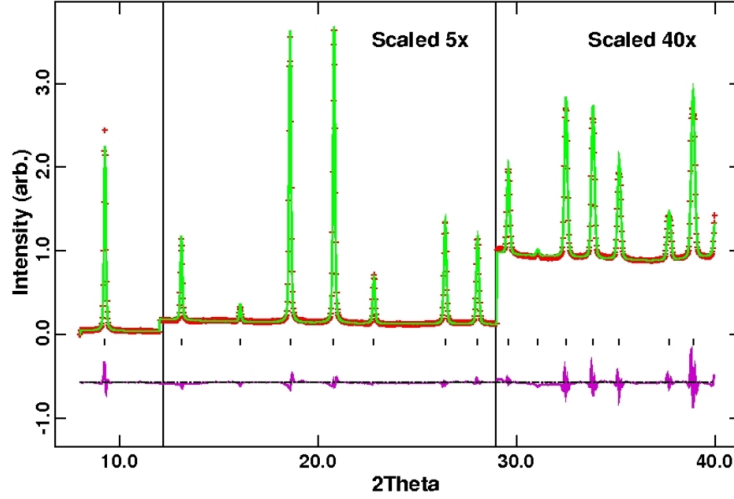


Figure 33: Rietveld analysis of $\text{Ti}_{1-x}(\text{O}/\text{OH}/\text{F})_3$ at 298 K. This is a representative fit to the cryostream diffraction data collected using beamline 1-BM-C at the Advanced Photon Source. The fit was used as the starting point for sequential Rietveld analysis of the remaining diffraction data. The red (+) are the data points, the green (-) the fit, and the purple (-) the difference curve.

Table 10: Rietveld refinement results from the analysis of the 298 K diffraction pattern collected for $\text{Ti}_{1-x}(\text{O}/\text{OH}/\text{F})_3$ at beamline 1-BM-C of the APS.

Space group	$Pm\bar{3}m$, No. 221
Wavelength	0.615183 Å
Unit cell	$a = 3.80629(9)$ Å Vol. = 55.145(4)
Atomic displacement parameters	Ti $U_{iso} = 0.0164(3)$ Å ² O,F $U_{11} = 0.0154(9)$ Å ² O,F $U_{22} = 0.0474(8)$ Å ² O,F $U_{33} = 0.0474(8)$ Å ²
Atom coordinates	Ti (0, 0, 0), occupancy = 0.779(5) O (0.5, 0, 0), occupancy = $\frac{1}{3}$ F (0.5, 0, 0), occupancy = $\frac{2}{3}$
Rietveld statistics	$\chi^2 = 17.65$, $R_F^2 = 0.0375$

Table 11: Rhombohedral lattice parameters, unit cell volume, Ti-X-Ti bond angle, and apparent Ti-X bond length for TiOF₂ as a function of pressure

Pressure (GPa at 298 K)	$a(\text{\AA})$	$\alpha(^{\circ})$	$Vol(\text{\AA}^3)$	Ti-X-Ti ($^{\circ}$)	Ti-X (\AA)
0	5.3685(2)	59.696(2)	108.653(8)	167.0(2)	1.9059(4)
0.09	5.6357(2)	59.655(2)	108.378(6)	167.7(2)	1.9031(3)
0.28	5.3474(3)	59.332(3)	106.479(9)	163.4(2)	1.9011(5)
0.40	5.3429(3)	59.219(4)	105.935(9)	162.7(2)	1.8996(5)
0.61	5.3352(4)	58.944(5)	104.792(9)	160.0(2)	1.9001(7)
0.72	5.3309(5)	58.808(5)	104.21(1)	159.3(2)	1.8989(8)
1.09	5.3156(4)	58.343(7)	102.176(6)	156.5(2)	1.8955(8)
1.34	5.3117(5)	57.965(7)	101.025(9)	156.7(3)	1.8881(9)
1.63	5.3051(5)	57.561(6)	99.654(9)	153.8(2)	1.8904(8)
2.16	5.2925(4)	57.074(5)	97.755(8)	152.4(2)	1.8845(7)
2.51	5.2858(4)	56.789(5)	96.689(7)	151.5(2)	1.8815(6)
3.36	5.2706(4)	56.220(4)	94.471(6)	147.8(2)	1.8846(8)
3.41	5.2695(3)	56.147(4)	94.234(6)	147.4(2)	1.8849(8)
3.64	5.2657(4)	56.027(4)	93.738(6)	147.0(2)	1.8838(8)
3.99	5.2609(3)	55.860(4)	93.077(6)	146.4(2)	1.8826(8)
4.77	5.2482(3)	55.452(4)	91.421(5)	145.0(2)	1.8790(8)
5.25	5.2415(3)	55.252(4)	90.587(3)	144.5(2)	1.8767(8)
5.32	5.2417(3)	55.244(4)	90.580(3)	144.4(1)	1.8770(8)
5.66	5.2371(3)	55.117(4)	90.037(2)	144.2(1)	1.8748(8)
6.12	5.2319(3)	54.961(4)	89.389(3)	143.6(1)	1.8736(8)
6.54	5.2264(3)	54.819(3)	88.768(4)	143.1(1)	1.8722(8)
7.04	5.2195(3)	54.666(3)	88.051(4)	142.7(1)	1.8700(8)
7.79	5.2096(3)	54.460(3)	87.061(3)	142.3(1)	1.8654(8)
8.93	5.1988(3)	54.248(3)	86.017(3)	142.4(1)	1.8582(8)

Table 12: Symmetry, lattice parameters, unit cell volume, Ti-X-Ti bond angle, and apparent Ti-X bond length for Ti_{1-x}(O/OH/F)₃ as a function of pressure

Pressure (GPa)	Symmetry	$a(\text{\AA})$	$\alpha(^{\circ})$	$Vol(\text{\AA}^3)$	Ti-X-Ti ($^{\circ}$)	Ti-X (\AA)
0.10	cubic	3.8040(3)		55.046(1)	180.00(0)	1.90200(2)
0.46	cubic	3.7885(1)		54.374(6)	180.00(0)	1.89423(7)
1.05	rhombohedral	5.3316(8)	58.234(9)	102.83(2)	155.59(33)	1.9029(12)
1.36	rhombohedral	5.3202(7)	57.74(1)	100.96(1)	155.23(23)	1.8931(9)
1.68	rhombohedral	5.3129(6)	57.279(7)	99.40(1)	152.80(29)	1.8930(12)
1.90	rhombohedral	5.3084(7)	56.950(7)	98.33(1)	151.31(28)	1.8927(12)
2.07	rhombohedral	5.3049(5)	56.784(7)	97.727(4)	150.31(28)	1.8934(12)
2.52	rhombohedral	5.2927(7)	56.423(7)	96.17(1)	148.82(27)	1.8905(13)
3.03	rhombohedral	5.2822(9)	56.00(1)	94.56(1)	148.1(4)	1.8839(18)
3.51	rhombohedral	5.2725(7)	55.688(7)	93.27(1)	146.76(27)	1.8824(14)
4.46	rhombohedral	5.2572(8)	55.152(9)	91.161(5)	145.64(29)	1.8748(15)
4.64	rhombohedral	5.2555(8)	55.060(9)	90.846(6)	145.62(30)	1.8729(15)
5.11	rhombohedral	5.2503(8)	54.805(8)	89.961(9)	144.38(27)	1.8738(15)
5.78	rhombohedral	5.2391(9)	54.586(8)	88.85(1)	144.28(28)	1.8672(15)
6.49	rhombohedral	5.2335(9)	54.417(8)	88.16(1)	143.72(27)	1.8657(15)

CHAPTER IV

EFFECT OF PRESSURE ON THE PROPERTIES OF TaO₂F AND ScF₃

4.1 Introduction

Negative thermal expansion (NTE) materials have been the target of recent research efforts, due to fundamental interest in structure–property relationships and because of their possible applications.[4, 12] One such application for NTE materials is in controlled thermal expansion composites; controlling thermal expansion can lead to enhanced dimensional stability and the ability to match expansion between different components.[15] The manufacture and use of composites can subject the materials to stresses that may induce phase transitions or alter the thermal expansion behavior of the materials.

Cubic zirconium tungstate, ZrW₂O₈, is one of the most widely studied NTE materials; it exhibits strong isotropic NTE across a broad temperature range. Holzer *et al.* explored the feasibility of making a metal matrix composite between copper metal and ZrW₂O₈; such a composite should have low thermal expansion and high thermal conductivity, which are desired for applications such as heat sinks for electronic components.[38] However, a phase transition from cubic ZrW₂O₈ to orthorhombic ZrW₂O₈ arising from stresses encountered during processing or from mismatches between the coefficients of thermal expansion (CTEs) for the filler and matrix was observed. This transition does not occur on hydrostatic compression until ≈ 220 MPa; the thermal expansion behavior of the two ZrW₂O₈ phases differs, resulting in a composite with diminished performance.[43, 44]

The pressure dependence of the volumetric coefficient of thermal expansion (α_v) is related to the temperature dependence of the isothermal bulk modulus (K_T) by:[41]

$$\left(\frac{\partial \alpha_v}{\partial p}\right)_T = \frac{1}{K_T^2} \left(\frac{\partial K_T}{\partial T}\right)_p \quad (7)$$

Experimental and theoretical studies of the temperature dependence of the isothermal bulk modulus, $(\frac{\partial K_T}{\partial T})_p$, show that it is typically negative, which implies that the CTE usually decreases upon compression.[42]

The pressure dependence of the CTE for $\text{Zn}(\text{CN})_2$, a negative thermal expansion material, has been examined; the CTE was reported to become more negative upon compression.[76] The average linear CTE for this material decreased from $-17.4(2) \text{ ppm}\cdot\text{K}^{-1}$ to $-19.4(2) \text{ ppm}\cdot\text{K}^{-1}$ upon going from ambient pressure to 0.4 GPa. Cetinkol *et al.* examined the pressure dependence of the CTE for the NTE material $\text{Zr}_2(\text{WO}_4)(\text{PO}_4)_2$; no effect on the CTE was observed from ambient pressure to 0.30 GPa.[77]

There has been little research examining the effects of pressure on the CTE of negative thermal expansion materials. The same structural features that can give rise to NTE, namely flexible open frameworks, can also cause interesting behavior on modest compression. High pressure behaviors, such as phase transitions, can be problematic for applications, necessitating the need for further studies of the effects of pressure on thermal expansion in NTE materials.

TaO_2F , which adopts the cubic ReO_3 structure type, has been reported to be a 'zero' expansion material, and a recent high pressure study reported a phase transition from cubic to rhombohedral symmetry above $\approx 0.7 \text{ GPa}$. [35, 45] ScF_3 also adopts the cubic ReO_3 structure type and was recently reported to exhibit pronounced NTE across a broad temperature range, and a phase transition from cubic to rhombohedral symmetry was observed at $\approx 0.8 \text{ GPa}$. [33] To date, there have been no studies examining the effects of pressure on the CTEs of these two materials.

4.2 *Experimental*

4.2.1 Sample Preparation

Scandium trifluoride was used as supplied by American Elements (99.99% metals basis). TaO_2F had been prepared previously¹ by dissolving Ta_2O_5 (STREM, 99.8% metals basis) in a Pt crucible with concentrated HF (Mallinckrodt, 48%) followed by slow evaporation to dryness. This sample is subsequently referred to as $\text{TaO}_2\text{F-A}$. The remaining powder was transferred to a Teflon container and heated at 453 K for 10 hours. TaO_2F was also prepared using a low temperature solid state reaction between Ta_2O_5 and TaF_5 . The

¹This sample was prepared by Mehmet Cetnikol.

reagents (including a 10% excess of TaF_5 over that required by stoichiometry) were combined in an argon filled glove box using a mortar and pestle. The reaction mixture was sealed inside a nickel tube fitted with stainless steel Swagelok compression fittings to create an air-tight vessel. The mixture was heated at 483 K for 18 hours, and then quenched in water to room temperature. This sample is subsequently referred to as $\text{TaO}_2\text{F-B}$; two different batches of $\text{TaO}_2\text{F-B}$ were prepared, one of X-ray diffraction experiments and a scaled up synthesis for neutron diffraction experiments at HFIR.

4.2.2 High Pressure–Low Temperature Neutron Diffraction

High pressure–low temperature time of flight (TOF) neutron diffraction data were collected² for $\text{TaO}_2\text{F-A}$ on the Special Environment Powder Diffractometer (SPED) at the Intense Pulsed Neutron Source (IPNS), Argonne National Laboratory.[78] Pressure was controlled using a helium gas pressure cell that allowed the application of precisely measured hydrostatic pressure.[40] At room temperature, data were recorded at 0.00, 0.05, 0.10, 0.20, 0.25, 0.30, and 0.40 GPa. At 60 K, diffraction data were recorded at 0.00, 0.20, and 0.30 GPa.

Neutron powder diffraction data were collected for both samples of TaO_2F and for ScF_3 at beamline HB2A of the High Flux Isotope Reactor (HFIR), Oak Ridge National Laboratory. A wavelength of 1.54 Å was selected using a Ge crystal monochromator for the TaO_2F measurements and a wavelength of 1.12 Å was selected for the ScF_3 measurements. The powdered samples were held inside an aluminum bodied helium gas pressure cell that allowed application of precisely measured hydrostatic pressure. Temperature control was provided using a closed-cycle helium refrigerator. Diffraction data for ScF_3 were recorded at 0.007, 0.103, 0.207, and 0.310 GPa at 50, 100, 150, and 280 K. For $\text{TaO}_2\text{F-A}$, diffraction data were recorded at 0.007, 0.103, 0.207, and 0.310 GPa at 40, 80, 120, 160, 200, 240, and 280 K; for $\text{TaO}_2\text{F-B}$, diffraction data were recorded at 0.007, 0.103, 0.207, and 0.310 GPa at 40, 60, 80, 100, 120, 160, 200, 240, and 280 K.

²The HP–LT diffraction data from IPNS for $\text{TaO}_2\text{F-A}$ were collected by Mehmet Cetnikol in 2007.

4.2.3 High Pressure–High Temperature X-ray Diffraction

High pressure–high temperature X-ray diffraction data were collected for TaO₂F-B on beam-line 11-ID-B at the Advanced Photon Source (APS), Argonne National Laboratory. TaO₂F-B was slurried with silicone oil and loaded into a Kapton capillary that was then loaded into a specially designed titanium pressure vessel equipped with an internal collimator to reduce scattering from the pressure vessel.[79] Hydrostatic pressure was applied using a hand-driven syringe pump utilizing silicone oil as the pressure transmitting medium. Temperature control was provided by an aluminum bodied heater block equipped with cartridge heaters that surrounded the Ti pressure vessel. High energy X-rays (58.29 keV) were used to provide adequate penetration of the pressure cell. Diffraction data were recorded on a Perkin Elmer amorphous silicon-based area detector (2048x2048, 200 μ m pixels). Ceria, CeO₂, was used as a calibrant for sample-to-detector distance, detector tilt angle, and beam center. The two-dimensional diffraction images were processed using the program Fit2D.[50] Diffraction data were recorded at ambient, 323, 373, and 423 K at 0.008, 0.04, 0.08, 0.12, 0.16, 0.20, 0.24, and 0.27 GPa. Data were also recorded at 473 and 523 K at 0.008, 0.04, 0.08, 0.12, 0.16, 0.20 and 0.24 GPa.

4.3 Results

4.3.1 TaO₂F

The variable temperature–pressure neutron diffraction patterns collected for TaO₂F at HFIR were analyzed using a combination of the Le Bail and Rietveld methods as implemented in Fullprof.[55] As seen in Figure 34, the diffraction patterns were dominated by scattering from the aluminum pressure cell. A Le Bail fit was utilized to fit the aluminum diffraction peaks, while a Rietveld fit of the cubic $Pm\bar{3}m$ model was made to the TaO₂F diffraction data. The lattice parameters for TaO₂F, scale factor, and a four term Thompson-Cox-Hastings pseudo Voigt profile function were refined. The background was modeled using a 6-term polynomial function; the atomic displacement parameters were fixed at 0.0025 Å², as attempts to refine them resulted in either unrealistic values or caused the Rietveld refinement to fail. The TaO₂F lattice parameters obtained from the Rietveld

analyses are presented in Supplemental Information.

The high pressure–high temperature X-ray diffraction patterns collected for TaO₂F-B at the APS were analyzed using the Rietveld method as implemented in GSAS using the EXPGUI interface.[53, 54] The regions in the diffraction pattern below 8.5° 2 θ were excluded because they were dominated by scattering from the Ti pressure vessel. The cubic $Pm\bar{3}m$ model was used during the analyses of all the diffraction patterns; the lattice parameters for TaO₂F, scale factor, isotropic atomic displacement parameters for Ta and O/F (constrained to have identical values), detector zero correction, and a 4-term pseudo Voigt profile function were refined. The background was modeled using an 8-term shifted Chebyshev function. A representative Rietveld fit to the diffraction data collected at 523 K, 0.24 GPa is shown in Figure 35. The lattice parameters extracted from the Rietveld analyses are presented in Supplemental Information.

The unit cell volumes of TaO₂F-A and TaO₂F-B were extracted from the Rietveld analyses of the variable temperature–variable pressure diffraction data and plotted with respect to temperature at pressure, and with respect to pressure at temperature (Figures 36–41). Straight line fits were used to calculate average volumetric CTEs at pressure, and average bulk moduli at temperature (Table 13). The non-linear behavior of the unit cell volume at low temperature (\approx 40–160 K) and high pressure (0.310 GPa) suggested the presence of a phase transition and prompted a reevaluation of the high pressure–low temperature TOF neutron diffraction data, which are of higher quality because of the pressure cell design and experimental geometry.

The TOF diffraction pattern collected for TaO₂F-A at 60 K, 0.3 GPa shows a Bragg reflection at $d \approx 1.43$ Å that is not accounted for using a cubic ($Pm\bar{3}m$) structural model. The diffraction pattern was reanalyzed using a primitive rhombohedral ($R\bar{3}c$) structural model (Figure 42) that accounts for this Bragg reflection, giving an improvement to the fit quality ($\chi^2=1.394$ vs. 1.756 and $R_p=0.1079$ vs. 0.1217). For comparison purposes, the ambient diffraction pattern for TaO₂F is shown in Figure 43 and the fit of the cubic $Pm\bar{3}m$ model to the 60 K, 0.3 GPa diffraction data is shown in Figure 44. This extra reflection was not observed in the high pressure–low temperature diffraction data from HFIR, which

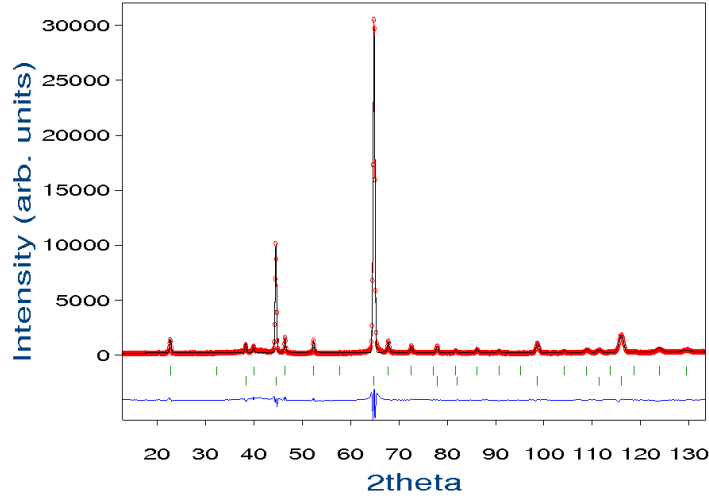


Figure 34: Rietveld fit to the 280 K, 0.007 GPa diffraction pattern collected for TaO₂F-A at HFIR. The top set of reflection markers correspond to cubic ($Pm\bar{3}m$) TaO₂F, the bottom set to FCC Al (sample cell). The red (o) are the data points, the black (–) is the fit to the data, and the blue (–) is the difference curve.

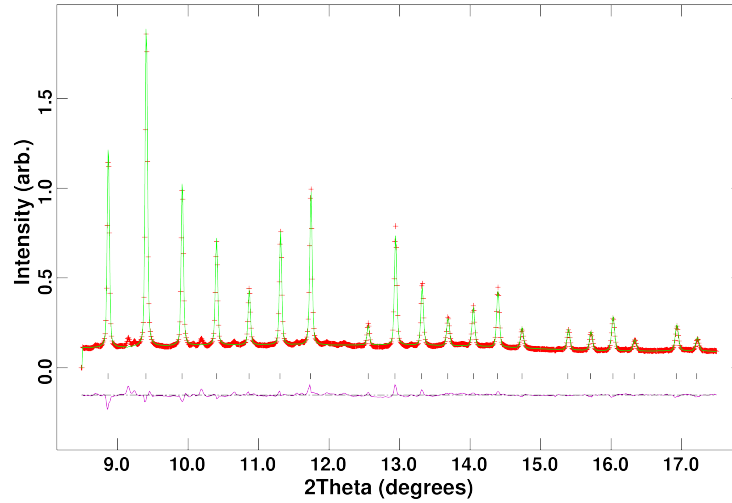


Figure 35: Representative Rietveld fit to the high pressure–high temperature TaO₂F X-ray diffraction data. The observed (red +), calculated (green –), difference curve (purple –), and reflection markers (|) are shown for the diffraction pattern collected at 523 K and 0.24 GPa inside of a titanium pressure cell.

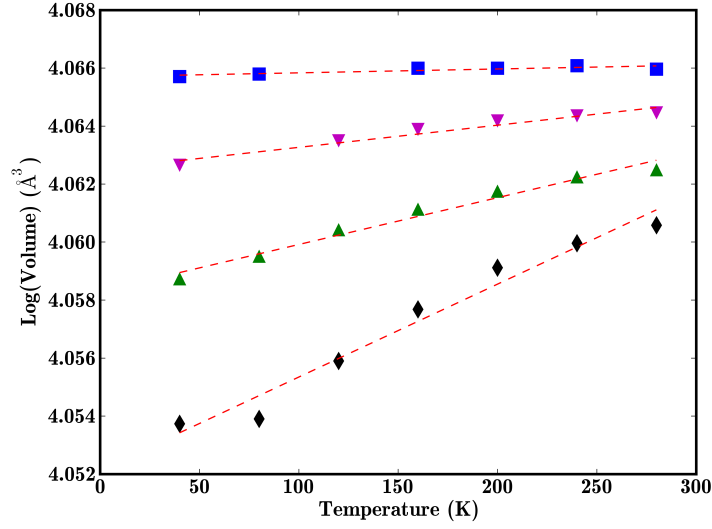


Figure 36: Log of unit cell volume plotted with respect to temperature at 0.007 GPa (blue ■), 0.1 GPa (purple ▽), 0.2 GPa (green △), and 0.3 GPa (black ◇) for TaO₂F-A from experiments at HFIR. The dashed red lines are straight line fits used to estimate average volumetric CTEs.

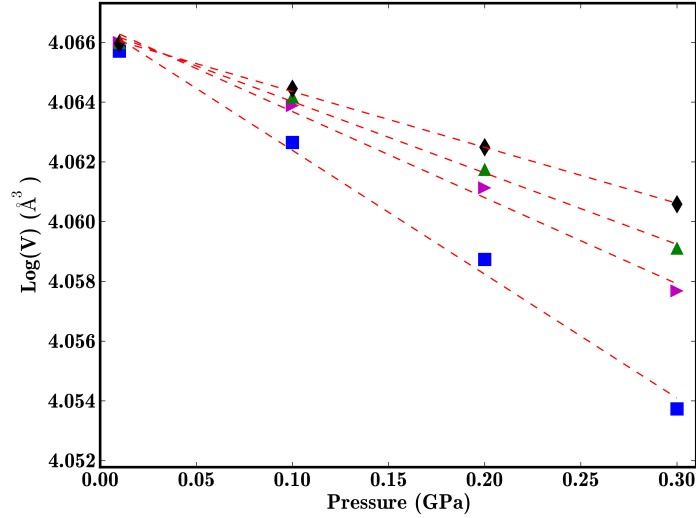


Figure 37: Log of unit cell volume plotted with respect to pressure at 40 K (blue ■), 160 K (purple ▸), 200 K (△), and 280 K (black ◇) for TaO₂F-A from experiments at HFIR. The dashed red lines are linear fits used to estimate the average bulk modulus (K). Data sets from 80, 120, and 240 K were omitted for clarity.

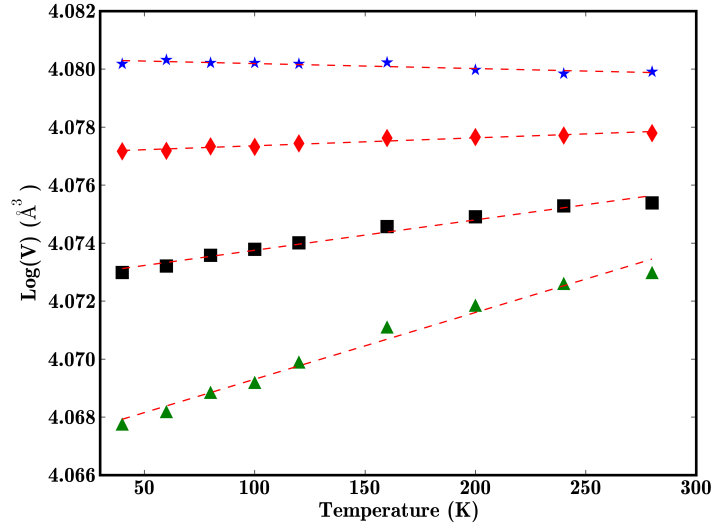


Figure 38: Log of unit cell volume plotted with respect to temperature at 0.007 GPa (blue *), 0.103 GPa (red ◇), 0.207 GPa (black ■), and 0.310 GPa (green △) for TaO₂F-B from experiments at HFIR. The dashed red lines are straight line fits used to estimate the average volumetric CTEs.

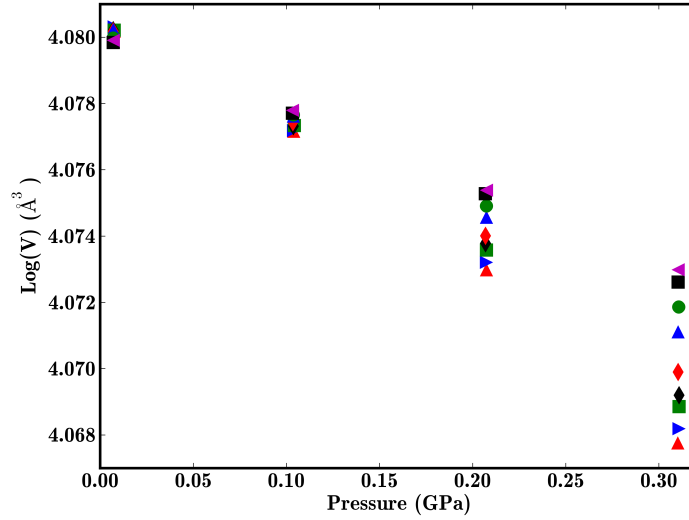


Figure 39: Log of unit cell volume of TaO₂F-B plotted with respect to pressure at 40 K (red △), 60 K (blue ▹), 80 K (green ■), 100 K (black ◇), 120 K (red ◇), 160 K (blue △), 200 K (green ○), 240 K (black ■), and 280 K (purple ◁) from low temperature-high pressure diffraction experiments at HFIR. The straight line fits used to calculate the average bulk modulus are omitted for clarity.

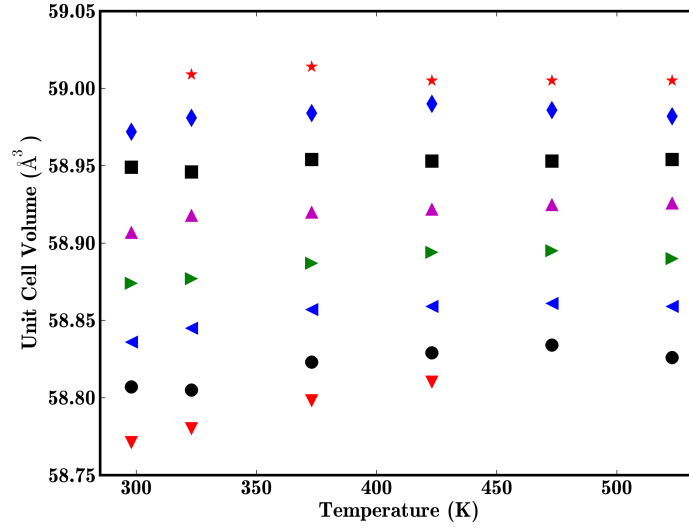


Figure 40: Unit cell volume for TaO₂F-B from APS plotted with respect to temperature at 0.008 GPa (red *), 0.04 GPa (blue ◇), 0.08 GPa (black ■), 0.12 GPa (purple ▽), 0.16 GPa (green ▷), 0.20 GPa (blue ◁), 0.24 GPa (black ○), and 0.27 GPa (red ▿).

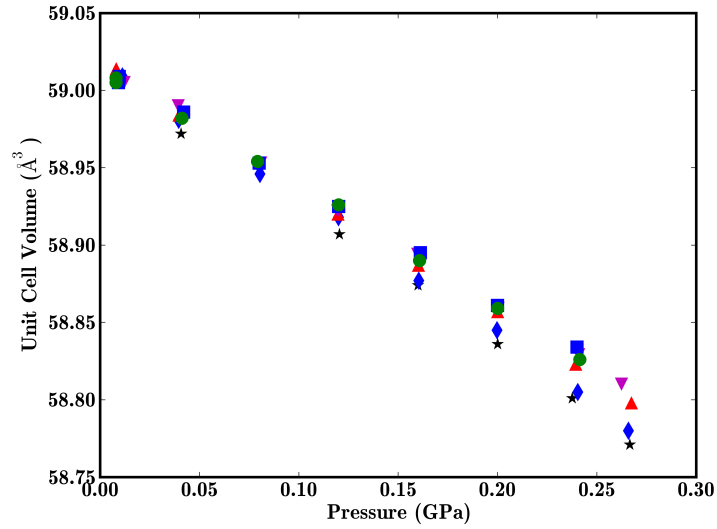


Figure 41: Unit cell volume for TaO₂F-B from APS plotted with respect to pressure at ambient (black *), 323 K (blue ◇), 373 K (red △), 423 K (purple ▽), 473 K (blue ■), and 523 K (green ○). Straight line fits used to calculate the bulk modulus are omitted for clarity.

Table 13: Average volumetric coefficients of thermal expansion (40–280 K) for TaO₂F-A and TaO₂F-B at pressure and average bulk modulus, K , at temperature, calculated from straight line fits through $\ln(V)$ vs T and $\ln(V)$ vs P , respectively.

<i>Pressure (GPa)</i>	TaO ₂ F-A, α_v	TaO ₂ F-B, α_v
0.007	1.4(4) ppm·K ⁻¹	-1.7(4) ppm·K ⁻¹
0.103	7.6(9) ppm·K ⁻¹	2.7(2) ppm·K ⁻¹
0.207	16(1) ppm·K ⁻¹	10.5(6) ppm·K ⁻¹
0.310	32(3) ppm·K ⁻¹	23(1) ppm·K ⁻¹
<i>Temperature (K)</i>	TaO ₂ F-A, K	TaO ₂ F-B, K
40	24(1) GPa	24(2) GPa
60	N/A	25(2) GPa
80	25(4) GPa	27(2) GPa
100	N/A	27(2) GPa
120	31(3) GPa	29(2) GPa
160	35(2) GPa	33(1) GPa
200	42(2) GPa	37(1) GPa
240	47(1) GPa	42(1) GPa
280	53(1) GPa	44(1) GPa

Table 14: Average volumetric coefficients of thermal expansion (298–523 K) for TaO₂F-B at pressure, and average bulk modulus, K , at temperature, calculated from straight line fits to $\ln(V)$ vs. P from Rietveld analyses of the high temperature–high pressure diffraction data collected on beamline 11-ID-B of the APS. Note that this sample of TaO₂F-B was not the same batch of sample used for the low temperature experiments at HFIR.

<i>Pressure (GPa)</i>	α_v , ppm·K ⁻¹
0.008	-0.6(4)
0.040	0.7(5)
0.080	0.5(2)
0.120	1.2(3)
0.160	1.4(5)
0.200	1.7(5)
0.240	1.9(6)
0.270	5.4(4)
<i>Temperature (K)</i>	K , GPa
298	65(2)
323	66(1)
348	68(1)
373	72(1)
398	71(1)
423	75(1)
473	78(1)
523	76(1)

was of lower quality and was dominated by scattering from the sample environment.

4.3.2 ScF₃

The low temperature–high pressure neutron diffraction data collected on beamline HB2A at HFIR for ScF₃ were analyzed using a combination of the Le Bail and Rietveld methods as implemented in Fullprof.[55] As seen with TaO₂F in Figure 34, the recorded diffraction patterns were dominated by scattering from the aluminum bodied pressure cell; a representative fit to the diffraction pattern collected at 0.007 GPa and 280 K for ScF₃ is provided in Supplemental Information. The diffraction peaks from the pressure cell were modeled with a Le Bail fit; the ScF₃ peaks were modeled simultaneously using a Rietveld fit. The 0.310 GPa diffraction patterns recorded at 50 and 100 K, and the diffraction pattern recorded at 0.207 GPa and 50 K were modeled using the rhombohedral $R\bar{3}c$ space group using hexagonal axes; all others were modeled using the cubic $Pm\bar{3}m$ space group. The lattice parameters for ScF₃, scale factor, and a four term Thompson-Cox-Hastings pseudo Voigt profile function were refined. The background was modeled using a 6-term polynomial function; the atomic displacement parameters were fixed at 0.0025 Å² as attempts to refine them resulted in either unrealistic values or caused the Rietveld refinement to fail. The lattice parameters for ScF₃ from the Rietveld analyses are presented in Supplemental Information.

The unit cell volumes per formula unit (V/Z) for ScF₃ were plotted with respect to temperature at pressure and with respect to pressure at temperature, as shown in Figures 45 and 46, respectively. Straight line fits to $\ln(V)$ vs. T and P were used to calculate average CTEs at pressure and average bulk moduli at temperature (Table 15). The bulk moduli for TaO₂F and ScF₃, calculated from the low temperature–high pressure experiments at HFIR, were plotted with respect to temperature and are presented in Figure 47.

4.4 Discussion

The effects of pressure on the coefficient of thermal expansion for ScF₃ are negligible across the temperature–pressure ranges examined. At ambient pressure, the average volumetric CTE for cubic ScF₃ is -29(1) ppm·K⁻¹; at 0.2 GPa the CTE is -28(2) ppm·K⁻¹. The CTE at 0.3 GPa is -21.9 ppm·K⁻¹; however, this CTE was calculated from only two available

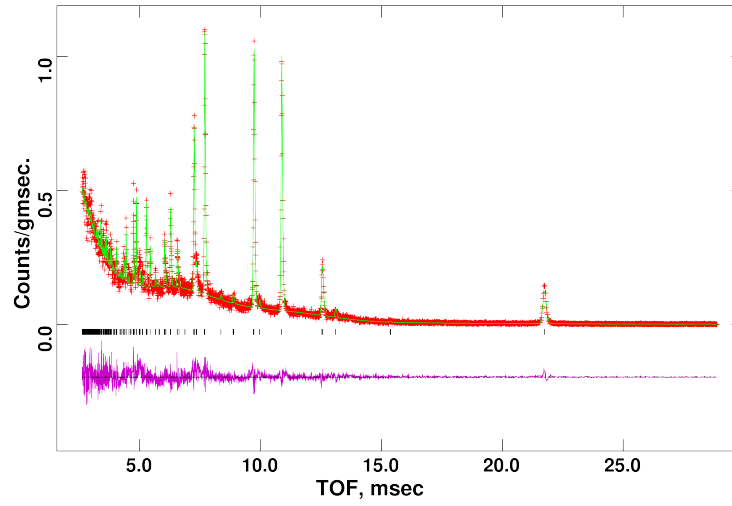


Figure 42: Rietveld fit of the primitive rhombohedral ($R\bar{3}c$) structural model to the 60 K, 0.3 GPa diffraction pattern for TaO₂F-A collected using TOF neutron diffraction at IPNS.

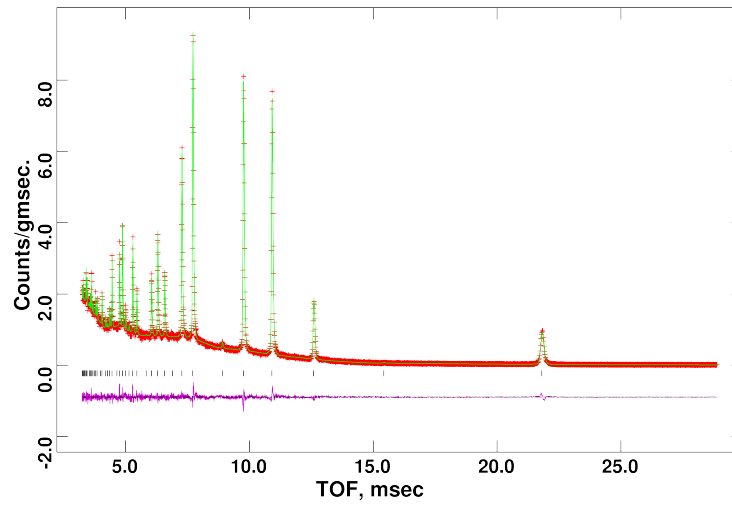


Figure 43: Rietveld fit of the cubic ($Pm\bar{3}m$) structural model to the ambient diffraction pattern collected for TaO₂F-A using TOF neutron diffraction at IPNS.

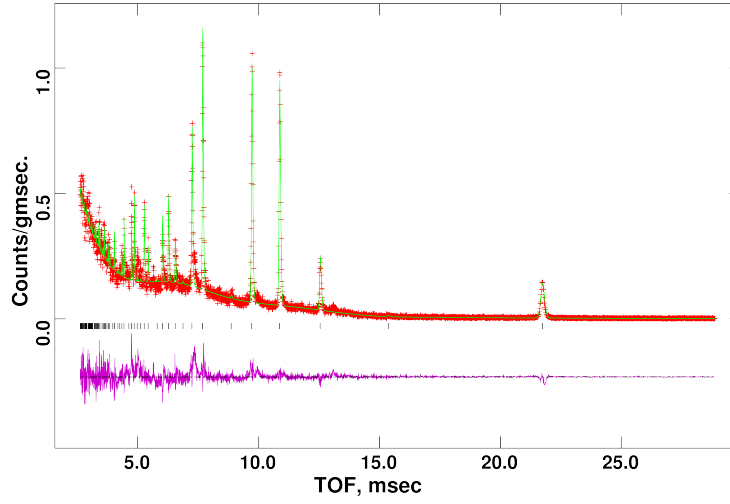


Figure 44: Rietveld fit of the cubic ($Pm\bar{3}m$) model to the 60 K, 0.3 GPa diffraction pattern for TaO₂F-A collected using TOF neutron diffraction at IPNS.

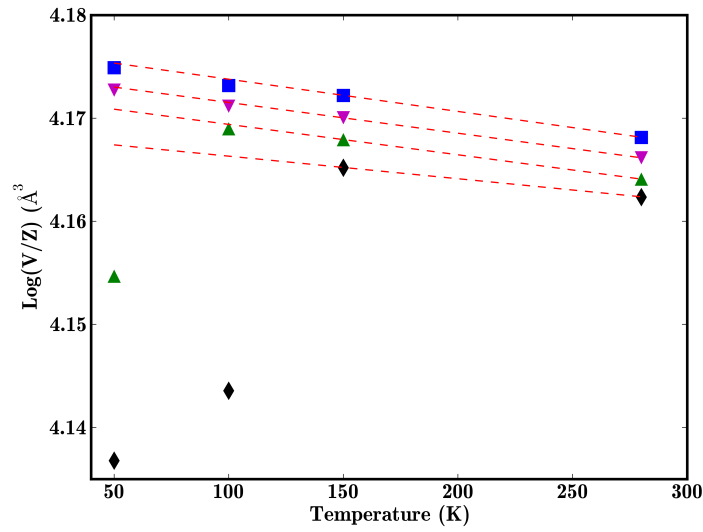


Figure 45: Log of unit cell volume per formula unit for ScF₃, plotted with respect to temperature at 0.007 GPa (blue ■), 0.103 GPa (purple ▽), 0.207 GPa (green △), and 0.310 GPa (black ◇) from data collected at HFIR. The dashed red lines are straight line fits used to estimate average volumetric CTEs. The three data points that do not fall on the straight line fits are for rhombohedral ScF₃.

Table 15: Average volumetric coefficients of thermal expansion for ScF_3 at pressure and average bulk modulus (K) at temperature. **The CTE at 0.310 GPa and the bulk modulus at 50 K were calculated from straight line fits to only two available data points for the cubic phase.

<i>Pressure (GPa)</i>	α_v (ppm·K ⁻¹)
0.007	-29(1)
0.103	-28(1)
0.207	-28(2)
0.310	-21.9**
<i>Temperature (K)</i>	K (GPa)
50	47.6**
100	51(1)
150	47(1)
280	52.0(7)

data points, which may account for the difference between the CTEs observed at lower pressures.

In contrast, application of modest pressure has a dramatic effect on the CTE of TaO_2F between 40 and 280 K. At ambient pressure, the average volumetric CTE for TaO_2F -A is 1.4(4) ppm·K⁻¹; application of only 0.1 GPa results in an increase of the CTE to 7.6(9) ppm·K⁻¹. Increasing the pressure to 0.3 GPa results in the CTE increasing to 32(3) ppm·K⁻¹. The CTE of TaO_2F -B also increases in a similar manner under increased pressure. This behavior is remarkably different from not only ScF_3 , but also that observed for the negative thermal expansion materials $\text{Zn}(\text{CN})_2$ [76] and $\text{Zr}_2(\text{WO}_4)(\text{PO}_4)_2$ [77]. At higher temperatures, between 298 to 523 K, the effects of pressure on the CTE of TaO_2F are less pronounced; the average volumetric CTE for TaO_2F -B at ambient pressure is -0.6(4) ppm·K⁻¹, and application of 0.27 GPa results in the CTE increasing to 5.4(3) ppm·K⁻¹.

A pressure induced phase transition from cubic ($Pm\bar{3}m$) to rhombohedral ($R\bar{3}c$) symmetry is observed for both ScF_3 and TaO_2F . The transition for ScF_3 occurs between 0.207–0.310 GPa when cooled to 100 K, and between 0.103–0.207 GPa when cooled to 50 K. The time of flight diffraction data collected at IPNS for TaO_2F -A provides evidence that TaO_2F -A is rhombohedral at 0.310 GPa when cooled to 60 K, however there is not sufficient data to determine the phase transition temperature as the data collected on HB2A is too low in quality to see where the transition occurred.

The rhombohedral ($R\bar{3}c$) structure arises from cooperative rotation ($a^- a^- a^-$ in Glazer notation) of the MX_6 ($M = \text{Ta, Sc}$; $X = \text{O, F}$) octahedra.[61] The degree of octahedral rotation, ψ , can be calculated using the equation:

$$\tan\psi = 2(x - \frac{1}{2})3^{\frac{1}{2}} \quad (8)$$

where x refers to the position of a given anion, $(x, 0, \frac{1}{4})$, in the hexagonal unit cell. The octahedral tilt angles were calculated for ScF_3 at 0.310 GPa at 50 K and for $\text{TaO}_2\text{F-A}$ at 0.310 GPa, 60 K (from the IPNS data) and are 9.9° and 4.4° , respectively. The phase transition from cubic to rhombohedral symmetry involves cooperative tilting of the MX_6 ($M = \text{Sc, Ta}$; $X = \text{O, F}$) octahedra; in the case of TaO_2F , the anion disorder may hinder this rotation contributing to the gradual reduction in unit cell volume upon cooling/compression.

As indicated in the plot of the bulk modulus versus temperature in Figure 47, the compressibility of ScF_3 remains essentially constant as the temperature is changed. $\text{TaO}_2\text{F-A}$, however, stiffens upon heating between $\approx 150\text{--}300$ K with $\frac{dK_T}{dT} = 0.155(6)$ GPa/K. Between 298 and 523 K, $\frac{dK_T}{dT} = 0.078(7)$ GPa/K for $\text{TaO}_2\text{F-B}$. The positive value for $\frac{dK_T}{dT}$ results in the CTE becoming more positive under compression and is in contrast to the behavior observed in most materials.

For both samples of TaO_2F , the CTE increases under compression and the bulk modulus increases on heating. However, the behavior of the two samples of TaO_2F (Table 13) is quantitatively different. As the same experimental setup was used for both materials, it is unlikely that these differences arise from experimental error. In Chapter 3 it was observed that digestion of TiO_2 in HF resulted in a titanium hydroxyoxyfluoride with Ti vacancies rather than TiOF_2 . $\text{TaO}_2\text{F-A}$ was prepared via digestion of Ta_2O_5 in HF, however IR spectra collected for this material do not support the presence of hydroxyl groups. The Ta site occupancies were refined during the Rietveld analyses of the ambient temperature-pressure TOF neutron diffraction pattern and the ambient diffraction pattern collected on a laboratory PXRD; refinement of the site occupancy for Ta does not indicate the presence of Ta vacancies in this material. There are several known metal hydroxyfluorides in the literature, however, most are formed with a low valence metal (i.e. Zn, Al, Fe, Ti); a

literature search failed to yield any examples of a metal hydroxyfluoride being formed from a higher valence metal such as Ta^{5+} . Coupling these observations with the fact that Ta^{5+} is more acidic than Ti^{4+} [80], which results in Ta^{5+} being more likely to lose the proton of a hydroxyl group and thus being stabilized by the oxide, suggests that the HF digestion synthesis of high valent metals is likely to produce an oxyfluoride free of hydroxyl groups.

A more probable explanation for the differences between $\text{TaO}_2\text{F-A}$ and $\text{TaO}_2\text{F-B}$ is that they have different disordered local structures arising from their different thermal histories. The highest temperature experienced by $\text{TaO}_2\text{F-A}$ was 453 K during synthesis, after which it was slowly cooled to room temperature. Synthesis of $\text{TaO}_2\text{F-B}$ required heating to 483 K and it was quenched to room temperature. Such differences in thermal history could result in changes in the local structure, and impact the material's properties.

The bulk moduli for TaO_2F and ScF_3 calculated at 280 K are slightly lower than reported in previous high pressure studies. In the case of ScF_3 , the bulk modulus at 280 K was estimated to be 52.0(7) GPa, however the bulk modulus for ScF_3 as determined from diamond anvil cell diffraction experiments is 57(3) GPa (Chapter 2). At 280 K the bulk modulus for $\text{TaO}_2\text{F-A}$ and $\text{TaO}_2\text{F-B}$ are 53(1) and 44(1) GPa, respectively. A previous high pressure study of a sample prepared in a similar fashion to $\text{TaO}_2\text{F-A}$ using diamond anvil cells reported a bulk modulus of 60(1) GPa.[45] One possible reason for the differences may be pressure calibration errors; in the case of TaO_2F , the thermal history of the sample must also be taken into account.

The unusual behavior observed for TaO_2F under pressure may be related to the disordered local structure in this material. During the cubic to rhombohedral phase transition that was observed for ScF_3 , there was a pronounced volume change between the two phases. However, for TaO_2F the change in unit cell volume upon cooling/compression was very gradual; this may arise from the disorder of the local structure hindering the cooperative rotation of the octahedra as part of the phase transition.

4.5 Conclusions

Scandium trifluoride, ScF_3 , and tantalum oxyfluoride, TaO_2F , are both framework materials that adopt the cubic ReO_3 structure under ambient conditions. Cubic ScF_3 exhibits strong negative thermal expansion at both ambient and high pressures. An abrupt cubic to rhombohedral phase transition is observed between 0.207 and 0.310 GPa when cooled to 100 K, and between 0.103 and 0.207 GPa when cooled to 50 K.

At ambient pressure, TaO_2F shows close to 'zero' thermal expansion. Application of modest pressure, however, resulted in the CTE becoming more positive; application of 0.310 GPa results in the average volumetric CTE becoming $32.0 \text{ ppm}\cdot\text{K}^{-1}$ between 40 to 280 K. At higher temperatures, the effects of pressure upon the CTE are much less pronounced but still result in the CTE increasing. This effect is in contrast to what is observed in most materials and is associated with a cubic to rhombohedral phase transition that occurs under pressure at low temperatures. The local structural disorder in this material likely impacts the route by which the phase transition occurs, resulting in the unusual effects that are observed.

The use of TaO_2F in any application where it might experience stress would be hindered by the effects of pressure on the CTE of this material. The attempt by Holzer *et al.* to make a mixed metal matrix composite with ZrW_2O_8 showed that pressures of at least ≈ 220 MPa may be experienced; for TaO_2F -A such pressures resulted in a 10-fold increase in the CTE.

4.6 Supplemental Information

Table 16: Unit cell parameters from variable temperature–pressure neutron diffraction experiments on TaO₂F-A at HFIR.

40 K	a (Å)	Vol. (Å ³)
0.007 GPa	3.8777(2)	58.306(5)
0.103 GPa	3.8737(2)	58.128(5)
0.207 GPa	3.8687(2)	57.901(6)
0.310 GPa	3.8622(3)	57.612(7)
80 K	a (Å)	Vol. (Å ³)
0.007 GPa	3.8780(2)	58.311(5)
0.207 GPa	3.8697(2)	57.946(5)
0.310 GPa	3.8634(4)	57.622(9)
120 K	a (Å)	Vol. (Å ³)
0.007 GPa	3.8778(2)	58.313(5)
0.103 GPa	3.8748(2)	58.177(5)
0.207 GPa	3.8709(2)	57.999(5)
0.310 GPa	3.8652(2)	57.744(6)
160 K	a (Å)	Vol. (Å ³)
0.007 GPa	3.8780(2)	58.323(5)
0.103 GPa	3.8753(2)	58.200(5)
0.207 GPa	3.8718(2)	58.040(5)
0.310 GPa	3.8673(3)	57.840(8)
200 K	a (Å)	Vol. (Å ³)
0.007 GPa	3.8780(2)	58.323(5)
0.103 GPa	3.8757(2)	58.217(5)
0.207 GPa	3.8726(2)	58.076(5)
0.310 GPa	3.8692(2)	57.923(5)
240 K	a (Å)	Vol. (Å ³)
0.007 GPa	3.8782(2)	58.328(5)
0.103 GPa	3.8759(2)	58.227(5)
0.207 GPa	3.8732(2)	58.105(5)
0.310 GPa	3.8703(2)	57.972(5)
280 K	a (Å)	Vol. (Å ³)
0.007 GPa	3.8780(2)	58.321(5)
0.103 GPa	3.8761(2)	58.233(5)
0.207 GPa	3.8735(2)	58.119(5)
0.310 GPa	3.8711(2)	58.008(5)

Table 17: Unit cell parameters for TaO₂F-B from Rietveld analyses of low temperature–high pressure neutron diffraction data collected on beamline HB2A at the HFIR

40 K	a (Å)	Vol. (Å ³)
0.008 GPa	3.8964(1)	59.156(4)
0.104 GPa	3.8925(1)	58.978(4)
0.207 GPa	3.8871(1)	58.732(4)
0.310 GPa	3.8803(1)	58.426(6)
60 K	a (Å)	Vol. (Å ³)
0.008 GPa	3.8966(1)	59.164(4)
0.104 GPa	3.8925(2)	58.979(4)
0.207 GPa	3.8874(2)	58.745(5)
0.311 GPa	3.8809(2)	58.451(6)
80 K	a (Å)	Vol. (Å ³)
0.008 GPa	3.8965(2)	59.158(4)
0.104 GPa	3.8927(2)	58.988(4)
0.207 GPa	3.8879(2)	58.767(4)
0.311 GPa	3.8817(2)	58.490(5)
100 K	a (Å)	Vol. (Å ³)
0.007 GPa	3.8965(2)	59.158(4)
0.104 GPa	3.8927(2)	58.987(4)
0.207 GPa	3.8881(2)	58.779(4)
0.311 GPa	3.8822(2)	58.510(5)
120 K	a (Å)	Vol. (Å ³)
0.007 GPa	3.8964(2)	59.156(4)
0.104 GPa	3.8927(2)	58.994(4)
0.207 GPa	3.8884(2)	58.792(4)
0.310 GPa	3.8831(2)	58.551(5)
160 K	a (Å)	Vol. (Å ³)
0.007 GPa	3.8965(2)	59.159(4)
0.104 GPa	3.8931(2)	59.005(4)
0.207 GPa	3.8891(2)	58.825(4)
0.310 GPa	3.8847(2)	58.622(5)
200 K	a (Å)	Vol. (Å ³)
0.007 GPa	3.8962(2)	59.144(4)
0.104 GPa	3.8931(2)	59.007(4)
0.207 GPa	3.8896(2)	58.845(4)
0.311 GPa	3.8856(2)	58.666(5)
240 K	a (Å)	Vol. (Å ³)
0.007 GPa	3.8960(2)	59.136(4)
0.103 GPa	3.8932(2)	59.010(4)
0.207 GPa	3.8901(2)	58.867(4)
0.310 GPa	3.8866(2)	58.710(5)
280 K	a (Å)	Vol. (Å ³)
0.007 GPa	3.8961(2)	59.140(4)
0.103 GPa	3.8933(2)	59.015(4)
0.207 GPa	3.8902(2)	58.873(4)
0.310 GPa	3.8871(2)	58.732(5)

Table 18: Unit cell parameters for TaO₂F-B extracted from Rietveld analyses of the high temperature–high pressure diffraction data collected on beamline 11-ID-B of the APS

0.008 GPa	a (Å)	Vol. (Å ³)
323 K	3.8932(2)	59.009(8)
348 K	3.8931(2)	59.005(9)
373 K	3.8933(2)	59.014(7)
398 K	3.8929(2)	58.994(8)
423 K	3.8931(2)	59.005(7)
473 K	3.8931(2)	59.005(7)
523 K	3.8931(2)	59.005(8)
0.040 GPa	a (Å)	Vol. (Å ³)
298 K	3.8924(1)	58.972(7)
323 K	3.8926(2)	58.981(8)
348 K	3.8923(2)	58.968(8)
373 K	3.8926(2)	58.984(8)
398 K	3.8923(2)	58.970(8)
423 K	3.8928(2)	58.990(8)
473 K	3.8927(2)	58.986(7)
523 K	3.8926(2)	58.982(8)
0.080 GPa	a (Å)	Vol. (Å ³)
298 K	3.8919(1)	58.949(7)
323 K	3.8918(2)	58.946(7)
348 K	3.8917(2)	58.942(7)
373 K	3.8920(2)	58.954(7)
398 K	3.8917(2)	58.940(7)
423 K	3.8920(2)	58.953(7)
473 K	3.8920(2)	58.953(7)
523 K	3.8920(2)	58.954(7)
0.120 GPa	a (Å)	Vol. (Å ³)
298 K	3.8910(1)	58.907(6)
323 K	3.8912(2)	58.918(6)
348 K	3.8908(2)	58.901(8)
373 K	3.8912(2)	58.920(7)
398 K	3.8909(2)	58.906(7)
423 K	3.8913(2)	58.922(7)
473 K	3.8913(2)	58.925(7)
523 K	3.8914(2)	58.926(7)
0.160 GPa	a (Å)	Vol. (Å ³)
298 K	3.8902(1)	58.874(7)
323 K	3.8903(2)	58.877(7)
348 K	3.8901(2)	58.871(7)
373 K	3.8905(2)	58.887(7)
398 K	3.8902(2)	58.874(7)
423 K	3.8907(2)	58.894(7)
473 K	3.8907(2)	58.895(7)
523 K	3.8906(2)	58.890(7)
0.200 GPa	a (Å)	Vol. (Å ³)
298 K	3.8894(1)	58.836(7)
323 K	3.8896(2)	58.845(7)
348 K	3.8893(2)	58.834(7)
373 K	3.8898(2)	58.857(7)
398 K	3.8894(2)	58.835(7)
423 K	3.8899(2)	58.859(7)
473 K	3.8899(2)	58.861(7)
523 K	3.8899(2)	58.859(7)
0.240 GPa	a (Å)	Vol. (Å ³)
298 K	3.8886(1)	58.807(6)
323 K	3.8887(2)	58.805(7)
348 K	3.8886(2)	58.798(7)
373 K	3.8891(2)	58.823(7)
398 K	3.8887(1)	58.805(7)
423 K	3.8892(1)	58.829(7)
473 K	3.8894(2)	58.834(7)
523 K	3.8892(2)	58.826(7)
0.270 GPa	a (Å)	Vol. (Å ³)
298 K	3.8880(1)	58.771(7)
323 K	3.8882(2)	58.780(7)
348 K	3.8880(2)	58.774(7)
373 K	3.8886(1)	58.798(7)
398 K	3.8882(1)	58.812(7)
423 K	3.8888(1)	58.810(7)

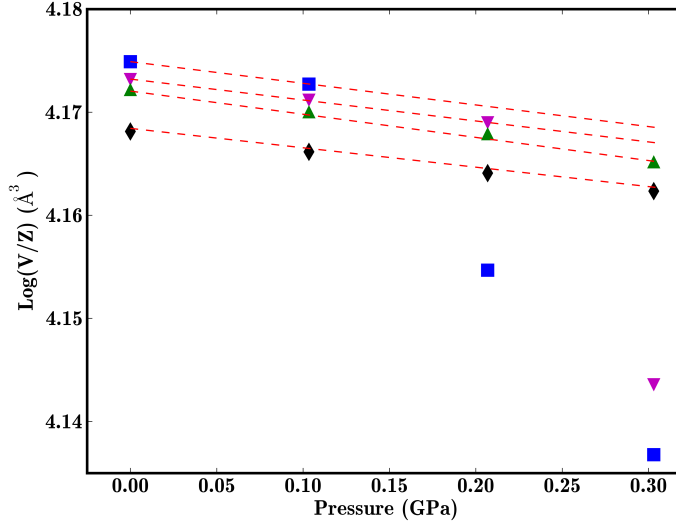


Figure 46: Log of unit cell volume per formula unit (V/Z) for ScF_3 , plotted with respect to pressure at 280 K (black \diamond), 150 K (green \triangle), 100 K (purple ∇), and 50 K (blue \blacksquare) from data collected at HFIR. The dashed red lines are straight line fits used to estimate the average bulk modulus. The data points at 50 K above 0.2 GPa and at 100 K above 0.3 GPa correspond to the rhombohedral unit cell

Table 19: Unit cell parameters from variable temperature–pressure neutron diffraction experiments for ScF_3

50 K	a (Å)	c (Å)	Vol. (Å ³)
0.007 GPa	4.02140(2)		65.033(5)
0.103 GPa	4.01850(2)		64.892(5)
0.207 GPa	5.63928(7)	13.90581(2)	382.35(5)
0.310 GPa	5.59350(1)	13.85936(3)	375.67(5)
100 K	a (Å)	c (Å)	Vol. (Å ³)
0.007 GPa	4.01910(2)		64.921(5)
0.103 GPa	4.10641(2)		64.791(5)
0.207 GPa	4.01641(2)		64.649(5)
0.310 GPa	5.61213(1)	13.85414(3)	378.165(5)
150 K	a (Å)		Vol. (Å ³)
0.007 GPa	4.01779(2)		64.858(5)
0.103 GPa	4.01491(2)		64.718(5)
0.207 GPa	4.01207(2)		64.581(5)
0.310 GPa	4.00841(3)		64.405(8)
280 K	a (Å)		Vol. (Å ³)
0.007 GPa	4.01235(2)		64.595(5)
0.103 GPa	4.00972(2)		64.467(5)
0.207 GPa	4.00696(2)		64.334(5)
0.310 GPa	4.00462(3)		64.222(6)

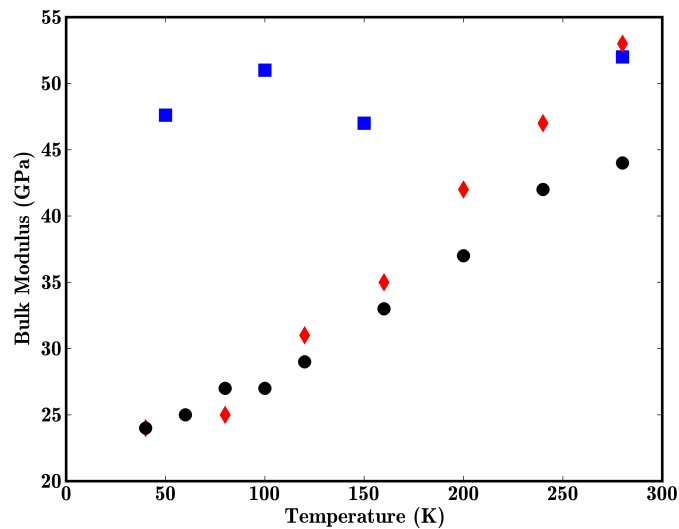


Figure 47: The average bulk modulus for TaO₂F-A (red \diamond), TaO₂F-B (black \circ), and ScF₃ (blue \blacksquare) plotted with respect to temperature.

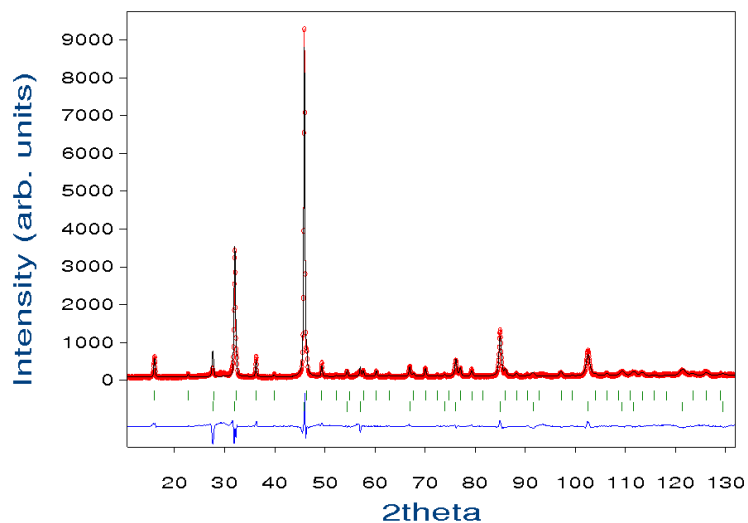


Figure 48: Rietveld fit to the 280 K, ambient pressure diffraction pattern collected for ScF₃. The top set of reflection markers correspond to ScF₃, the bottom set to FCC Al (sample cell).

CHAPTER V

LOCAL STRUCTURE OF TaO_2F AND TiOF_2

5.1 Introduction

The cubic ReO_3 structure is commonly used as an illustrative example of how negative thermal expansion (NTE) might arise from the transverse thermal motion of bridging moieties and the coupled rotation of rigid units; in Chapter 2, the pronounced thermal expansion of ScF_3 , which adopts the ReO_3 structure type, was discussed and highlights how materials with this structure type may exhibit NTE. In addition to ScF_3 , other materials are known to adopt the cubic ReO_3 structure type. Tantalum oxyfluoride, TaO_2F , has a cubic ReO_3 type structure at room temperature and has been shown to exhibit zero thermal expansion.[35] Titanium oxyfluoride, TiOF_2 , has been previously reported to adopt the cubic ReO_3 structure type, but a recent study by Shian *et al.* showed that this material adopts a rhombohedrally distorted variant of the ReO_3 structure at room temperature while maintaining ReO_3 type connectivity;[27, 67, 69] in Chapter 3, the thermal expansion of TiOF_2 was examined and it was found to exhibit positive thermal expansion at all temperatures. In both of these oxyfluorides, there is a disordered distribution of O and F over the available anion positions.

The long-range average structures for TaO_2F and TiOF_2 are very simple and have a statistical distribution of oxygen and fluorine atoms over the available anion sites. However, O and F are chemically different from one another; therefore it is expected that they would prefer different bond lengths as the stronger $M\text{--O}$ bond should be shorter than the $M\text{--F}$ bond. The local, short range structure (on the nanoscale) of TaO_2F and TiOF_2 should be quite different from the average structure due to the different bonding requirements. In a recent electron diffraction study of NbO_2F , Brink reported that there was one-dimensional ordering of the O and F with unequal $\text{Nb}\text{--}X$ ($X = \text{O}, \text{F}$) bond lengths and significant static displacements of Nb from the ideal cation site.[81] Based on a variable temperature

neutron diffraction study of TaO₂F, Tao reported large transverse atomic displacement parameters (ADPs) for the anions that persisted at low temperatures; they speculated that these large ADPs likely arise from static tilting of the TaO₄F₂ octahedra and the possibility of non-linear Ta–(O/F)–Ta links.[35]

Diffraction patterns of crystalline materials possess sharp Bragg reflections arising from the long-range order; analysis of these reflections allows determination of the average crystal structure. Diffraction patterns also contain diffuse scattering, which is not used in Rietveld type analyses of diffraction data. The diffuse scattering portion of a diffraction pattern contains information regarding the local structure of materials. Using the 'total scattering' approach, it is possible to use both the Bragg and diffuse scattering portions of a diffraction pattern simultaneously to compute atomic pair distribution functions (PDFs).

The atomic PDF, $G(r)$, is defined as:

$$G(r) = 4\pi r[\rho(r) - \rho_0] \quad (9)$$

where ρ_0 is the average number density, $\rho(r)$ is the atomic pair-density, and r is a radial distance.[82] The PDF, $G(r)$, gives information about the number of atoms in a spherical shell at a distance r from a reference atom. The PDF is obtained from neutron or X-ray powder diffraction patterns through a Fourier transformation of the total scattering structure function:

$$G(r) = 2\pi \int_{Q=0}^{Q_{max}} Q[S(Q) - 1]\sin(Qr) dQ \quad (10)$$

where $S(Q)$ is the total scattering structure function and is derived from the measured scattered intensity.[82] The structure function is defined as:

$$S(Q) = \frac{I^{coh}(Q) - \sum c_i |f_i(Q)|^2}{|\sum c_i f_i(Q)|^2} + 1 \quad (11)$$

where $I^{coh}(Q)$ is the measured coherent scattering intensity from a powdered sample (which has been corrected for background and other experimental artifacts and normalized by the flux and the number of atoms in the sample), c_i is the atomic concentration, and f_i are the X-ray atomic form factors.[82] The scattered intensity is measured as a function of Q , where Q is:

$$Q = \frac{4\pi \sin\theta}{\lambda} \quad (12)$$

The atomic PDF is a probability distribution function in real space which gives the probability of finding pairs of atoms in the material separated by a distance, r . The peak positions in the PDF correspond to bond lengths between atoms, the peak integrated intensity provides information about coordination number, and the peak width is related to thermal or static disorder in the system. As the PDFs from total scattering experiments contain information concerning both the local structure and the long range ordering in a material, they are an ideal tool for studying disordered crystalline materials such as the oxyfluorides TiOF_2 and TaO_2F .

Growing interest in the study of disordered materials has resulted in the development of dedicated high energy X-ray diffraction beamlines (necessary to provide diffraction data to high values of Q), advancements in software for PDF extraction and modeling, and advances in the instrumentation for rapid acquisition of total scattering data.[83] Historically, the collection of diffraction data to the high values of Q required for PDF analysis took a long time; it is now possible to obtain high-quality PDFs with only a few seconds of data collection.[83] The ability to rapidly acquire data makes it possible to readily examine the local structure changes in response to external stimuli such as temperature or pressure.

ScF_3 and TaO_2F both adopt the cubic ReO_3 structure type, but their thermal expansion properties are different.[33, 35] The differences in their behavior may be related to the disordered local structure of TaO_2F . In the following, the local structures of TaO_2F and TiOF_2 are examined using pair distribution functions obtained from total scattering experiments.

5.2 *Experimental*

5.2.1 Sample Preparation

TaO_2F had been prepared previously¹ by dissolving Ta_2O_5 (STREM Chemicals, 99.8% metals basis) in a Pt crucible with concentrated HF (Mallinckrodt, 48%) followed by slow evaporation to dryness. The remaining powder was transferred to a Teflon container and heated at 453 K for 10 hours.

¹This sample was prepared by Mehmet Cetnikol.

TiOF₂ was prepared by heating TiO₂ (anatase, STREM Chemicals, 99% metals basis) with TiF₄ (Alfa Aesar, 98% metals basis). The starting reagents (including 15% excess TiF₄ over that required by stoichiometry) were combined in an argon-filled glove box using a mortar and pestle. The reaction mixture was sealed inside a copper tube fitted with brass Swagelok compression fittings to create an air-tight vessel. The mixture was heated at 493 K for 18 hours followed by quenching in water to room temperature.

5.2.2 Total Scattering Data Collection

Variable temperature total scattering diffraction data for TaO₂F were collected on beamline 1-ID-C of the Advanced Photon Source (APS), Argonne National Laboratory using high energy X-rays ($\lambda=0.18505$ Å); temperature control was provided using an Oxford Cryosystems Cryostream. Diffraction data were collected for TiOF₂ on beamline 11-ID-B of the APS using high energy X-rays ($\lambda=0.21280$ Å)². The two dimensional diffraction images were recorded on a GE amorphous Si detector with the samples held in Kapton capillaries. Ceria (CeO₂, NIST 674a) was used as a calibrant for sample-to-detector distance, detector tilt angle, detector tilt plane rotation angle, and beam center. A scattering pattern was recorded from an empty Kapton capillary to be used for background subtraction.

5.2.3 Diffraction Data Processing

The two dimensional diffraction patterns were integrated using the program Fit2D.[50] Pair distribution functions were calculated from the diffraction patterns using the program PDFgetX2.[84] Standard corrections, including background subtraction, sample absorption, and empirical energy dependence of the detection efficiency, were performed within PDFgetX2 prior to PDF extraction.

5.3 Results

5.3.1 Titanium Oxyfluoride

Different structural models were fit to the pair distribution function for cubic TiOF₂ collected at 500 K using the program PDFgui.[85] As seen in Figure 49, the cubic ($Pm\bar{3}m$)

²The total scattering diffraction data for both TaO₂F and TiOF₂ were collected by Dr. Karena W. Chapman of the Advanced Photon Source, Argonne National Laboratory.

structural model, which was used in the Rietveld analysis of the cubic TiOF_2 diffraction data, is not appropriate to describe the local structure of this material as it does not account for differing $\text{Ti}-X$ ($X = \text{O}, \text{F}$) bond lengths. To examine the local structure of TiOF_2 while accounting for differing $\text{Ti}-X$ bond lengths, two different tetragonal ($P4/mmm$) models, derived from those used in a previous DFT study of TiOF_2 [63], were explored over a limited range ($r = 1.2$ to 10 \AA). In the first tetragonal model (Figure 50, Table 20) the oxygen atoms are all confined to the equatorial ($a - b$) plane (Supplemental Information, Figure 62); the second tetragonal model (Figure 51, Table 21) has the oxygen atoms out of this plane (Supplemental Information, Figure 63).

Table 20: The final atomic positions in the tetragonal cell with the oxygen atoms in the $a - b$ plane used to fit the low r portion of the PDF for cubic TiOF_2 . The refined lattice constants for the model were: $a=b=7.510(9) \text{ \AA}$ and $c=3.921(1) \text{ \AA}$.

<i>Atom</i>	<i>x</i>	<i>y</i>	<i>z</i>
Ti	0.7598(6)	0.7598(6)	0.0
Ti	0.2402(6)	0.2402(6)	0.0
Ti	0.2402(6)	0.7598(6)	0.0
Ti	0.7598(6)	0.2402(6)	0.0
O	0.0	0.76(3)	0.0
O	0.0	0.24(3)	0.0
O	0.24(3)	0.0	0.0
O	0.76(3)	0.0	0.0
F	0.5	0.748(6)	0.0
F	0.5	0.252(6)	0.0
F	0.252(6)	0.5	0.0
F	0.748(6)	0.5	0.0
F	0.762(3)	0.762(3)	0.5
F	0.238(3)	0.238(3)	0.5
F	0.238(3)	0.762(3)	0.5
F	0.762(3)	0.238(3)	0.5

During the fit of the tetragonal models to the PDF, unit cell constants, scale factor, atomic correlation factor³, atom positions within the unit cell, and isotropic atomic displacement parameters for each unique atom were refined. The tetragonal model with the oxygen atoms out of the ($a - b$) plane resulted in a slightly better fit ($R_W=0.170$) than the model where oxygens were in the equatorial $a - b$ plane ($R_W=0.206$), however this model

³The atomic correlation factor is the coefficient for the $1/r$ or $1/r^2$ contribution to the peak sharpening.[85]

resulted in a shorter than expected Ti–F bond length of 1.807 Å. After a minimum in R_W was observed during refinement of this model with the oxygens out of the $a - b$ plane, the oxygen atoms were placed back into the $a - b$ plane and the refinement was performed again; this resulted in an even lower R_W of 0.164 (Figure 52). The final structural model and structural drawings of the tetragonal models are presented in Supplemental Information. The Ti–(O/F)–Ti bond lengths and Ti–Ti separations in each model were calculated within PDFgui[85], and the Ti–X–Ti bond angles were calculated from these lengths (Table 22).

5.3.2 TaO₂F

The cubic $Pm\bar{3}m$ structural model was fit to the 80 K PDF of TaO₂F using the program PDFgui.[85] As seen in Figure 53, this model is in good agreement with the data at high r values ($>\approx 9$ Å); however, the cubic model is not appropriate for describing the local structure of TaO₂F because of the differing Ta–F and Ta–O bond lengths. A model for the local structure was constructed using a 3x3x3 supercell.⁴

The starting supercell was formed from the cubic $Pm\bar{3}m$ structural model. The O and F atoms were distributed over the available anion positions to produce TaO₄F₂ octahedra. Using a computer spreadsheet, a displacement parameter was added to each of the Ta atomic positions such that Ta was displaced towards the oxygen atoms resulting in shorter Ta–O and longer Ta–F bonds. After each variation of the displacement parameter, the model was checked against the PDF using the program PDFgui until a minimum in R_W was observed.[85] Once the minimum R_W was observed from the Ta displacements, the new Ta atomic coordinates were kept fixed and the oxygen and fluorine atomic positions were displaced perpendicular to the Ta–X–Ta axis by addition of a displacement parameter. After each variation of the parameter, the model was checked against the experimentally derived PDF in PDFgui until a minimum in R_W was observed. As seen in Figure 54, the resulting model is in good agreement with the experimental PDF ($r = 1.2\text{--}10$ Å) for TaO₂F. The Ta–X–Ta bond angles and Ta–X bond lengths from the fit are presented in Table 23

⁴The initial 3x3x3 supercell used to model the local structure of TaO₂F was constructed by Mehmet Cetnikol with the help of Dr. Karena W. Chapman of the APS, Argonne National Lab.

Table 21: The final atomic positions in the tetragonal cell with the oxygen atoms out of the $a - b$ plane used to fit the low r portion of the PDF for cubic TiOF_2 . The refined lattice constants for this model were: $a=b=7.521(2)$ Å and $c=3.905(2)$ Å.

<i>Atom</i>	<i>x</i>	<i>y</i>	<i>z</i>
Ti	0.760(1)	0.760(1)	0.0
Ti	0.240(1)	0.240(1)	0.0
Ti	0.240(1)	0.760(1)	0.0
Ti	0.760(1)	0.240(1)	0.0
O	0.769(3)	0.769(3)	0.5
O	0.231(3)	0.231(3)	0.5
O	0.231(3)	0.769(3)	0.5
O	0.769(3)	0.231(3)	0.5
F	0.0	0.76(1)	0.0
F	0.0	0.24(1)	0.0
F	0.24(1)	0.0	0.0
F	0.76(1)	0.0	0.0
F	0.5	0.74(2)	0.0
F	0.5	0.26(2)	0.0
F	0.26(2)	0.5	0.0
F	0.74(2)	0.5	0.0

Table 22: Ti- X -Ti ($X = \text{O}, \text{F}$) bond angles, Ti- X bond lengths, and Ti-Ti bond lengths calculated from tetragonal model fits to the low r (1.2–10 Å) range of the PDF for cubic TiOF_2 at 500 K. Model 1 places the oxygen atoms in the equatorial $a - b$ plane, and Model 2 places the oxygen atoms out of the $a - b$ plane. *Ti-F-Ti out of the $a - b$ plane; ** with the oxygen atoms placed back into the $a - b$ plane after a minimum in R_W was observed in model 2.

Model 1			
<i>Link</i>	<i>Angle</i>	Ti- X Å	Ti-Ti Å
Ti-O-Ti	180.0°	1.804(7)	3.61(1)
Ti-F-Ti	174.7°	1.953(9)	3.90(1)
Ti-F-Ti*	180.0°	1.961(6)	3.92(1)
Model 2			
<i>Link</i>	<i>Angle</i>	Ti- X Å	Ti-Ti Å
Ti-O-Ti	177.4°	1.953(9)	3.91(1)
Ti-F-Ti	170.0°	1.961(6)	3.91(1)
Ti-F-Ti	180.0°	1.807(7)	3.61(1)
Model 2**			
<i>Link</i>	<i>Angle</i>	Ti- X Å	Ti-Ti Å
Ti-O-Ti	177.3°	1.805(8)	3.61(1)
Ti-F-Ti	172.2°	1.956(7)	3.90(1)
Ti-F-Ti*	176.3°	1.958(7)	3.91(1)

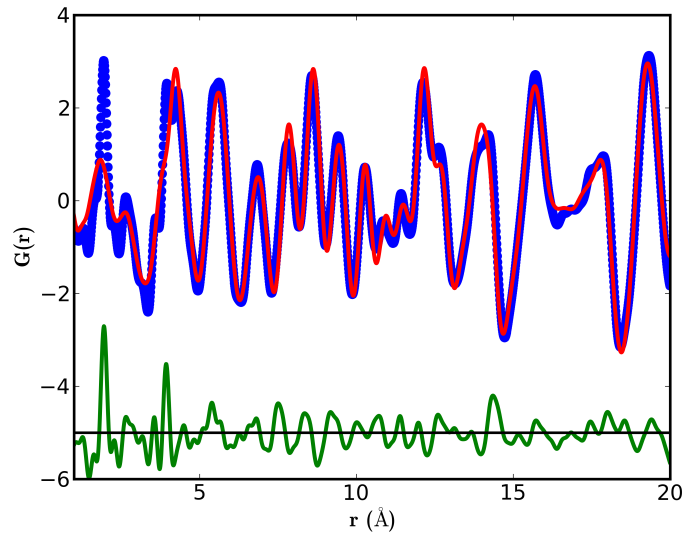


Figure 49: Fit of the cubic $Pm\bar{3}m$ model (red $-$) to the 500 K PDF (blue \circ) to the X-ray PDF for TiOF_2 . The green ($-$) is the difference curve between the fit and the data.

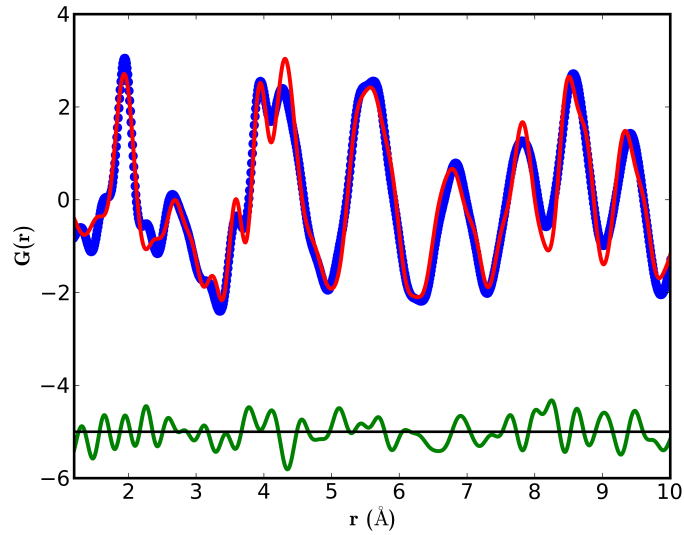


Figure 50: Fit of a tetragonal model (red $-$) with the oxygen atoms in the equatorial $a - b$ plane to the low r portion of the PDF (blue \circ) of cubic TiOF_2 (at 500 K). The green ($-$) is the difference curve between the fit and the data.

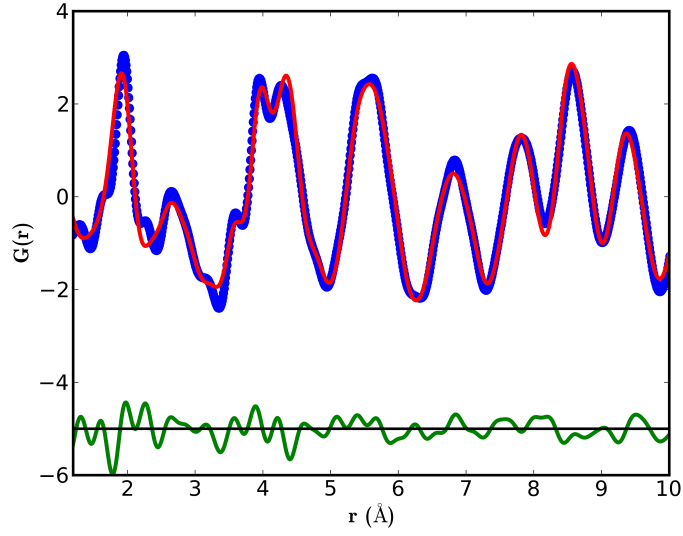


Figure 51: Fit of a tetragonal model (red $-$) with the oxygen atoms out of the $a - b$ plane to the low r portion of the PDF (blue \circ) of cubic TiOF_2 (at 500 K). The green ($-$) is the difference curve between the fit and the data.

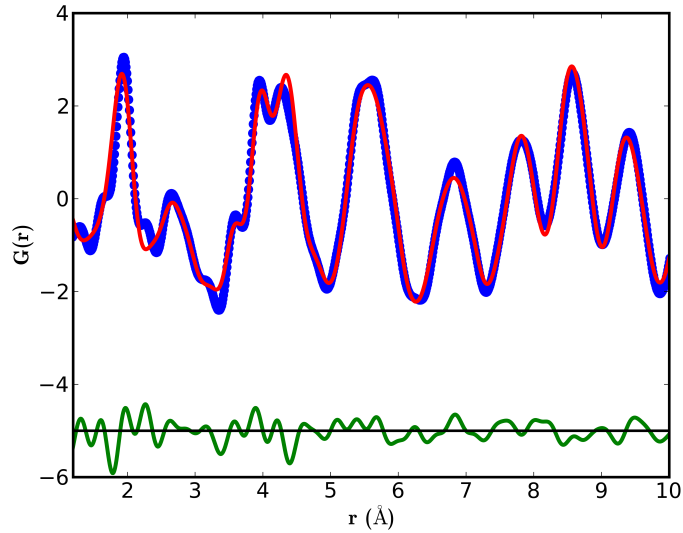


Figure 52: Fit of a tetragonal model (red $-$) to the low r portion of the PDF (blue \circ) of cubic TiOF_2 (at 500 K). The initial refinement of this model placed the oxygen atoms out of the $a - b$ plane and once a minimum in R_W was observed they were placed back into the $a - b$ plane for further refinement. The green ($-$) is the difference curve between the fit and the data.

and a layer of the atom positions on the (0 0 1) plane is presented in Figure 55. The final structural model is provided in Supplemental Information.

Table 23: Ta–X–Ta ($X = \text{O}, \text{F}$) bond angles and Ta–X bond lengths from the fit of a 3x3x3 supercell to the low r (1.2–10 Å) portion of the 80 K PDF of TaO₂F. There are no ESDs on the values as the model was optimized by hand.

<i>Link</i>	<i>Angle</i>	Ta–X Å	Ta–Ta Å
Ta–F–Ta	174.0°	2.0501	4.0946
Ta–F–Ta	168.0°	2.0586	4.0946
Ta–F–Ta	173.3°	2.0617	4.1073
Ta–F–Ta	175.8°	2.0698	4.1200
Ta–O–Ta	180.0°	1.8858	3.7716
Ta–O–Ta	167.0°	1.8980	3.7716
Ta–O–Ta	173.5°	1.8888	3.7716

In order to examine the expansion of the average structure of TaO₂F, the cubic $Pm\bar{3}m$ structural model was fit to the high r ($r = 10\text{--}30$ Å) region of the variable temperature PDFs (Supplemental Information, Figure 64) and the cubic lattice constants were extracted; the average linear CTE was estimated to be 0.75(5) ppm·K^{−1} from a straight line fit through the $\ln(a)$ versus temperature data (Supplemental Information, Figure 65). In order to examine the changes in the local structure of TaO₂F in response to temperature, a Gaussian was fit to the Ta–O–Ta and Ta–F–Ta peaks in the PDF. A script was written that allowed for automated peak fitting so that each fit was done in a consistent manner. The Ta–F–Ta peak has a broad shoulder arising from the Ta–X bond across the face diagonal. During the fit of the Ta–F–Ta peak, the fit range was fixed at 4.0–4.25 Å, which truncated the right side of the peak. To ensure that the estimated changes in peak position were real, and not a result of artifacts from the Fourier transform used to obtain the PDFs, the peaks were fit to PDFs obtained using two different Q_{max} ($Q_{max} = 25$ and 25.9 Å^{−1}) and to PDFs that had been smoothed by averaging over $2\pi/Q_{max}$. The distances estimated by this approach are shown in Figures 56–61. The average coefficients of thermal expansion of the Ta–X–Ta links were calculated using the 80 K and 440 K distances and are presented in Table 24.

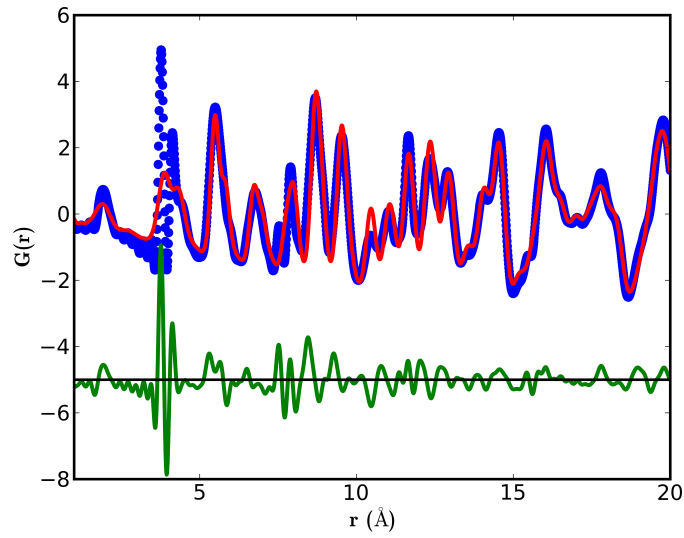


Figure 53: Fit of the cubic $Pm\bar{3}m$ model (red $-$) to the 80 K PDF (blue \circ) of TaO_2F . The green $-$ is the difference curve between the fit and the data.

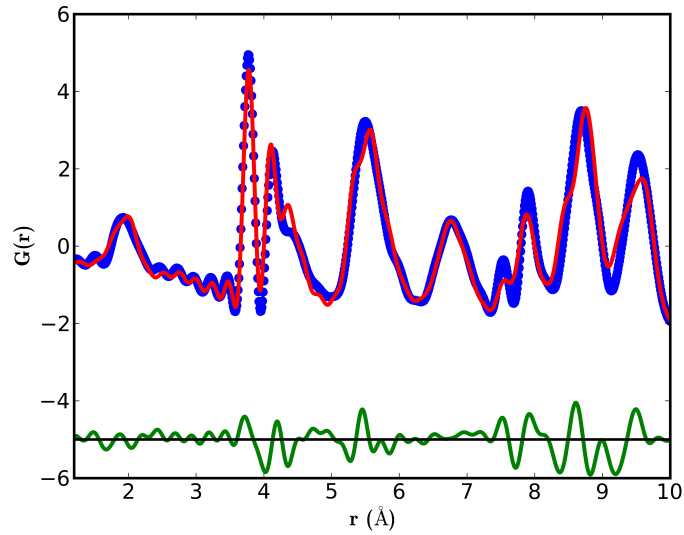


Figure 54: Fit of a $3\times 3\times 3$ supercell with bent Ta-F-Ta links (red $-$) to the low r portion of the PDF (blue \circ) of TaO_2F at 80 K. The green $-$ is the difference curve between the fit and the data.

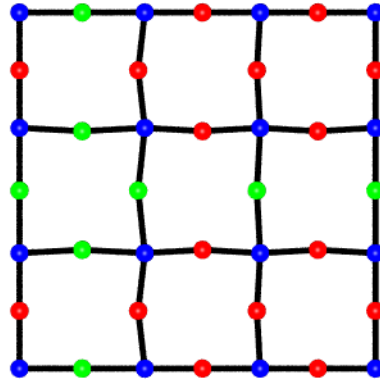


Figure 55: View of the atom positions on the (0 0 1) plane in the 3x3x3 supercell used to model the local structure of TaO_2F . The blue spheres represent Ta, the green spheres represent F, and the red spheres represent O.

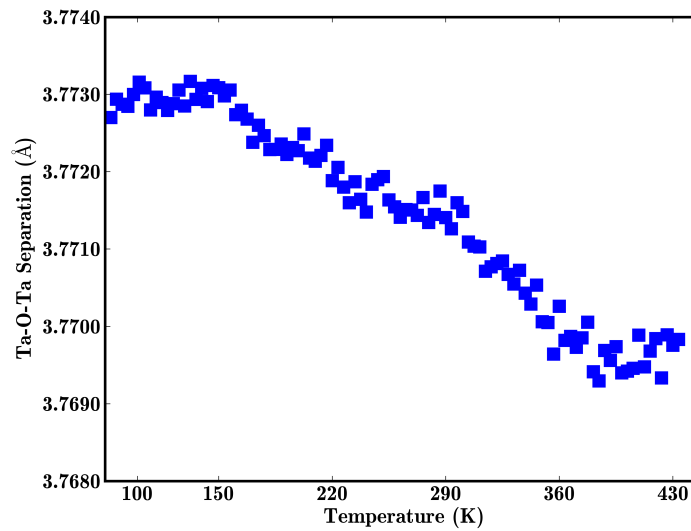


Figure 56: The Ta–O–Ta separation in TaO_2F as a function of temperature. The inter-atomic separation was determined from a Gaussian fit to the peak in the atomic PDF. The Q_{max} used was 25.9 \AA^{-1} . The average linear coefficient of thermal expansion is $-2.1 \text{ ppm}\cdot\text{K}^{-1}$.

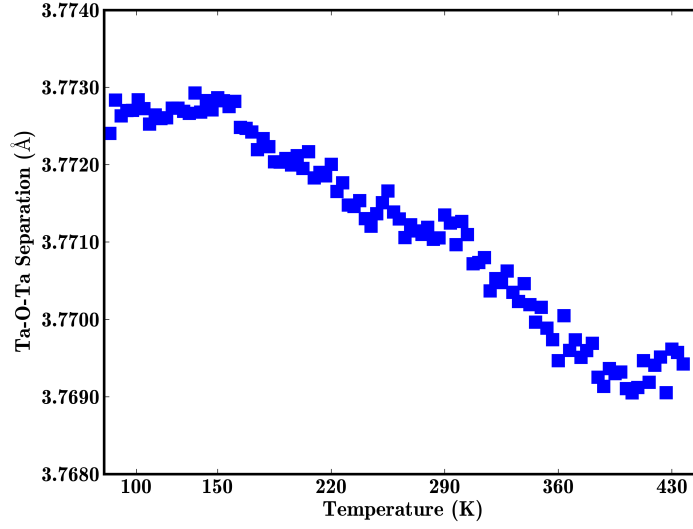


Figure 57: The Ta–O–Ta separation in TaO₂F as a function of temperature. The inter-atomic separation was determined from a Gaussian fit to the peak in the atomic PDF. The Q_{max} used was 25.0 Å⁻¹. The average linear coefficient of thermal expansion is -2.2 ppm·K⁻¹.

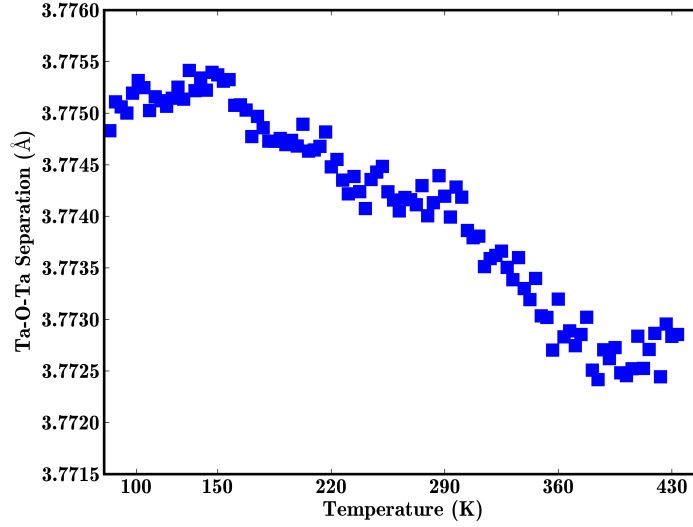


Figure 58: The Ta–O–Ta separation in TaO₂F as a function of temperature. The inter-atomic separation was determined from a Gaussian fit to the peak in the atomic PDF. The Q_{max} used was 25.9 Å⁻¹ and the PDF was smoothed by averaging over $2\pi/Q_{max}$. The average linear coefficient of thermal expansion is -1.5 ppm·K⁻¹.

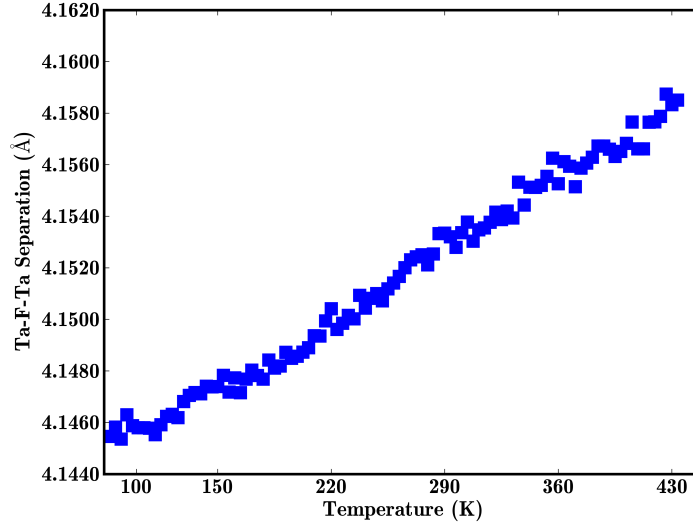


Figure 59: The Ta–F–Ta separation in TaO₂F as a function of temperature. The inter-atomic separation was determined from a Gaussian fit to the peak in the atomic PDF. The Q_{max} used was 25.9 Å⁻¹ and the PDF was smoothed by averaging over $2\pi/Q_{max}$. The average linear coefficient of thermal expansion is 8.7 ppm·K⁻¹.

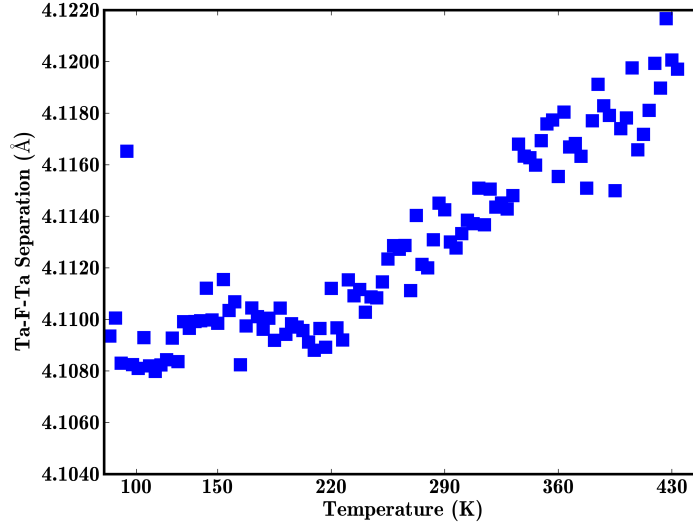


Figure 60: The Ta–F–Ta separation in TaO₂F as a function of temperature. The inter-atomic separation was determined from a Gaussian fit to the peak in the atomic PDF. The Q_{max} used was 25.9 Å⁻¹. The average linear coefficient of thermal expansion is 7.0 ppm·K⁻¹.

Table 24: The average linear coefficients of thermal expansion of the Ta- X -Ta ($X = \text{O}, \text{F}$) links in TaO₂F. Q_{max} is the value used in the calculation of PDFs from the total scattering data. The average linear CTE for TaO₂F, calculated from fits to the long range ($r = 10\text{--}30$ Å) is presented as Ta- X -Ta.

<i>Link</i>	Q_{max} , Å ⁻¹	CTE, ppm·K ⁻¹
Ta-O-Ta	25.9	-2.1(4)
Ta-O-Ta	25.9, smoothed	-1.5(2)
Ta-O-Ta	25.0	-2.2(3)
Ta-F-Ta	25.9	7.0(3)
Ta-F-Ta	25.9, smoothed	8.7(1)
Ta-F-Ta	25.0	3.0(3)
Ta- X -Ta	25.9	0.75(5)

5.4 Discussion

While both TaO₂F and TiOF₂ have simple average structures, the local structure of both of these materials is more complex. Analysis of the atomic pair distribution functions, which were calculated from X-ray total scattering experiments, indicates the presence of differing M - X - M ($M = \text{Ta}, \text{Ti}; X = \text{O}, \text{F}$) links in both of these materials. While the models for the local structures of TiOF₂ and TaO₂F were quite different, they both resulted in good fits to the low r portion of the PDFs and suggest the presence of non-linear M - X - M linkages.

In order for negative thermal expansion to arise in framework materials comprised of corner sharing octahedra, the M - X - M linkages should be close to linear. When the links are linear (or close to linear), the transverse thermal motion of the bridging moiety across the M - M axis can bring the metal atoms closer together. When the links are significantly bent, the transverse thermal motion of the bridging moiety can result in the metal atoms being pushed further apart resulting in positive thermal expansion.

An simple analysis of the variable temperature total scattering data for TaO₂F indicates that the Ta-O-Ta linkage contracts on heating, while the Ta-F-Ta linkage expands on heating (see Figures 56–61). One possible explanation for this material exhibiting close to zero thermal expansion, rather than NTE, is that the contraction of the Ta-O-Ta linkages is offset by the expansion of the Ta-F-Ta linkages. The expansion of the Ta-F-Ta links may arise from an elongation of the Ta-F bond, or it may arise if the Ta-F-Ta links are

significantly bent and the transverse thermal motion of the F atom results in the Ta-Ta separation increasing.

The average CTEs for the Ta- X -Ta links are provided in Table 24; the CTEs calculated from the PDFs that were extracted using a Q_{max} of 25 Å⁻¹ were -2.2 ppm·K⁻¹ and 3.1 ppm·K⁻¹ for Ta-O-Ta and Ta-F-Ta, respectively. However, there was a considerable amount of variation in the CTEs calculated for the Ta-F-Ta links; the differing values in the CTE for the Ta-F-Ta links may arise because the Gaussian fit to the peak neglected the shoulder on the right of the peak. The shoulder on the peak arises from the Ta- X bond across the face diagonal of the unit cell, and there may be a temperature dependence to this bond which manifests itself as a change in the apparent position for the Ta-F-Ta peak. While the explanation for near zero thermal expansion in TaO₂F (the contraction of the Ta-O-Ta links being offset by the expansion of the Ta-F-Ta links) is not entirely consistent with the models used here to describe the local structure, future work examining the local structures of these materials should explore more complex models that consist of linear M -O- M links and bent M -F- M links.

The structural models used to examine the local structures of both TiOF₂ and TaO₂F resulted in a variety of M - X - M linkages. In TiOF₂, both models fit to the local structure resulted in there being Ti-F-Ti links that were significantly more bent than the Ti-O-Ti links. The supercell model used to fit the structure of TaO₂F resulted in both bent Ta-O-Ta and Ta-F-Ta links. However, the models used to describe the local structures of these materials are too simple. In the case of TiOF₂, each of the models assumes that there is tetragonal symmetry and long range ordering of oxygen and fluorine; this model is not appropriate to determine what, if any, ordering exists. For the case of TaO₂F, an ordered arrangement of oxygen and fluorine atoms was used to maintain TaO₄F₂ octahedra in a 3x3x3 supercell. This is still too simple to fully model the local structure. However, all of the models used do emphasize the fact that there are very distinct M - X - M linkages in these oxyfluorides, and the data for TaO₂F suggest different links respond differently to temperature.

5.5 *Conclusions*

The local structures of TiOF_2 and TaO_2F are quite different from their average structures. Simple models were used to describe the local structures of both of these materials, and these models indicate that there are geometrically distinct $M-X-M$ linkages in these materials. Using simple peak fitting to the Ta- X -Ta correlation peaks in the variable temperature PDFs, it was observed that the Ta-O-Ta linkage contracts on heating whereas the Ta-F-Ta linkage probably expands on heating. The different response to temperature of these links directly impacts the thermal expansion property of the bulk material, and in the case of TaO_2F may explain why zero thermal expansion is observed instead of NTE.

5.6 *Supplemental Information*

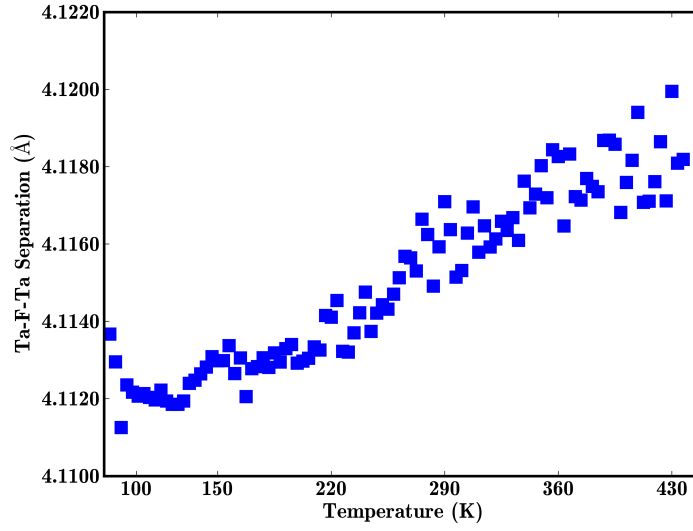


Figure 61: The Ta–F–Ta separation in TaO₂F as a function of temperature. The inter-atomic separation was determined from a Gaussian fit to the peak in the atomic PDF. The Q_{max} used was 25.0 Å^{−1}. The average linear coefficient of thermal expansion is 3.1 ppm·K^{−1}.

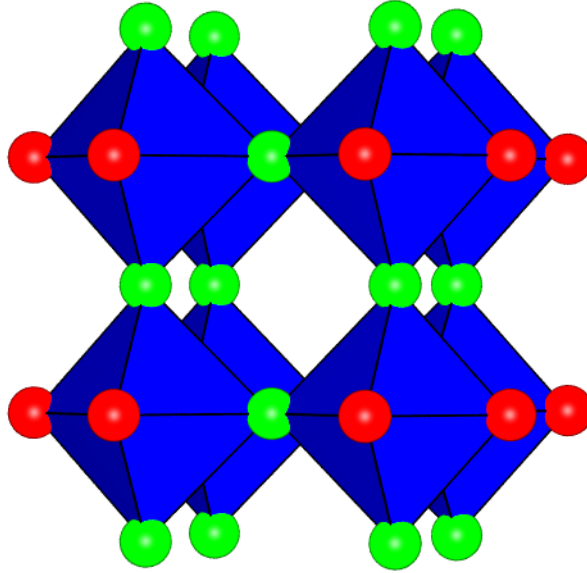


Figure 62: Crystal structure of the tetragonal model with oxygen atoms in the equatorial $a - b$ plane used to fit the low r portion of the PDF for cubic TiOF₂. The Ti atoms reside at the center of the octahedra, the red spheres are oxygen atoms, and the green spheres are fluorine atoms.

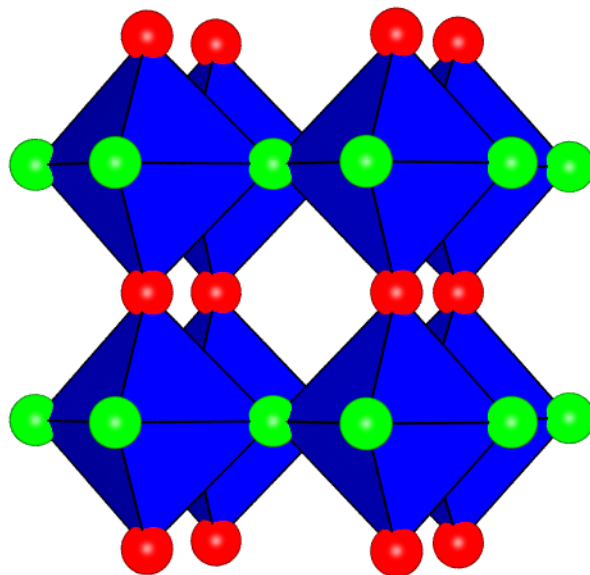


Figure 63: Crystal structure of the tetragonal model with oxygen atoms out of the equatorial $a - b$ plane used to fit the low r portion of the PDF for cubic TiOF_2 . The Ti atoms reside at the center of the octahedra, the red spheres are oxygen atoms, and the green spheres are fluorine atoms.

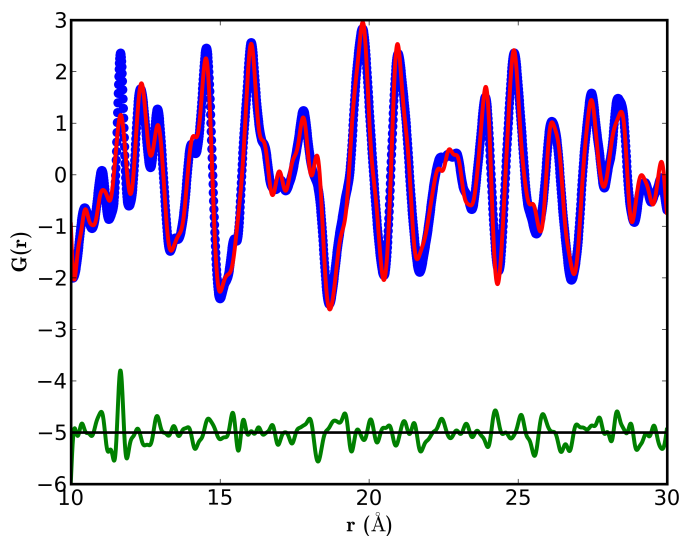


Figure 64: Representative fit of the cubic $Pm\bar{3}m$ model to the variable temperature PDFs for TaO_2F . The red (—) is the fit, the blue (o) are the data points, and the green (—) is the difference curve between the fit and the data.

Table 25: Extracted TaO₂F lattice constants from fits of the cubic $Pm\bar{3}m$ model to the variable temperature PDFs ($r = 10\text{--}30$ Å).

Temperature (K)	a Å	Temperature (K)	a Å
80	3.8842(7)	262.5	3.8845(8)
83.7	3.8841(7)	266.2	3.8846(8)
87.3	3.8841(7)	269.8	3.8847(8)
91	3.8841(7)	273.5	3.8847(8)
94.6	3.8842(7)	277.1	3.8848(8)
98.3	3.8842(7)	280.8	3.8849(8)
101.9	3.8842(7)	284.4	3.8849(8)
105.6	3.8842(7)	288.1	3.8849(8)
109.2	3.8842(7)	291.7	3.8849(8)
112.9	3.8842(7)	295.4	3.8849(8)
116.5	3.8842(7)	299	3.8848(8)
120.2	3.8843(7)	302.7	3.8847(8)
123.8	3.8844(7)	306.3	3.8847(8)
127.5	3.8845(7)	310	3.8846(8)
131.1	3.8845(7)	313.6	3.8846(8)
134.8	3.8845(7)	317.3	3.8846(8)
138.4	3.8846(7)	320.9	3.8846(8)
142.1	3.8846(7)	324.6	3.8846(8)
145.7	3.8846(8)	328.2	3.8846(8)
149.4	3.8846(8)	331.9	3.8846(8)
153	3.8844(8)	335.5	3.8846(8)
156.7	3.8844(8)	339.2	3.8846(8)
160.3	3.8843(8)	342.8	3.8847(8)
164	3.8843(8)	346.5	3.8847(8)
167.6	3.8843(8)	350.1	3.8847(8)
171.3	3.8843(8)	353.8	3.8847(8)
174.9	3.8843(8)	357.4	3.8847(8)
178.6	3.8843(8)	361.1	3.8847(8)
182.2	3.8843(8)	364.7	3.8847(8)
185.9	3.8843(8)	368.4	3.8848(8)
189.5	3.8843(8)	372	3.8848(8)
193.2	3.8844(8)	375.7	3.8848(8)
196.8	3.8843(8)	379.3	3.8848(8)
200.5	3.8843(8)	383	3.8848(8)
204.1	3.8844(8)	386.6	3.8849(8)
207.8	3.8844(8)	390.3	3.8849(8)
211.4	3.8844(8)	393.9	3.8849(8)
215.1	3.8844(8)	397.6	3.8850(8)
218.7	3.8844(8)	401.2	3.8850(8)
222.4	3.8844(8)	404.9	3.8851(9)
226	3.8844(8)	408.5	3.8851(9)
229.7	3.8844(8)	412.2	3.8851(9)
233.3	3.8844(8)	415.8	3.8852(9)
237	3.8844(8)	419.5	3.8852(9)
240.6	3.8844(8)	423.1	3.8854(9)
244.3	3.8844(8)	426.8	3.8855(9)
247.9	3.8844(8)	430.4	3.8856(9)
251.6	3.8845(8)	434.1	3.8857(9)
255.2	3.8845(8)	437.7	3.8858(9)
258.9	3.8845(8)	441.4	3.8858(9)

Table 26: Final 3x3x3 supercell used to fit the local structure of TaO₂F. There are no ESDs on the values as the model was optimized by hand.

<i>Atom</i>	<i>x</i>	<i>y</i>	<i>z</i>	<i>Atom</i>	<i>x</i>	<i>y</i>	<i>z</i>
Ta	0.0	0.0	0.0	O	0.33333	0.33333	0.83833
Ta	0.35184	0.0	0.0	O	0.33333	0.66667	0.51500
Ta	0.67592	0.0	0.0	O	0.33333	0.66667	0.83833
Ta	0.0	0.0	0.32408	O	0.66667	0.0	0.16167
Ta	0.32408	0.0	0.32408	O	0.66667	0.0	0.48500
Ta	0.64816	0.0	0.32408	O	0.66667	0.33333	0.16167
Ta	0.0	0.0	0.64816	O	0.66667	0.33333	0.83833
Ta	0.32408	0.0	0.64816	O	0.66667	0.66667	0.51500
Ta	0.67592	0.0	0.64816	O	0.66667	0.66667	0.83833
Ta	0.0	0.32408	0.0	O	0.0	0.16204	0.0
Ta	0.35184	0.32408	0.0	O	0.0	0.83796	0.0
Ta	0.67592	0.32408	0.0	O	0.0	0.51388	0.33333
Ta	0.0	0.35184	0.32408	O	0.0	0.83796	0.33333
Ta	0.32408	0.35184	0.32408	O	0.0	0.16204	0.66667
Ta	0.64816	0.35184	0.32408	O	0.0	0.48612	0.66667
Ta	0.0	0.32408	0.67592	O	0.33333	0.16204	0.0
Ta	0.32408	0.32408	0.67592	O	0.33333	0.83796	0.0
Ta	0.67592	0.32408	0.67592	O	0.33333	0.51388	0.33333
Ta	0.0	0.67592	0.0	O	0.33333	0.83796	0.33333
Ta	0.35184	0.67592	0.0	O	0.33333	0.16204	0.66667
Ta	0.67592	0.67592	0.0	O	0.33333	0.48612	0.66667
Ta	0.0	0.67592	0.35184	O	0.66667	0.16204	0.0
Ta	0.32408	0.67592	0.35184	O	0.66667	0.83796	0.0
Ta	0.64816	0.67592	0.35184	O	0.66667	0.51388	0.33333
Ta	0.0	0.64816	0.67592	O	0.66667	0.83796	0.33333
Ta	0.32408	0.64816	0.67592	O	0.66667	0.16204	0.66667
Ta	0.67592	0.64816	0.67592	O	0.66667	0.48612	0.66667
O	0.51388	0.0	0.0	F	0.17592	0.0	0.0
O	0.83796	0.0	0.0	F	0.82408	0.0	0.33333
O	0.16204	0.0	0.33333	F	0.5	0.0	0.66667
O	0.48612	0.0	0.33333	F	0.17592	0.33333	0.0
O	0.16204	0.0	0.66667	F	0.82408	0.33333	0.33333
O	0.83796	0.0	0.66667	F	0.5	0.33333	0.66667
O	0.51388	0.33333	0.0	F	0.17592	0.66667	0.0
O	0.83796	0.33333	0.0	F	0.82408	0.66667	0.33333
O	0.16204	0.33333	0.33333	F	0.5	0.66667	0.66667
O	0.48612	0.33333	0.33333	F	0.0	0.0	0.82333
O	0.16204	0.33333	0.66667	F	0.0	0.33333	0.5
O	0.83796	0.33333	0.66667	F	0.0	0.66667	0.17667
O	0.51388	0.66667	0.0	F	0.33333	0.0	0.82333
O	0.83796	0.66667	0.0	F	0.33333	0.33333	0.5
O	0.16204	0.66667	0.33333	F	0.33333	0.66667	0.17667
O	0.48612	0.66667	0.33333	F	0.66667	0.0	0.82333
O	0.16204	0.66667	0.66667	F	0.66667	0.33333	0.5
O	0.83796	0.66667	0.66667	F	0.66667	0.66667	0.17667
O	0.0	0.0	0.16167	F	0.0	0.5	0.0
O	0.0	0.0	0.48500	F	0.0	0.17592	0.33333
O	0.0	0.33333	0.16167	F	0.0	0.82408	0.66667
O	0.0	0.33333	0.83833	F	0.33333	0.5	0.0
O	0.0	0.66667	0.51500	F	0.33333	0.17592	0.33333
O	0.0	0.66667	0.83833	F	0.33333	0.82408	0.66667
O	0.33333	0.0	0.16167	F	0.66667	0.5	0.0
O	0.33333	0.0	0.48500	F	0.66667	0.17592	0.33333
O	0.33333	0.33333	0.16167	F	0.66667	0.82408	0.66667

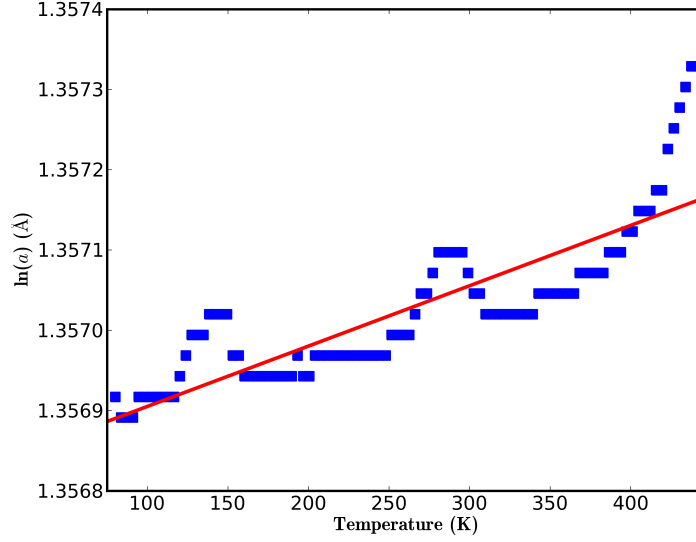


Figure 65: Log of the TaO_2F lattice constant (blue ■) versus temperature extracted from fits to the variable temperature PDFs. The red (–) is a straight line fit used to calculate the average linear coefficient of thermal expansion.

Table 27: The final atomic positions in the tetragonal cell which was refined with the oxygen atoms out of the $a - b$ plane until a minimum in R_W was observed, then the oxygen atoms were placed back into the $a - b$ plane and further refinement was performed. The refined lattice constants for this model were: $a=b=7.512(2)$ Å and $c=3.914(2)$ Å.

<i>Atom</i>	<i>x</i>	<i>y</i>	<i>z</i>
Ti	0.760(1)	0.760(1)	0.0
Ti	0.240(1)	0.240(1)	0.0
Ti	0.240(1)	0.760(1)	0.0
Ti	0.760(1)	0.240(1)	0.0
F	0.766(4)	0.766(4)	0.5
F	0.234(4)	0.234(4)	0.5
F	0.234(4)	0.766(4)	0.5
F	0.766(4)	0.234(4)	0.5
O	0.0	0.77(1)	0.0
O	0.0	0.23(1)	0.0
O	0.23(1)	0.0	0.0
O	0.77(1)	0.0	0.0
F	0.5	0.74(2)	0.0
F	0.5	0.26(2)	0.0
F	0.26(2)	0.5	0.0
F	0.74(2)	0.5	0.0

CHAPTER VI

CONCLUDING REMARKS

A clear understanding of a material’s thermal expansion is crucial when considering potential applications. Materials that have large coefficients of thermal expansion (CTE) often have poor thermal shock resistance and can develop cracks during periods of rapid heating and cooling. Likewise, materials with large CTEs can be problematic in applications that require dimensional stability such as precision optics. Considerable research effort has been directed towards finding materials that exhibit low, or even zero thermal expansion, as this should have enhanced thermal shock resistance and would be ideal in applications where dimensional stability is important. Negative thermal expansion (NTE) materials, those which contract on heating, have also been the target of recent research as they are of fundamental interest and may find use in controlled thermal expansion composites.

Negative thermal expansion in framework materials may arise through the transverse thermal motion of bridging moieties and the coupled rotation of rigid units. In elementary discussions explaining the mechanisms of thermal expansion, the cubic ReO_3 structure is often used as an illustrative example. Although ReO_3 only exhibits mild NTE at low temperature, most likely owing to Re’s single delocalized d -electron, there are a variety of other materials that adopt the ReO_3 structure-type and might have interesting expansion characteristics. In Chapter 2 of this thesis, the thermal expansion properties of ScF_3 , which adopts the cubic ReO_3 structure, were explored and pronounced negative thermal expansion was observed across a broad temperature range.

The thermal expansion properties of TiOF_2 were examined in Chapter 3, as some reports indicated that this material adopts the cubic ReO_3 structure type at room temperature. Positive thermal expansion was observed at all temperatures for TiOF_2 , and a rhombohedrally distorted variant of the ReO_3 structure type was observed at room temperature. The material produced from the digestion of TiO_2 in HF, which is the most commonly

used synthetic route in the literature, was not TiOF_2 but rather a Ti-vacancy containing hydroxyoxyfluoride ($\text{Ti}_{1-x}(\text{O}/\text{OH}/\text{F})_3$) that adopts a cubic ReO_3 structure. This material hydrolyzes upon heating, and the resulting material exhibits positive thermal expansion at all temperatures. There were no observed phase transitions on compression to ≈ 9 GPa for TiOF_2 , however a phase transition from cubic to rhombohedral symmetry was observed upon compression for $\text{Ti}_{1-x}(\text{O}/\text{OH}/\text{F})_3$ between 0.5-1 GPa.

In Chapter 4, the effect of pressure on the CTEs of ScF_3 and TaO_2F was examined using *in situ* variable pressure-temperature neutron diffraction. One possible application for NTE and zero expansion materials is in composites with tailored CTEs; during the manufacture and use of these composites stresses may be experienced, which can alter the behavior of materials. Pressure had a negligible effect on the thermal expansion of cubic ScF_3 , however a phase transition was observed from cubic to rhombohedral symmetry when cooled to 100 K and compressed to greater than 0.2 GPa. For TaO_2F , the application of modest pressure, such as those that would be experienced during the manufacture of a composite, had a dramatic effect on its coefficient of thermal expansion, resulting in it becoming more positive. As the CTE of TaO_2F is extremely sensitive to modest pressure, its use in situations where it may experience stress is precluded.

Finally, in Chapter 5, the local structures of TiOF_2 and TaO_2F were examined using pair distribution functions that had been calculated from X-ray total scattering experiments. While the average structures of these materials are very simple, the local structure is more complex because of the different $M-X$ ($M = \text{Ti}, \text{Ta}; X = \text{O}, \text{F}$) bonds. Simple structural models were used to examine the low r portion of the PDFs, and they indicated that there were very different $M-X-M$ linkages present in both of these materials. A simple analysis of the variable temperature PDFs for TaO_2F using Gaussian fits to peaks in the PDFs suggests that these distinct links respond differently to temperature. Their different responses to temperature may explain why TaO_2F exhibits near zero thermal expansion rather than NTE.

REFERENCES

- [1] M. A. White. *Properties of Materials*. Oxford University Press, New York, New York, 1999.
- [2] *Handbook of Materials Selection*. J. Wiley, New York, 2002.
- [3] M. B. Jakubinek, C. A. Whitman, and M. A. White. Negative thermal expansion materials, thermal properties and implications for composite materials. *Journal of Thermal Analysis and Calorimetry*, 99:165–172, 2010.
- [4] J. S. O. Evans. Negative thermal expansion materials. *Journal of the Chemical Society, Dalton Transactions*, pages 3317–3326, 1999.
- [5] *Atkins Physical Chemistry*. W.H. Freeman and Company, New York, NY, eighth edition, 2006.
- [6] W. Miller, C. W. Smith, D. S. Mackenzie, and K. E. Evans. Negative thermal expansion: a review. *Journal of Material Science*, 44:5441–5451, 2009.
- [7] R. Roy, D. K. Agrawal, and H. A. McKinstry. Very low thermal expansion coefficient materials. *Annual Reviews in Materials Science*, 19:59–81, 1989.
- [8] A. W. Sleight. Isotropic negative thermal expansion. *Annual Reviews in Materials Science*, 28:29–43, 1998.
- [9] F. A. Hummel. Thermal expansion properties of natural lithia materials. *Footprints*, 20:3, 1948.
- [10] F. A. Hummel. Thermal expansion properties of some synthetic lithia mineral. *Journal of the American Ceramics Society*, 34:235, 1951.
- [11] J. P. Boilot, J. P. Salanie, and G. Desplanches. Phase transformation in $\text{Na}_{1+x}\text{Si}_x\text{Zr}_2\text{P}_{3-x}\text{O}_{12}$ compounds. *Materials Research Bulletin*, 14:1469, 1979.
- [12] A. W. Sleight. Compounds that contract on heating. *Inorganic Chemistry*, 37:2854–2860, 1998.
- [13] D. B. Balashov and V. P. Orlov. Thermal anomaly of water. I. Regional boundaries. entropy. heat capacities. *Zhurnal Fizicheskoi Khimii*, page 2465, 1983.
- [14] T. A. Mary, J. S. O. Evans, T. Vogt, and A. W. Sleight. Negative thermal expansion from 0.3 to 1050 kelvin in ZrW_2O_8 . *Science*, 272:90–92, 1996.
- [15] A. W. Sleight. Negative thermal expansion materials. *Current Opinion in Solid State and Materials Science*, 3:128–131, 1998.
- [16] J. Z. Tao and A. W. Sleight. The role of rigid unit modes in negative thermal expansion. *Journal of Solid State Chemistry*, 173:442–448, 2003.

- [17] A. K. A. Pryde, K. D. Hammonds, M. T. Dove, V. Heine, J. D. Gale, and M. C. Warren. Rigid unit modes and the negative thermal expansion in ZrW_2O_8 . *Phase Transitions A Multinational Journal*, 61:141–153, 1997.
- [18] J. S. O. Evans, T. A. Mary, and A. W. Sleight. Negative thermal expansion materials. *Physica B: Condensed Matter*, 241:311–316, 1997.
- [19] N. Matsuno, M. Yoshimi, S. Ohtake, T. Akahane, and N. Tsuda. Thermal expansion of ReO_3 . *Journal of the Physical Society of Japan*, 45:1542–1544, 1978.
- [20] D. Taylor. Thermal expansion v. miscellaneous binary oxides. *Transactions and Journal of the British Ceramic Society*, pages 9–14, 1985.
- [21] M. Dapiaggi and A. N. Fitch. Negative (and very low) thermal expansion in ReO_3 from 5 to 300 K. *Journal of Applied Crystallography*, 42(2):253–258, Apr 2009.
- [22] T. Chatterji, P. F. Henry, R. Mitall, and S. L. Chaplot. Negative thermal expansion of ReO_3 : Neutron diffraction experiments and dynamical lattice calculations. *Physical Review B: Condensed Matter and Materials Physics*, 78:134105, 2008.
- [23] U. D. Wdowik, K. Parlinski, T. Chatterji, S. Rols, and H. Schober. Lattice dynamics of rhenium trioxide from the quasiharmonic approximation. *Physical Review B*, 82(10):104301, Sep 2010.
- [24] E. E. Rodriguez, A. Llobet, Th. Proffen, B. C. Melot, R. Seshadri, P. B. Littlewood, and A. K. Cheetham. The role of static disorder in negative thermal expansion in ReO_3 . *Journal of Applied Physics*, 105(11):114901, 2009.
- [25] M. A. Hepworth, K. H. Jack, R. D. Peacock, and G. J. Westland. The crystal structures of the trifluorides of iron, cobalt, ruthenium, rhodium, palladium, and iridium. *Acta Crystallographica*, 10:63–69, 1957.
- [26] P. Daniel, A. Bulou, M. Rousseau, J. Nouet, and M. Leblanc. Raman-scattering study of crystallized $m\text{F}_3$ compounds ($M = \text{Al, Cr, Ga, V, Fe, In}$): An approach to the short-range-order force constants. *Physical Review B: Condensed Matter*, 42:10545–10552, 1990.
- [27] K. S. Vorres and J. Donohue. The structure of titanium oxydifluoride. *Acta Crystallographica*, 8:25–26, 1955.
- [28] S. Chaudhuri, P. J. Chupas, M. Wilson, P. Madden, and C. P. Grey. Study of the nature and mechanism of the rhombohedral-to-cubic phase transition in $\alpha\text{-AlF}_3$ with molecular dynamics simulations. *Journal of Physical Chemistry B*, 108:3437–3445, 2004.
- [29] B. J. Kennedy and T. Vogt. Powder x-ray diffraction study of the rhombohedral to cubic phase transition in TiF_3 . *Materials Research Bulletin*, 37:77–83, 2002.
- [30] A. Mogus-milankovic, J. Ravez, J. P. Chaminade, and P. Hagenmuller. Ferroelastic properties of some TF_3 compounds ($T = \text{Ti, V, Cr, Fe, Ga}$). *Materials Research Bulletin*, 20:9–17, 1985.

- [31] J. Ravez, A. Mogus-milankovic, J. P. Chaminade, and P. Hagenmuller. Ferroelastic properties of AlF_3 . *Materials Research Bulletin*, 19:1311–1316, 1984.
- [32] P. J. Chupas, S. Chaudhuri, Hanson J. C., X. Qiu, P. L. Lee, S. D. Shastri, S. J. L. Billinge, and C. P. Grey. Probing local and long-range structure simultaneously: An in situ study of the high-temperature phase transition of $\alpha\text{-AlF}_3$. *Journal of the American Chemical Society*, 126:4756–4757, 2004.
- [33] B. K. Greve, K. L. Martin, P. L. Lee, P. J. Chupas, K. W. Chapman, and A. P. Wilkinson. Pronounced negative thermal expansion from a simple structure: Cubic ScF_3 . *Journal of the American Chemical Society*, 132:15496–15498, 2010.
- [34] L. K. Frevel and H. W. Rinn. The crystal structure of NbO_2F and TaO_2F . *Acta Crystallographica*, 9, 1956.
- [35] J. Z. Tao and A. W. Sleight. Very low thermal expansion in TaO_2F . *Journal of Solid State Chemistry*, 173(1):45 – 48, 2003.
- [36] C. Lind, D. G. VanDerveer, A. P. Wilkinson, J. Chen, M. T. Vaughan, and D. J. Weidner. New high-pressure form of the negative thermal expansion materials zirconium molybdate and hafnium molybdate. *Chemistry of Materials*, 13:487–490, 2001.
- [37] T. Varga, A. P. Wilkinson, C. Lind, W. A. Bassett, and C. S. Zha. *In situ* high-pressure synchrotron x-ray diffraction study of $\text{Sc}_2\text{W}_3\text{O}_{12}$ at up to 10 GPa. *Physical Review B: Condensed Matter and Materials Physics*, 71:214106, 2005.
- [38] H. Holzer and D. C. Dunand. Phase transformation and thermal expansion of $\text{Cu/ZrW}_2\text{O}_8$ metal matrix composites. *Journal of Materials Research*, 14(3):780–789, 1999.
- [39] K. W. Chapman, P. J. Chupas, G. J. Halder, J. A. Hriljac, C. Kurtz, B. K. Greve, C. J. Ruschman, and A. P. Wilkinson. Optimizing high-pressure pair distribution function measurements in diamond anvil cells. *Journal of Applied Crystallography*, 43:297–307, 2010.
- [40] J. D. Jorgensen, S. Pei, P. Lighfoot, D. G. Hinks, B. W. Veal, B. Dabrowski, A. P. Paulikas, R. Kleb, and I. D. Brown. Pressure-induced charge transfer and dT_c/dP in $\text{YBa}_2\text{Cu}_3\text{O}_{7-x}$. *Physica C*, 171:93, 1990.
- [41] R. C. Wetherfold and J. Wang. Tailoring thermal deformation by using layered beams. *Composites Science and Technology*, 53:1, 1995.
- [42] Y. Fei. Effects of temperature and composition on the bulk modulus of $(\text{Mg,Fe})\text{O}$. *American Mineralogist*, 84:272–276, 1999.
- [43] J. S. O. Evans, Z. Hu, J. D. Jorgensen, D. N. Argyriou, S. Short, and A. W. Sleight. Compressibility, phase transitions, and oxygen migration in zirconium tungstate, ZrW_2O_8 . *Science*, 275:61, 1997.
- [44] Z. Hu, J. D. Jorgensen, S. Teslic, S. Short, D. N. Argyriou, J. S. O. Evans, and A. W. Sleight. Pressure-induced phase transformation in ZrW_2O_8 – compressibility and thermal expansion of the orthorhombic phase. *Physica B*, 340:241–243, 1998.

- [45] M. Cetinkol, A. P. Wilkinson, C. Lind, W. A. Bassett, and C. Zha. High-pressure powder diffraction study of TaO_2F . *Journal of Physics and Chemistry of Solids*, 68:611–616, 2007.
- [46] S. K. Sikka. Negative thermal expansion and its relation to high pressure. *Journal of Physics: Condensed Matter*, 16:S1033–S1039, 2004.
- [47] E. G. Ippolitov and A. G. Maklachkov. The condensed phase diagram of the $\text{BaF}_2\text{-YF}_3$ system. *Russian Journal of Inorganic Chemistry*, 15:753–755, 1970.
- [48] K. S. Aleksandrov, V. N. Voronov, A. N. Vtyurin, A. S. Krylov, M. S. Molokeev, M. S. Pavlovskii, S. V. Goryainov, A. Y. Likhacheva, and A. I. Ancharov. Pressure-induced phase transition in the cubic ScF_3 crystal. *Physics of the Solid State*, 51:810–816, 2009.
- [49] P. Melnikov and L. N. Komissarova. New form of scandium fluoride. *Journal of Physics and Chemistry of Solids*, 67:1899–1900, 2006.
- [50] A. P. Hammersley, S. O. Svensson, M. Hanfland, A. N. Fitch, and D. Hausermann. Two-dimensional detector software: From real detector to idealised image or two-theta scan. *High Pressure Research*, 14:235–248, 1996.
- [51] Peter J. Chupas, Karena W. Chapman, Charles Kurtz, Jonathan C. Hanson, Peter L. Lee, and Clare P. Grey. A versatile sample-environment cell for non-ambient X-ray scattering experiments. *Journal of Applied Crystallography*, 41(4):822–824, 2008.
- [52] J. D. Barnett, S. Block, and G. J. Piermarini. An optical fluorescence system for quantitative pressure measurement in the diamond-anvil cell. *Review of Scientific Instruments*, 44:1, 1973.
- [53] A. C. Larson and R. B. Von Dreele. General structure analysis system (GSAS). *Los Alamos National Laboratory Report LAUR 86-748*, 2000.
- [54] B. H. Toby. EXPGUI, a graphical user interface for GSAS. *Journal of Applied Crystallography*, 34:210–213, 2001.
- [55] J. Rodriguez-Carvajal. Recent advances in magnetic structure determination by neutron powder diffraction. *Physica B.*, 192:55, 1993.
- [56] K. W. Chapman, P. J. Chupas, and C. J. Kepert. Direct observation of a transverse vibrational mechanism for negative thermal expansion in $\text{Zn}(\text{CN})_2$: An atomic pair distribution function analysis. *Journal of the American Chemical Society*, 127:15630–15636, 2005.
- [57] A. L. Goodwin and C. J. Kepert. Negative thermal expansion and low-frequency modes in cyanide-bridged framework materials. *Physical Review B: Condensed Matter and Materials Physics*, 71:140301–4, 2005.
- [58] X. G. Zheng, H. Kubozono, H. Yamada, K. Kato, Y. Ishiwata, and C. N. Xu. Giant negative thermal expansion in magnetic nanocrystals. *Nature Nanotechnology*, 3:724–726, 2008.
- [59] K. Takenaka and H. Takagi. *Applied Physics Letters*, 87:261902–3, 2005.

- [60] J. Arvanitidis, K. Papagelis, S. Margadonna, K. Prassides, and A. N. Fitch. Temperature-induced valence transition and associated lattice collapse in samarium fulleride. *Nature*, 425:599–602, 2003.
- [61] A. M. Glazer. The classification of tilted octahedra in perovskites. *Acta Crystallographica*, B28:3384–3392, 1972.
- [62] K. S. Vorres and F. B. Dutton. The fluorides of titanium: X-ray powder data and some other observations. *Journal of the American Chemical Society*, 77:2019, 1955.
- [63] X. Rocquefelte, F. Goubin, Y. Montardi, N. Viadere, A. Demourgues, A. Tressaud, M.-H. Whangbo, and S. Jobic. Analysis of the refractive indices of TiO_2 , TiOF_2 , and TiF_4 : Concept of optical channel as a guide to understand and design optical materials. *Inorganic Chemistry*, 44(10):3589–3593, 2005. PMID: 15877442.
- [64] M.V. Reddy, S. Madhavi, G.V. Subba Rao, and B.V.R. Chowdari. Metal oxyfluorides TiOF_2 and NbO_2F as anodes for Li-ion batteries. *Journal of Power Sources*, 162(2):1312 – 1321, 2006. Special issue including selected papers from the International Power Sources Symposium 2005 together with regular papers.
- [65] J. Zhu, D. Zhang, Z. Bian, G. Li, Y. Huo, Y. Lu, and H. Li. Aerosol-spraying synthesis of $\text{SiO}_2/\text{TiO}_2$ nanocomposites and conversion to porous TiO_2 and single-crystalline TiOF_2 . *Chemical Communications*, pages 5394–5396, 2009.
- [66] K. Dehnicke. Über titandifluoriddichlorid und titanoxidfluorid. *Die Naturwissenschaften*, 24:660, 1965.
- [67] J. H. Moss and A. Wright. Titanium (IV) oxydifluoride. *Journal of Fluorine Chemistry*, 5:163 –167, 1975.
- [68] E. I. Mel’nichenko, G. F. Krysenko, D. G. Epov, and E. G. Rakov. Titanium oxyfluorides. *Russian Journal of Inorganic Chemistry*, 46(12):1769–1774, 2001.
- [69] S. Shian and K. H. Sandhage. Hexagonal and cubic TiOF_2 . *Journal of Applied Crystallography*, 43(4):757–761, Aug 2010.
- [70] A. Demourgues, N. Penin, E. Durand, F. Weill, D. Dambournet, N. Viadere, and A. Tressaud. New titanium hydroxyfluoride $\text{Ti}_{0.75}(\text{OH})_{1.5}\text{F}_{1.5}$ as a UV absorber. *Chemistry of Materials*, 21:1275–1283, 2009.
- [71] H. Serier, M. Gaudon, A. Demourgues, and A. Tressaud. Structural features of zinc hydroxyfluoride. *Journal of Solid State Chemistry*, 2007:3485–3492, 2007.
- [72] B. J. Kennedy and T. Vogt. Powder x-ray diffraction study of the rhombohedral to cubic phase transition in TiF_3 . *Materials Research Bulletin*, 37:77–83, 2002.
- [73] C. J. Howard, K. S. Knight, B. J. Kennedy, and E. H. Kisi. The structural phase transitions in strontium zirconate revisited. *Journal of Physics: Condensed Matter*, 12(45):L677–L683, 2000.
- [74] C. J. Howard, B. J. Kennedy, and B. C. Chakoumakos. Neutron powder diffraction study of rhombohedral rare-earth aluminates and the rhombohedral to cubic phase transition. *Journal of Physics: Condensed Matter*, 12(4):349, 2000.

- [75] S. Carlson, A. K. Larsson, and F. E. Rohrer. High-pressure transformations of NbO_2F . *Acta Crystallographica B*, 56:189–196, 2000.
- [76] K. W. Chapman and P. J. Chupas. Pressure enhancement of negative thermal expansion behavior and induced framework softening in zinc cyanide. *Journal of the American Chemical Society*, 129:10090–10091, 2007.
- [77] M. Cetinkol and A. P. Wilkinson. Pressure dependence of negative thermal expansion in $\text{Zr}_2(\text{WO}_4)(\text{PO}_4)_2$. *Solid State Communications*, 149:421–424, 2009.
- [78] J. D. Jorgensen, J. Faber Jr., J. M. Carpenter, R. K. Crawford, R. L. Haumann, R. L. Hitterman, R. Kleb, G. E. Ostrowski, F. J. Rotella, and T. G. Worlton. Electronically focused time-of-flight powder diffractometers at the intense pulsed neutron source. *Journal of Applied Crystallography*, 22:321, 1989.
- [79] A. P. Wilkinson, C. R. Morelock, B. K. Greve, A. C. Jupe, K. W. Chapman, P. J. Chupas, and C. Kurtz. Reducing the background from pressure vessels using a BRIM. *Journal of Applied Crystallography*, 44:1047–1053, 2011.
- [80] *Shriver & Atkins Inorganic Chemistry*. W. H. Freeman and Company, New York, New York, fourth edition, 2006.
- [81] F. J. Brink, R. L. Withers, and L. Noren. An electron diffraction and crystal chemical investigation of oxygen/fluorine ordering in niobium oxyfluoride, NbO_2F . *Journal of Solid State Chemistry*, 166:73–80, 2002.
- [82] S. J. L. Billinge and M. G. Kanatzidis. Beyond crystallography: The study of disorder, nanocrystallinity and crystallographically challenged materials with pair distribution functions. *Chemical Communications*, pages 749–760, 2004.
- [83] P. J. Chupas, X. Qiu, J. C. Hanson, P. L. Lee, C. P. Grey, and S. J. L. Billinge. Rapid-acquisition pair distribution function (RA-PDF) analysis. *Journal of Applied Crystallography*, 36:1342–1347, 2003.
- [84] X. Qiu, J. W. Thompson, and S. J. L. Billinge. PDFgetx2: A GUI driven program to obtain the pair distribution function from X-ray powder diffraction data. *Journal of Applied Crystallography*, 37:678, 2004.
- [85] C. L. Farrow, P. Juhas, J. W. Liu, D. Bryndin, E. S. Bozin, J. Bloch, Th. Proffen, and S. J. L. Billinge. PDFfit2 and PDFgui: Computer programs for studying nanostructure in crystals. *Journal of Physics: Condensed Matter*, 19:335219, 2007.
- [86] R. Mittal. Negative thermal expansion in framework compounds. *Pramana*, 71:829–835, 2008. 10.1007/s12043-008-0194-x.
- [87] J Purans, A Kuzmin, E Cazzanelli, and G Mariotto. Disorder-induced raman scattering in rhenium trioxide (ReO_3). *Journal of Physics: Condensed Matter*, 19(22):226206, 2007.
- [88] K. Aleksandrov, V. Voronov, A. Vtyurin, A. Krylov, M. Molokeev, M. Pavlovski, S. Goryanov, A. Likhacheva, and A. Ancharov. Pressure-induced phase transition in the cubic scf_3 crystal. *Physics of the Solid State*, 51:810–816, 2009. 10.1134/S1063783409040295.

- [89] T. Chatterji and G. J. McIntyre. Pressure-induced structural phase transition in reO_3 . *Solid State Communications*, 139(1):12 – 15, 2006.
- [90] Tapan Chatterji, P. G. Freeman, M. Jimenez-Ruiz, R. Mittal, and S. L. Chaplot. Pressure- and temperature-induced $m3$ phonon softening in reO_3 . *Phys. Rev. B*, 79(18):184302, May 2009.
- [91] D. Dambournet, A. Demourgues, C. Martineau, E. Durand, J. Majimel, C. Legein, J. Buzare, F. Fayon, A. Vimont, H. Leclerc, and A. Tressaud. Microwave synthesis of an aluminum fluoride hydrate with cationic vacancies: Structure, thermal stability, and acidic properties. *Chemistry of Materials*, 20(22):7095–7106, 2008.
- [92] C.E. Guillaume. *C. R. Acad. Sci.*, 125:235–238, 1897.
- [93] G. Scholz, S. Brehme, R. König, D. Heidemann, and E. Kemnitz. Crystalline aluminum hydroxide fluorides $\text{Al}_x(\text{OH})_{3-x}\cdot\text{H}_2\text{O}$: Structural insights from ^1H and ^2H solid state nmr and vibrational spectroscopy. *Journal of Physical Chemistry C*, 114:10535–10543, 2010.
- [94] H. Sowa and H. Ahsbah. Pressure-induced octahedron strain in VF_3 -type compounds. *Acta Cryst. B*, B54:578–584, 1998.
- [95] R. A. Howald, R. D. Jones, A. B. Rezvani, B. N. Roy, M. J. Scanlon, and T. M. Swager. Temperature dependence of the bulk modulus of solids in the magnesium oxide-aluminum oxide ($\text{AlO}_{1.5}$)silicon dioxide system. *Journal of Physical Chemistry*, 89(12):2682–2687, 1985.
- [96] *Local Structure from Diffraction*. Plenum Press, 1998.
- [97] D. B. Balashov and V. P. Orlov. I. Regional boundaries. entropy. heat capacities. *Zh. Fiz. Khim.*, 57:2465, 1983.